CO-ROBOTIC ULTRASOUND IMAGING: A COOPERATIVE FORCE CONTROL APPROACH

by
Rodolfo Gabriel Finocchi

An essay submitted to Johns Hopkins University in conformity with the requirements for the degree of Master of Science in Engineering

Baltimore, Maryland
May, 2016

ABSTRACT

Ultrasound (US) imaging remains one of the most commonly used imaging modalities in medical practice due to its low cost and safety. However, 63-91% of ultrasonographers develop musculoskeletal disorders due to the effort required to perform imaging tasks. Robotic ultrasound (RUS), the application of robotic systems to assist ultrasonographers in ultrasound scanning procedures, has been proposed in literature and recently deployed in clinical settings using limited degree-of-freedom systems. An example of this includes breast-scanning systems, which allow one-DOF translation of a large ultrasound array in order to capture patients' breast scans and minimize sonographer effort while preserving a desired clinical outcome. Recently, the robotic industry has evolved to provide light-weight, compact, accurate, and cost-effective manipulators. We leverage this new reality in able to provide ultrasonographers with a full 6-DOF system that provides force assistance to facilitate US image acquisition.

Admittance robot control allows for smooth human-machine interaction in a desired task. In the case of RUS, force control is capable of assisting sonographers in facilitating and even improving the imaging results of typical procedures. We propose a new system setup for collaborative force control in US applications. This setup consists of the 6-DOF UR5 industrial robot, and a 6-axes force sensor attached to the robot tooltip, which in turn has an US probe attached to it through a custom-designed probe attachment mechanism. Additionally, an independent one-axis load cell is placed inside this attachment device and used to measure the contact force between the probe and the patient's anatomy in real time and independent of any other forces. As the sonographer guides the US probe, the robot collaborates with the hand motions, following the path of

the user. When imaging, the robot can offer assistance to the sonographer by augmenting the forces applied by him or her, thereby lessening the physical effort required as well as the resulting strain. Additional benefits include force and velocity limiting for patient safety and robot motion constraints for particular imaging tasks. Initial results of a conducted user study show the feasibility of implementing the presented robot-assisted system in a clinical setting.

Advisor: Dr. Emad M. Boctor Reader: Russell H. Taylor

ACKNOWLEDGEMENTS

I would like to thank everyone who has helped and guided me throughout my time at the Johns Hopkins University. First, I would like to thank all of the professors with whom I have had the pleasure of interacting throughout my time at JHU, particularly those in the Biomedical Engineering Department and Laboratory for Computational Science and Robotics. Their desire and efforts to move their fields forward are inspirational as a student, researcher, engineer, and individual. In particular, I am grateful for the guidance provided by Dr. Emad Boctor throughout my graduate education and research. Additionally, I would like to thank Dr. Russell Taylor for sharing his broad wisdom and expertise in his field.

In addition, I would like to thank the members of the MUSiiC research lab, led by Dr. Boctor, for all the support and guidance provided throughout the year. In particular, I would like to thank Fereshteh Aalamifar for recruiting me to begin work on the project and for her mentorship since. Thank you also to Kai Zhang for his guidance involving Synthetic Tracked Aperture Ultrasound, Kalyna Apkarian for her tremendous partnership, Alexis Cheng for his advice, and Lei Chen for all his help involving ultrasound image acquisition.

I would also like to thank Dr. Iulian Iordachita and Dr. Reza Seifabadi for aiding me in the mechanical design of the custom-made probe holder and Dr. Tutkun Sen for all his help involving control of the UR5 robot.

Lastly, I would like to thank the people in my life who are there for me in ways no one else can be. To Paul Thaler, thank you for your boundless patience, love, and encouragement. To my friends, thank you for the support and sympathetic ears. Finally, to my parents, thank you for believing in me, for offering your wisdom in difficult times, and for always pushing me to be and do the best I can.

CONTENTS

LIST OF TABLES

LIST OF FIGURES

CHAPTER 1: INTRODUCTION

Ultrasound (US) imaging, or ultrasonography, is one of the most commonly used imaging modalities used to scan soft tissues of the body because it is inexpensive, non-ionizing, and generally real-time [1, 2]. Ultrasonography requires an ultrasonographer to hold an US probe on the surface of a patient, often requiring he or she push against the patient's tissue to reach imaging regions of interest found in deeper parts of their anatomy. Particularly when treating obese patients, sonographers must apply high forces to complete the procedure efficiently, often resulting in serious injury to the sonographer [3]. The following work focuses on ultrasound procedures such as these, in which sonographers are required to apply high forces for long durations.

Recent innovations in robotics have allowed the industry to provide lightweight, compact, accurate, and cost-effective arms that have the potential to revolutionize the way ultrasound procedures are performed. This thesis presents the architecture and design for a robotic ultrasound system that works collaboratively with sonographers to facilitate typically strenuous imaging tasks. The ultimate goal of the work presented is to reduce the harm to ultrasound sonographers while allowing them to collect high-quality image data. The system used to do this integrates robotics and sensors, providing a number of assisting behaviors such as effort augmentation, automatic force control and locking, and increased accuracy in certain imaging tasks. The performance of these capabilities is demonstrated by phantom experiments.

1.1 Thesis Statement

A force assistive framework with real-time sensing and cooperative human-machine control provides the capabilities to address fundamental limitations in ultrasound

An integrated system that consists of sensors and mechanical actuators can augment sonographer ability and reduce human effort and strain. Such a system can provide relevant assistance in imaging tasks that are difficult, time-consuming, and that lead to physical damage and pain. It can also help increase precision and control in probe movements and thereby improve image quality. Finally, such a system is not only clinically relevant, but also supports further research in the field.

1.2 Introduction to Computer-Integrated Surgery and Robotic Ultrasound

Computer-Integrated Surgery (CIS) has gained significant attention in the medical fields for its ability to increase the stability and robustness of medical procedures [4]. While some aspects of CIS focus on computer-assisted surgery (CAS), which continue to rely on the surgeon's abilities to perform a given surgical task, robotic surgery systems, have been shown to provide greater performance in certain procedures, as illustrated by Nathoo *et al.* [5]. For example, robotic-directed procedures have greater accuracy, precision and sustained identical repetitive motions than CAS. Additionally, robots do not fatigue in the same way that human surgeons do, allowing for faster procedures, reduced occurrence of tool tremor, and shorter reaction times. For these reasons, robotic systems have gained particular attention due to their ability to couple complex information to physical action in order to perform a useful task [6]. Robots consist of a mechanical device capable of interacting with its environment, sensors that receive information from the system's surrounding environment and its own internal state, and a processing unit (known as a

controller) that integrates these components and translates any input into corresponding mechanical actions. Robots and human surgeons are able to complement one another's strengths and weaknesses in a number of ways, as shown in Table 1.1.

	Strengths	Limitations
Humans	Excellent judgment Excellent hand–eye coordination Excellent dexterity (at natural *human* scale) Able to integrate and act on multiple information sources Easily trained Versatile and able to improvise	Prone to fatigue and inattention Limited fine motion control due to tremor Limited manipulation ability and dexterity outside natural scale Cannot see through tissue Bulky end-effectors (hands) Limited geometric accuracy Hard to keep sterile Affected by radiation, infection
Robots	Excellent geometric accuracy Untiring and stable Immune to ionizing radiation Can be designed to operate at many different scales of motion and payload Able to integrate multiple sources of numerical and sensor data	Poor judgment Hard to adapt to new situations Limited dexterity Limited hand–eye coordination Limited haptic sensing (today) Limited ability to integrate and interpret complex information

Table 1.1 Complementary strengths of human surgeons and robots [6]. Reprinted with permission from Springer. Copyright 2008.

A large field of research has aimed at exploiting the benefits of such human-machine relationships to improve or simplify common medical procedures and discover new possibilities in medical treatment. Robots have been used clinically in a variety of applications including, but not limited to, orthopedics, radiation therapy, and urology, in order to perform common tasks with greater accuracy, consistency, or ease by augmenting the ability of a typical clinician [4-7]. In particular, admittance force control, which translates forces applied to the end of the robot and measured by a sensor to robot velocities, has been used in a number of procedures, including skull base surgery [8], and retinal microsurgery [9-11]. Using this method, cooperative control of the robot can be introduced. With admittance control, the direction of the motion of the robot is the same as that of the force applied, and its speed is proportional to the force's magnitude. In these

situations, the human is always in contact with the robot, which can increase the chance of clinician acceptance and adoption of a robotic system, especially for procedures in which the clinician is accustomed to having full control of their tool or where direct interaction with the patient is necessary [4].

1.3 Ultrasound and Work-Related Musculoskeletal Disorders

One such group of procedures is that of ultrasound imaging. US consists of sending pulses of ultrasound waves into tissue using a probe and detecting their reflections in order to determine the internal structure of the tissue and to construct an image. US is used extensively in medical diagnoses with common applications including fetal imaging, tumor detection, biopsy needle insertion, tracking and monitoring, and musculoskeletal imaging. Additionally, ultrasonography has been used in surgery for decades as it can be a critical tool in the identification of surgical targets, or the avoidance of sensitive anatomical structures [1]. However, the acquisition of optimal images is highly dependent on sonographer skill. In the past two decades, researchers have aimed at applying some of the benefits of medical robots to ultrasound procedures where hand-tremor, varying application forces and sonographer injury are relevant factors. In fact, because of the application force necessary to acquire high-quality ultrasound images, the number of procedures a clinician might perform in any one day, and the duration of such procedures, work-related musculoskeletal disorders (WRMSDs) are estimated to affect 63% to 91% of sonographers, compared to 13% to 22% for the general population. These disorders, which include tendonitis, carpal tunnel syndrome and shoulder rotator cuff injuries, cause over

90% of sonographers to scan patients while in pain, leading many to end their careers prematurely [3,12-16].

Proper ultrasound imaging technique requires both static and dynamic loading of an ultrasonographer's musculature in order to place the probe at an appropriate angle for the acquisition of viable images. As Schoenfeld [12] reported, these positions are often awkward and must be held for long durations. During examinations, a clinician's arm is permanently contracted without a rest period for an average procedural duration of more than 25 minutes [3]. As shown by Village *et al.* [13], during 90% of this time, the applied force is at a minimum of 1kg (~9.8N), providing few opportunities for rest and recovery. Additionally, they also found that forceful gripping of the ultrasound probe is positively correlated with the onset of WRMSD symptoms. Sonographers apply an average of 3.96 kg (≈38.81 N) of force in gripping the transducer over an entire scanning period and in the

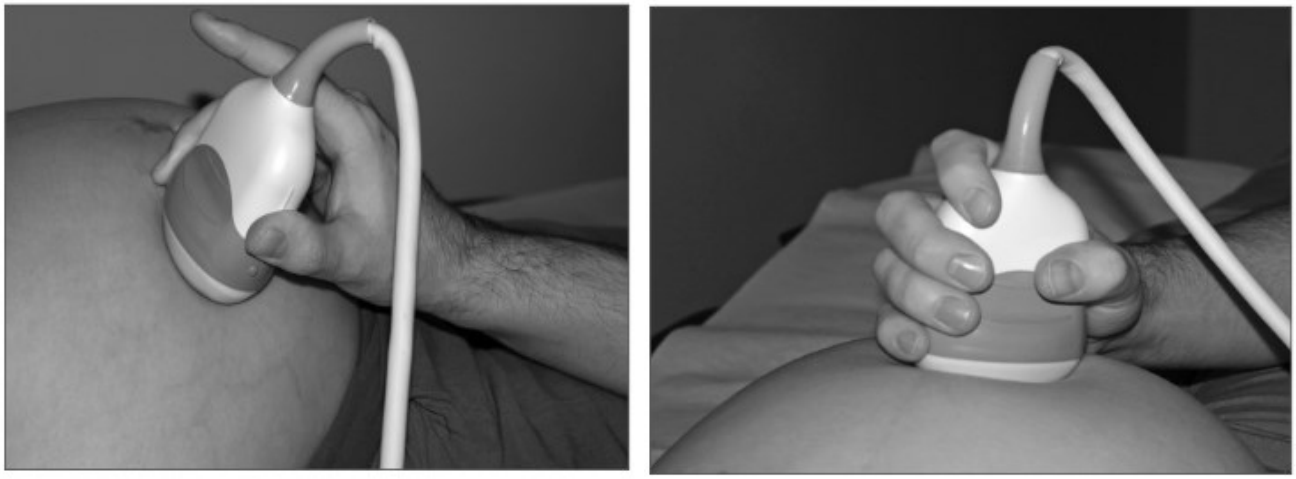

Figure 1.1 The two types of grips employed by ultrasonographers on ultrasound probes. Left: Pinch grip; not recommended. Right: Palmar, or power grip; deploys greater force and can lessen muscle tiredness [3]. Reprinted with permission from The Associati

case of obese patients, this force has been shown to reach up to 27.6 kg (≈270.48 N). At these high forces, the risk of harm in the sonographer is high. Pinch grips – grips between a person's fingers and their thumb – that exceed 0.9 kg (8.82 N) or palmar power grips –

grips that involve the whole hand wrapped around the ultrasound probe handle – exceeding 4.5 kg (~44.1 N), lead to an increase in the risk of joint injuries. This is further exacerbated by the prolonged periods for which sonographers hold these positions [14, 15]. Both types of grips are depicted in Figure 1.1.

		Side Within Location, %			Severity Within Location, %		
	% of *n* With Pain	Left Side	Right Side	Both Sides	Slight	Moderate	Severe
Neck	65.8	17.0	41.1	41.6	28.2	57.7	14.1
Upper back	44.3	13.1	39.1	47.9	27.3	61.7	11.1
Middle back	17.9	10.1	31.0	58.9	30.0	59.7	10.3
Lower back	33.2	13.7	23.6	62.7	25.2	57.3	17.5
Shoulder	74.6	19.6	58.4	22.1	23.2	55.9	20.9
Shoulder blade	37.7	18.2	64.5	17.3	23.9	57.3	18.8
Upper arm	27.0	18.4	69.4	12.1	34.1	53.8	12.1
Elbow/forearm	32.1	18.9	65.0	16.2	30.4	53.7	15.9
Wrist	49.7	17.1	60.4	22.5	34.5	51.2	14.3
Hand/fingers	44.2	17.7	57.1	25.2	32.7	50.1	17.2

Table 1.2: Location and Severity of Reported Pain/Discomfort Experienced While Scanning (n = 2679) [16]. Reprinted with permission from SAGE Publishing. Copyright 2009.

Evans *et al.* [16] surveyed 2,679 vascular technologists (VTs) and diagnostic medical sonographers (DMSs) about the extent of their WRMSD symptoms. Table 1.2 shows the results, presenting the prevalence of these conditions, the variety of anatomical locations where they lead to sonographer pain, and the severity of pain at each location. Across all demographics, shoulder and neck pain are the most common, with most clinicians reporting moderate to severe pain. DMS and VT jobs are expected to grow by 24% in 2014-2024, amounting to 27,600 new jobs in these fields by the end of this period [17]. Therefore, as more people enter this field, the more that will suffer from the effects of these debilitating conditions.

The work done by a number of groups in machine-assisted ultrasound imaging aims at reducing the burden on the sonographer by holding and moving the probe with the appropriate force needed for high quality imaging [18]. In particular, three robotic ultrasound (RUS) approaches have been used by different researchers to do so. These

approaches are autonomous RUS imaging, teleoperated RUS, and human-robot cooperative RUS.

1.4 Autonomous Robotic Ultrasound Systems

The first type of RUS system, autonomous imaging, does all of the physical work of the sonographer without any human interaction. It requires the presence of a technician to ensure patient safety and proper robot behavior. As with other US systems, it requires the skills of a sonographer to analyze resulting images and make relevant clinical decisions.

Boctor et al. [19] presented a comparison between manual and autonomous robot-assisted ultrasound-guided hepatic ablative therapy. Their system consisted of two robotic arms, one that held the ultrasound probe and another that positioned a needle guide. Anatomical volumes of interest were reconstructed into 3D ultrasound images, which improved needle insertion accuracy. The average reported mismatch between real and planned insertion depths was 1.2 mm across three trials and the average error in the needle positioning was ~3 mm across ten trials.

Ding et al. [20] developed a robotic system to assist in ultrasound guided needle placement. The robot provides the spatial movement needed and controls the contact force between the ultrasound probe and patient, while the clinician is freed up to insert a needle accurately. A 6 degree of freedom (DOF) parallel robot that automatically maintained skin contact and imaging angle of the ultrasound probe was presented. Results showed that their impedance control algorithm was able to stabilize the contact force in just under ten seconds. They also reported the robot's ability to autonomously react to patient breathing

in order to maintain the desired contact force; variability in the contact force applied during respiration was 0.2lb, a tolerance they deemed acceptable for the application.

Krupa [21] developed an automated RUS method to spatially calibrate the location of an ultrasound probe for accurate 3D imaging. A new visual servoing technique is presented. It uses 2D ultrasound images to control the robot motion and position the image on the intersection point of a cross-wire phantom used for spatial calibration. The calibration procedure provided high accuracy in 3D reconstruction and proved to be highly robust to large model errors.

Janvier et al. [22] conducted positioning and inter-target accurate analyses of a robotic serial arm designed for accurate 3D ultrasound imaging of lower limb vessels. They report a mean positioning accuracy between 0.46 mm and 0.75 mm and a mean inter-target distance accuracy between 0.26 mm and 0.62 mm. A teach/replay mode was meant to have the robot learn from a freehand scan and repeat it. For this functionality, a repeatability error of less than 0.20 mm was reported. It was concluded that the robot proved to be a suitable tracking device because of its high precision and accuracies.

Hong et al. [23] present a real-time ultrasound-guided needle-insertion medical robot for percutaneous cholecystostomy, a procedure for the drainage of the gallbladder. The proposed design used intraoperative images to modify the needle path in real time. They accomplished needle path updating times of 130 and 131 ms per cycle in phantom and volunteer experiments, respectively. Animal experiments showed the feasibility of clinical use.

1.5 Teleoperated Robotic Ultrasound Systems

The second robotic ultrasound approach, teleoperated imaging, allows a skilled sonographer to remotely assist with a procedure by controlling a robotically held ultrasound probe through a separate control panel or joystick.

Salcudean et al. [24] developed one such system for diagnostic ultrasound for carotid artery examinations, using visual servoing to enable motion in the plane of the ultrasound probe. In this case, the robot controlled three degrees of freedom (DOF), while the operator controlled the other degrees with a joystick/haptic interface.

Koizumi et al. [25] describe a master-slave type remote medical system used to diagnose shoulder diseases using ultrasound imaging. The system focuses on proper positioning, orientation, and contact force between the US probe and the area of interest. Impedance control is used for positioning of the master and slave manipulators to convey the contact force and enhance manipulability. An experiment was run in which a diagnostic specialist diagnosed a real patient using the remote system in real time. The contact force control proved to be sufficient in able to acquire and maintain proper diagnostic images efficiently. The average diagnostic time between remote and normal diagnoses across four patients was approximately 275 vs 225 seconds, respectively, values which were deemed approximately equivalent.

Vieyres et al. [26] present TERESA, a tele-echography project with the goal of bringing quality US examinations to astronauts and remotely located patients "on ground", despite the lack of a specialist at the location. The project makes use of 4 DOF mechanical system that holds an US probe and is able to rotate around the three axes and translate along the Z axis, allowing for continuous contact of the US probe with the patient’s skin. The

remote sonographer uses a fictive probe on a magnetic tracker to move the probe as desired, and the probe holding robot mimics movements. Results on 20 patients showed the feasibility of the device and the possibility to obtain good views from the remote site.

Vilchis-González et al. [27] describe the TERMI master-slave system used for remote ultrasound venous thrombosis examinations of the lower extremities. The system allows for the control of four degrees of freedom on the slave side. The results showed that from null initial conditions and a set desired position $q_d = [0.125\ 0.1875\ 0.0625]^T$, all errors converge to zero with smooth solutions.

Solazzi et al. [28] developed a 5-DOF RPaPaRR (R: revolute joint, Pa: parallel joint) robot for the accurate position of an ultrasound probe for the evaluation of endothelial function. It allowed the sonographer to manipulate the probe directly, or to move it using two joysticks. The positioning accuracy of the robot was reported as 0.062 mm, 0.089 mm, and 0.005º in the x, y, and roll angular directions, respectively. Qualitative clinical studies showed using the device made the positioning steadier and resulted in a sharper ultrasound image when compared with freehand.

Nakadate et al. [29] describe their automated medical ultrasound scanning system for the carotid artery using a 6-DOF parallel link mechanism. A phantom experiment is run to align the image of an inserted needle from an initial position to a target position using the joystick controller compared with freehand. The average error using freehand was reported as 0.27-0.29 mm and dropped to 0.06-0.07 mm with the help of the manipulator.

Mathiassen et al. [30] used the UR5 6-DOF robot for teleoperated procedures. They implemented admittance control to allow the sonographer to bring the probe close to the patient's body and then relied on a teleoperational module to apply force against the patient

and acquire ultrasound images. The system performance was evaluated based on compliance force control accuracy, real time performance, and forward flow haptic control performance between the slave and master systems.

Monfaredi et al. [18] developed a compact 6-DOF parallel teleoperated robot with three legs and two plates. The measured forces from a force sensor are directly fed back to the operator using a haptic device. A PID controller is used to close the position tracking control loop. A qualitative study with an experienced radiologist concluded that the system has the necessary dexterity required for scanning a region of interest. The error of tracking was <1mm, which was deemed appropriate for ultrasound applications.

1.6 Human-Robot Cooperative Robotic Ultrasound Systems

While autonomous robot control and teleoperation have their benefits, both methods require a significant change in the clinical workflow. The first allows the clinician to focus on aspects of their procedure that have little to do with the probe placement or force application. While it might be convenient, it can also be dangerous since it may cause the ultrasonographer to ignore the robot's actions altogether. In the case of an emergency, reaction times are likely to be slower than if the clinician had direct control over the mechanism. The second method, teleoperation, also has its benefits as it allows people in remote settings to gain access to the expertise of ultrasonographers, which they might not otherwise. However, it demands that clinicians learn how to manipulate the systems' specific teleoperation modules, making it difficult for standardization and clinical adoption. The final category of RUS is human-robot cooperation, in which the human

operator and robot share control of the US probe, thereby making it the method that most closely mimics standard freehand ultrasound techniques.

Aalamifar et al. [31] used a dual-probe approach for ultrasound tomography, in which a robotically controlled ultrasound probe tracked and followed the position of a second sonographer-held freehand probe. In this case, while the robot-held ultrasound probe was controlled directly by the manipulation of the sonographer-held probe, the robot itself did not come in contact with the operator. In [32] a second version of this system is described. This version uses two identical robots to hold each probe. As one is moved, the second tracks the probe and moves accordingly. The first robot is controlled with admittance control, reacting to the force commands of the user, while the second robot moves autonomously.

Şen et al. [33] present a cooperatively controlled robot for ultrasound monitoring of radiation therapy. The UR5 is used to reproducibly position an US probe on the patient during simulation and treatment for improvement of soft issue visualization and to allow real-time monitoring of the target. The system integrates 3D ultrasound imaging with computed tomography (CT) guidance for external beam radiotherapy. During CT imaging, a model probe is used to create deformations similar to that caused by a real US probe for simplified US-CT registration. Virtual springs are implemented to guide the ultrasound probe to a position recorded from a prior imaging session. However, though a soft virtual fixture, the clinician is able to deviate from this position by exerting forces against the springs, and thereby compensate for any placement error caused by inter-day patient movement. Experiments that demonstrate the effectiveness of these virtual springs and their repeatability are presented.

Nakadate et al. [34] designed a 3-DOF arm that can be used to guide the probe in space to a desired part of the patient's anatomy. They also designed an arm-supporting manipulator, which allows the sonographer to rest his or her arm while performing an US procedure. This system neglects 3-DOF and does not provide any force assistance during actual imaging. This paper reported high dissatisfaction from users following user studies.

Masuda et al. [35] present a 6-DOF three-legged robot parallel mechanism that uses the brightness of the ultrasound image to determine whether or not the probe is in contact with a patient's surface. Contact force from the body surface is not distinguished from the user's applied force. Therefore, it is not possible to know how much force is being applied by the probe against a patient while the probe is being manipulated.

Pierrot et al. [36] present a 6-DOF robotic arm used to hold an ultrasound probe. They use a damping control scheme to allow the sonographer to guide the probe to any number of desired sites. Once the probe head makes contact with the patient at a desired point, the user presses a teaching pendant, repeating this for any number of desired imaging points. Once this procedure is finished, the robot revisits each of these sites, applying a predefined force against the patient. This method does not allow the sonographer to manipulate the US probe and image as they normally would, changing the clinical workflow and reducing the chance of adoption.

1.7 Thesis Contributions

With the rise of WRMSDs in sonographers, the ultimate goal of this work is to develop a RUS framework that helps DMSs and VTs perform their job functions with few changes to the clinical workflow. The system presented herein aims to address the

limitations of existing US systems by helping reduce the strain on the sonographer. Ultimately, the overarching end-goals of this project are to minimize the occurrence of the WRMSDs common in the field and simultaneously improve ultrasound image quality. Both of these goals are met through a number of contributions presented in this thesis and summarized here:

- Application of human-robot cooperative, variable admittance control scheme to probe manipulation in US imaging. Makes use of an adaptive low pass filter shown in the literature to work well in interactive systems for reduced robot jitter and lag.

- Implementation of additional force-assistive capabilities. The first is force limiting, which sets a maximum on the probe-to-patient contact force. The second is automatic contact force application, which causes the robot to apply a preset force autonomously. The third and final is contact force locking, which once activated by the sonographer, ensures that the probe-to-patient contact force remains the same as that measured at the moment of activation.

- Design of a custom ultrasound probe holder for dual-sensing capabilities which allows the probe-to-patient contact force and forces that come from the sonographer's movements to be decoupled.

- Implementation of robot position-constraining control algorithms, known as Virtual Fixtures, to improve the Synthetic Tracked Aperture Ultrasound Imaging algorithm, which helps enhance the quality of deep-tissue US

images. This component was completed collaboratively with Kalyna Apkarian under the direct mentorship of Haichong Kai Zhang.

- Performance of user studies and phantom imaging experiments to assess extent of our system's force assistance and image quality-improvement capabilities.

1.8 Thesis Overview

This chapter has presented the motivation for this work, and introduced the approach used to the address the difficulties involved with US image acquisition, including image quality and sonographer injury.

Chapter 2 presents the design of our integrated system and detailed description of the admittance control and signal filtering algorithms used.

Chapter 3 describes the design and development of a dual-sensor force-augmenting custom US probe holder and the relevant control scheme. It also introduces the other force assistive capabilities, namely force locking, force limiting, and automatic contact force application.

Chapter 4 is dedicated to describing the setup, methods and results of user studies performed to compare our force assistive system to freehand, or unassisted, ultrasound imaging. Comparisons in image quality, participants' physical strain, and user opinions for both imaging techniques are presented.

Chapter 5 presents the use and mathematical formulations of Virtual Fixtures, sets of geometric constraints, used to limit or require certain robot behaviors. The chapter also

discusses the results showing the effects of these constraints on image quality using the Synthetic Tracked Aperture Ultrasound (STRATUS) imaging algorithm.

Chapter 6 offers a summary and conclusion of this work as well as existing limitations and future areas of research.

CHAPTER 2: PROPOSED CO-ROBOTIC SYSTEM AND ROBOT CONTROL FRAMEWORK

We present a robotic ultrasound (US) system that uses admittance force control for human-robot collaborative control of an US probe, with the additional benefit of input force augmentation to help reduce the amount of effort required from the sonographer.

For cooperative robot control, the admittance control approach is one that mimics the intuitiveness and ease of manipulation of typical freehand, or unassisted, US systems to which clinicians are accustomed. What results is co-robotic guidance that allows the sonographer to be in direct contact with the probe, always having full manipulability and control of the its placement, orientation, and contact force. Such a system also helps to reduce hand-tremor associated with applying high forces as well as any contact force variations caused by fatigue, leading to more stable and higher quality images. We also present the use of virtual fixtures, geometric constraints that limit or require certain robot motions, for specific imaging applications. Together, admittance force control, force scaling for assistive imaging, and virtual fixtures, provide a robotic ultrasound framework that provides intuitive control of the probe, similar to freehand ultrasound, but with added benefits.

Our new system for robotic assistance during US procedures makes use of a commercially available industrial robot, the Universal Robots UR5. When an ultrasonographer makes a motion to move the ultrasound probe freely in space, the forces applied are read by a 6-axis force and torque sensor at the robot end effector. These force readings are translated into linear and rotational velocity commands that are proportional and in the same direction as the measurement, leading to smooth, interactive motions of

the robot manipulator. When the probe is brought to an imaging area of interest, the robot can begin to provide force assistance to acquire desired images. At all times, the force being applied normal to the patient's anatomy can be measured and the robot's motion can be controlled based on the sonographer's input and this contact force. This method assists the sonographer while ensuring the forces being applied on the patient are within safe limits. The sonographer is able to lock the probe in place once a target site has been located on the image and even fully let go of the probe if desired, removing any strain on him or her. In certain cases, virtual fixtures can be activated to require more precise motions of the robot for particular applications.

An initial iteration of the admittance control algorithm for US imaging in the UR5 was implemented by Fereshteh Aalamifar of the Johns Hopkins University MUSiiC group using the URScript language. This implementation used linear admittance gains, a moving average filter, and sent the UR5 the resulting Cartesian velocities, without optimization. The author of this thesis extended this work by implementing it in Matlab, so that it would be easier to modify for different applications and so that it could be easily integrated with existing imaging algorithms, also written in Matlab. As described in this chapter, this extension makes use of non-linear admittance gains, the dynamic "1€" filter [37], and optimized joint velocities as the robot commands. The reasoning and benefits behind these changes are explained in the following sections.

2.1 System Setup

The overall system, shown in Figure 2.1, consists of one robotic arm, one 6-axis force sensor, one 1-axis load cell, and one US probe.

Robotic Arm

We used one 6-degree-of-freedom (DOF) UR5 robotic arm (Universal Robots, Odense, Denmark), which is able to carry a 5kg load, has an 850 mm in radius spherical reach, and 0.1 mm repeatability [38]. The robot can be controlled by sending URScript [39] commands to the UR5 controller. URScript is a language developed by Universal Robots, and allows communication with the force sensors and additional computers through TCP/IP connections.

6-Axis Force/Torque Sensor

One FT-150 (Robotiq, Lévis, Quebec, Canada) 6-Axis force and torque (F/T) sensor is used. The FT-150 is especially designed for robotic applications and connects directly to the UR5's robot controller. It has an outside diameter of 120 mm, a 100 Hz data

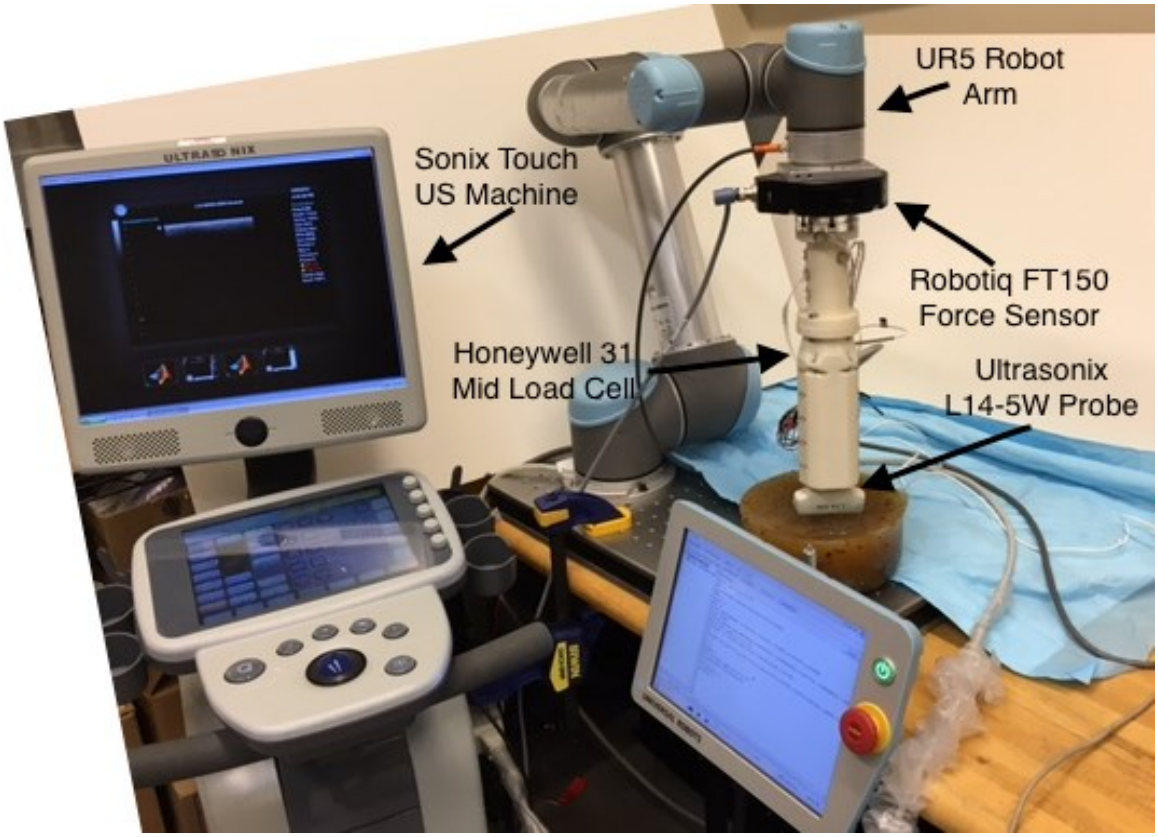

Figure 2.1 Integrated system setup consisting of UR5 robotic arm, Robotiq FT-150 force/torque sensor, Honeywell Model 31 Mid Load Cell and Ultrasonix ultrasound probe and machine.

transmission rate, a linear force measuring range of ±150 N and a torque measuring range of ±15 Nm. The FT-150 is attached to the robot tooltip and the US probe is attached to the sensor's tool interface.

Ultrasound System

One L14-5W 60 mm 128 array linear Ultrasonix US probe, together with the Sonix Touch US machine (Analogic Ultrasound, Richmond, BC, Canada), was used. A custom made US probe holder 3D printed using ABS and described in more detail in Chapter 4 was used to attach the US probe to the Robotiq FT-150 force sensor.

1-Axis Force Load Cell (inside probe holder in image)

One Model 31 Mid (Honeywell, Inc., Morris Plains, NJ, USA) load cell with a load capacity of 25 lbf (~111.21 N) was used. The load cell was placed inside the custom-made US probe holder and was used to measure any force applied directly to the probe head, independently from any force applied to the probe by the sonographer's hand. The setup for this sensor is explained and shown in further detail in Chapter 4.

2.2 Admittance Control Law

In our system, we use admittance force control of the UR5 industrial robot to achieve co-operative human-robot manipulation of an ultrasound probe. Admittance control takes measured forces/torques and produces a desired Cartesian velocity, $\dot{x}_{des} \in \mathbb{R}^{6x1}$. This is done with the following formulation:

$$\dot{x}_{des} = K\left(\begin{bmatrix} F_e \\ T_e \end{bmatrix}\right) \quad (2.1)$$

where $K \in \mathbb{R}^{6x6}$ is a diagonal matrix of scale factors, and $F_e \in \mathbb{R}^{3x1}$ and $T_e \in \mathbb{R}^{3x1}$ are the measured force and torque, respectively, measured at the robot's end effector (EE). As explained in Section 2.1: System Setup above, the force and torque applied by the sonographer on the ultrasound (US) probe during manipulation are read by the Robotiq FT-150 F/T sensor. The values of K are nonlinear admittance gains calculated as proposed in [40] in order to enable fine control for small applied forces, allow for faster motions for higher applied forces, and reduce the effect of noise in the force sensor readings. Overall, it does not require the gain value to be changed for different applications, as might be the case with linear gain values. The function that defines the gain value for each force dimension $i = x, y, z$ can be expressed as:

$$K_i = K_{max} \cdot e^{\left(1 - \frac{F_{e_{max}}}{\|F_{e,i}\|}\right)} \quad (2.2)$$

where K_{max} is an experimentally determined value that defines the maximum possible gain in any given direction, $\|F_{e,i}\|$ is the magnitude of the measured force in given dimension i, and $F_{e_{max}}$ is the maximum value permitted for $\|F_{e,i}\|$, set in order to ensure the gain is never so large that it causes dangerous robot velocities. An equivalent method is used to determine the nonlinear torsional admittance gains. The values of K_{max} were determined to be 0.125 for every degree of freedom (DOF). $F_{e_{max}}$ was set to 25 N for the linear axes and 5 Nm for the torsional axes. Additionally, in order to reduce the effect of sensor noise on the robot's behavior, a deadband ($\pm d$) of ± .1 N and Nm was selected for both the force and torque components. Therefore, whenever the magnitude of $F_{e,i}$ or T_e, i are less than ±.1 N or Nm, respectively, K_i for that component will be 0. The end result is a gain for each of the 6 DOF that varies from -K_{max} to K_{max} in a sigmoidal pattern. An

example gain vs. force relationship for a linear force channel is shown in Figure 2.2. The sigmoidal shape avoids any sharp transitions at the$\pm d$ and $\pm F_{e_{max}}$ regions but guarantees an almost linear gain elsewhere.

Before the resulting desired EE Cartesian velocities can be sent to the robot, they must be transformed from the robot EE frame e to the robot base frame b. The relationship between the force sensor input and the robot base can be the defined by a transformation $g_{be} \in SE(3)$, defined as in [41]:

$$g_{be} = \begin{bmatrix} R_{be} & p_{be} \\ 0_{1x3} & 1 \end{bmatrix} \quad (2.3)$$

where $R_{be} \in SO(3)$ represents a rotation matrix that relates the robot's end effector frame to that of the robot's base and $p_{be} \in \mathbb{R}^{3x1}$ is the spatial displacement between the two frames. (2.3), determined using the forward kinematics of the robot, as described in

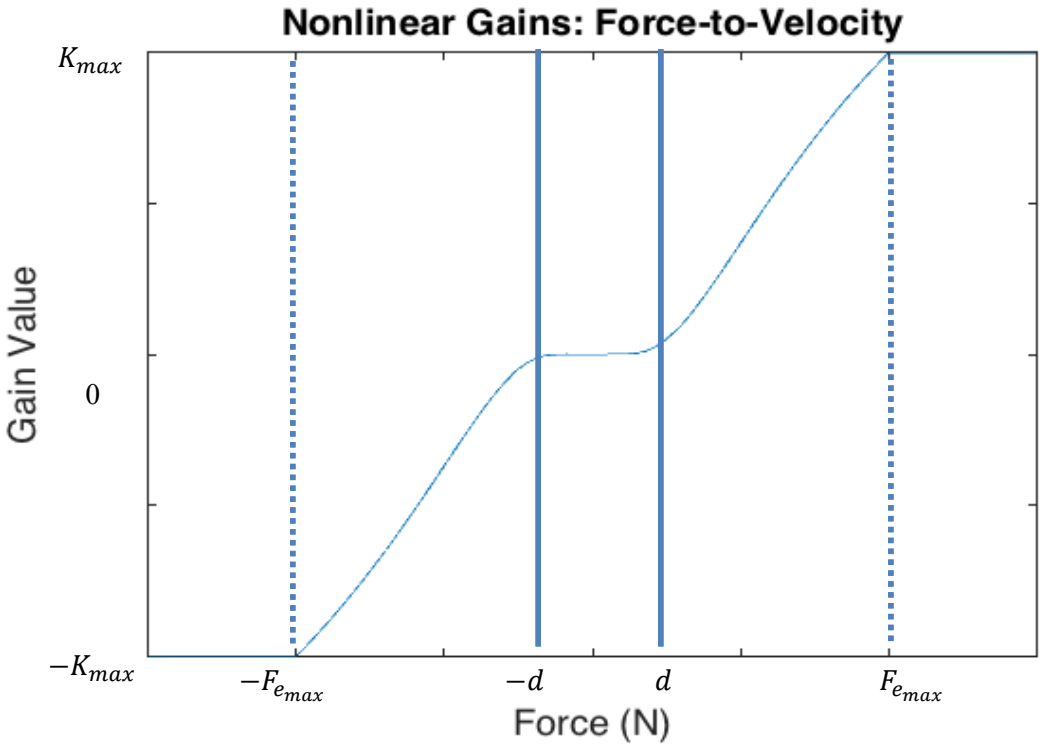

Figure 2.2 Sigmoidal relationship between input force and gain for one of the linear force channels. Solid lines demarcate the boundaries of the dead zone while the dotted lines demarcate the upper and lower force thresholds

appendix A. The relationship of the end effector velocity $\dot{x}_{des}$ calculated in (2.1) to its corresponding value in the robot base or world frame is defined as:

$$\dot{x}_{des}^{base} = Ad_{g_{be}} \cdot \dot{x}_{des} \quad (2.4)$$

where $Ad_{g_{be}} \in \mathbb{R}^{6x6}$ is the adjoint transformation associated with coordinate transformation g_{be}:

$$Ad_{g_{be}} = \begin{bmatrix} R_{be} & \hat{p}_{be}R_{be} \\ 0_{3x3} & R_{be} \end{bmatrix} \quad (2.5)$$

$\hat{p}_{be} \in so(3)$ is the skew symmetric matrix associated with the vector p_{be}. Namely, given $p_{be} = \begin{bmatrix} p_{be_1} \\ p_{be_2} \\ p_{be_3} \end{bmatrix}$,

$$\hat{p}_{be} = \begin{bmatrix} 0 & -p_{be_3} & p_{be_2} \\ p_{be_3} & 0 & -p_{be_1} \\ -p_{be_2} & p_{be_1} & 0 \end{bmatrix} \quad (2.6)$$

2.3 Signal Filtering

Since the robot commands are highly dependent on the forces measured by the FT150, the system must be robust enough to reject noisy signals and quickly adapt to sudden changes in the magnitude and direction of a user's applied force. Using solely the input force signal for each time step in the robot control leads to significant robot jitter, seen in Figure 2.3. In the image, the blue curve represents the robot velocities expected given the force readings at each time step, while the orange line shows filtered robot velocities at each time step. Given the difference between the trajectories of the two curves, it is clear that there is significant jitter in the robot control when the signal is not filtered. In order to smoothen out the robot movement in relation to the force inputs, the command velocity sent to the robot is passed through an implementation of the "1€" filter, a low-pass

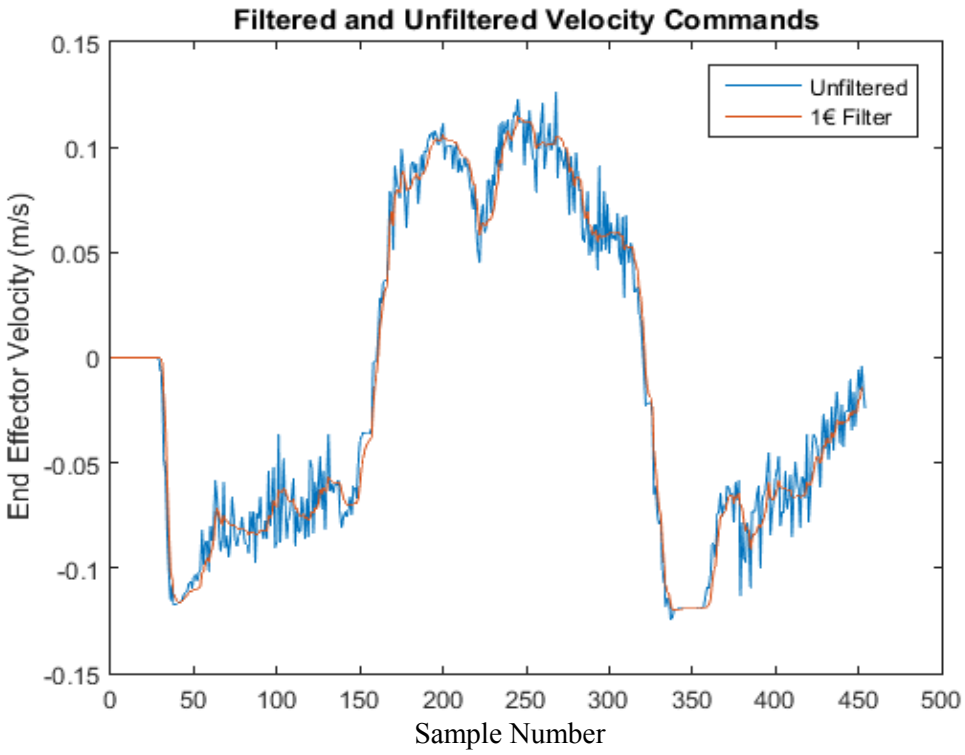

Figure 2.3 Smoothing effect of 1€ filter on velocity commands. Blue curve represents unfiltered and orange represents filtered values. Collected from the X-velocity values of robot manipulation in real-time

filter developed for use with noisy input in interactive systems [41]. As explained by its developers, the "1€" filter uses a first order low-pass filter with an adaptive cutoff frequency to account for human's higher sensitivity to jitter at low speeds and higher sensitivity to lag at higher speeds. Applied to our system, when a user applies low force or torque magnitudes at the ultrasound probe, expecting the robot to move at a low velocity, the cutoff frequency is low, reducing jitter in the robot. When the user applies a higher force magnitude, expecting a higher robot end-effector velocity, the cutoff frequency increases proportionally in order to reduce lag in the system. This filter is very similar to an exponential smoothing moving average filter, seen in (2.7).

$$s_0 = x_0;\ s_t = \alpha x_t + (1-\alpha)s_{t-1}, \qquad t > 0,\ 0 < \alpha < 1 \quad (2.7)$$

This is an iterative calculation where x_t is the unfiltered sensor output at time t, α acts as a constant smoothing factor between 0 and 1, which weighs the value of x_t, s_t is the output

of the filter at time t, $s_{t-1}$is the filter output at time $t-1$ and $(1-\alpha)$ weighs the previous output. The "1€" filter is different from standard exponential smoothing filters in that while in the regular exponenial smoothing, the weighting between current and past readings, shown in (2.7) as α and $(1-\alpha)$ respectively, their values change dynamically in the "1€" filter as a function of the rate of change the signal. This can be seen below:

$$\alpha = \frac{1}{1+\frac{\tau}{T_e}} \quad (2.8)$$

where T_e is the sampling period and

$$\tau = \frac{1}{2\pi f_c} \quad (2.9)$$

where

$$f_c = f_{c_{min}} + \beta \left|\dot{\hat{X}}_i\right| \quad (2.10)$$

$\dot{\hat{X}}_i$ in (2.10) is the rate of change of the filtered output, calculated at each step. $f_{c_{min}}$ and β are the only two variables that need to be tuned in the filter and are the minimum cutoff frequency and slope, respectively. If the value of $\dot{\hat{X}}_i$ is high (the user is moving the robot quickly), then f_c will grow accordingly in order to reduce lag. When $\dot{\hat{X}}_i$ is low (the user is moving the robot quickly), the user would be more sensitive to jitter and f_c is therefore set closer to its minimum value, filtering out the greatest proportion of noise.

Combining this with the general admittance control law (2.1), the resulting velocity commands for each time step can be summarized as:

$$\dot{x}_t = \alpha\left(\frac{d\dot{x}}{dt}\right) \cdot K\left(\begin{bmatrix} F_e \\ T_e \end{bmatrix}\right) + \left(1-\alpha\left(\frac{d\dot{x}}{dt}\right)\right) * \dot{x}_{t-1}; \quad t > 0 \quad (2.11)$$

The second component on the right-hand side of (2.11) is the previous Cartesian velocity command, scaled by $\left(1-\alpha\left(\frac{d\dot{x}}{dt}\right)\right)$. As with a standard exponential smoothing filter, this

second component contains information from all past velocity commands, with the more recent commands making a greater contribution. The decay of the contribution of velocities found in the more distant past is determined by the value of α. Again, since in the "1€" filter α changes based on the rate of change of the velocity commands, a lower rate of change will give a lower α value, leading to a higher contribution for past values, and therefore less jitter. A higher rate of change has the opposite effect, leading to a faster decay of the contribution of past values and therefore less lag. It is because of this robustness that the "1€" filter was chosen over a simple moving average filter or a standard exponential smoothing filter, which cannot change their weighting dynamically and therefore require one to sacrifice either jitter or lag for the other. Again, the effects of the "1€" filter on one of the velocity channels can be seen in Figure 2.3. The blue curve represents the raw, unfiltered velocity commands, while the orange curve represents the effect of applying the "1€" filter in real-time. It is clear that when the "1€" filter is applied the resulting velocity command is significantly smoothened. This accuracy is particularly important in ultrasound imaging given the need to accurately track the probe location in relation to the resulting images. If too much lag or jitter were present, the calibration of the ultrasound probe would be made impossible by the randomness in the noise. An alternate smoothing method that was initially tested, a weighted moving average filter, is described in Appendix 2. The "1€" filter was selected over the weighted moving average filter because of the latter's propensity to add lag to a system and reduce responsiveness, problematic in robotic control applications. Given the "1€" filter's balance of lag and adaptability, it was the more suitable choice.

2.4 Joint Velocity Command Calculations

Cartesian velocity commands calculated in (2.4; unfiltered) or (2.11; filtered) are converted to robot joint velocities using the Jacobian matrix, $J \in \mathbb{R}^{6x6}$, whose calculation is explained in Appendix 3. In the case of a 6 degree of freedom (DOF) robot such as the UR5, the Jacobian is composed of six columns, all describing the time derivative of the kinematics equations of the robot. The Jacobian is dependent on the position of each joint at a certain point in time and relates robot joint rates to the linear and angular velocity of the end-effector:

$$\dot{x}_{des} = J\dot{q}_{des} \quad (2.12)$$

Given the desired Cartesian EE velocity, the corresponding joint angular velocities $\dot{q} \in \mathbb{R}^{6x1}$ can be calculated by:

$$\dot{q}_{des} = J^{-1}\dot{x}_{des} \quad (2.13)$$

Since the Jacobian matrix must be inverted for this formulation to work correctly, this method breaks down at configurations of the robot where the Jacobian loses rank (its columns become linearly dependent), known as kinematic singularities. A different approach to solve for $\dot{q}_{des}$, explained by Funda et al. [42], consists of a linear least squares optimization framework, with the following objective function:

$$\dot{q}_{des} = \underset{\dot{q}_{des}}{\operatorname{argmin}} \|J\dot{q}_{des} - \dot{x}_{des}\| \quad (2.14)$$

The optimization solver generates the best set of $\dot{q}$ that will minimize the two-norm motion error of the robot. This vector is then sent as a joint velocity command to the UR5. Using this optimization framework avoids cases where the Jacobian is uninvertible, and also permits for the constraining of the robot motion. One such constraint that is applied for safety reasons is that of joint velocity limits, which limit the range of speeds at which

the robot is allowed to move. This modification to the control law is particularly important in the manipulation of robots in medical procedures, where patient and clinician safety can be compromised by the rapid swinging of a robot manipulator. Therefore, (2.14) can be set to be subject to $\dot{q}_{low} \leq \dot{q}_{des} \leq \dot{q}_{up}$. As described by [43-45], any constraint added to the optimizer framework takes the form of

$$H\dot{q}_{des} \leq h \quad (2.15)$$

where H, the constraint coefficient matrix and h, the constraint vector, are structured in a way to define the desired behavior of the system. For example, in the case of the joint velocity range limits, the H matrix and h vector are formulated as follows:

$$H_{joint} = \begin{bmatrix} -I_{6x6} \\ I_{6x6} \end{bmatrix} \quad (2.16)$$

$$h_{joint} = \begin{bmatrix} \dot{q}_{low} \\ \dot{q}_{up} \end{bmatrix} \quad (2.17)$$

where I_{6x6} is the 6x6 identity matrix. For this implementation, $\dot{q}_{low} = \dot{q}_{up} = 0.5\, rad/s$. When joint velocity limits are the only constraint in the system, H and h from (2.15) are equal to H_{joint} and h_{joint}, respectively The optimization framework can accept a number of additional constraints, some of which are referred to as Virtual Fixtures (VFs), described in further detail in Chapter 5.

2.5 Summary

Overall, the use of admittance control, velocity filtering, and optimized joint velocity calculations allows us to set up the environment required for collaborative human-robot interaction. This control scheme allows the user, in this case a sonographer, to have full control of the behavior of the robot based on his or her force input at the robot wrist. Admittance control gives the sonographer the same probe-manipulability as that of

freehand ultrasound, plus the benefits of robotic assistance. It is this framework atop which we build our system's force-assistive features including force augmenting, locking, and limiting, all discussed in chapter 3, as well as our implementation of Virtual Fixtures for Synthetic Tracked Aperture Ultrasound, discussed in chapter 5.

CHAPTER 3: DUAL FORCE SENSOR TOOL AND CONTACT FORCE CONTROL

3.1 Introduction

In order to assist a sonographer in applying a desired force against a patient, we have developed a force assistive algorithm that augments the effort of the user such that less strain is required to maintain a stable and viable ultrasound image. This method is particularly useful when an ultrasound procedure is being performed on an obese patient whose extra layers of tissue require that the clinician exert a higher force in order to reach and clearly visualize the imaging region of interest. Force scaling can help reduce the amount of force that the sonographer has to apply by augmenting smaller efforts, thereby reducing the strain on the clinician. This can help reduce an ultrasonographer's chance of developing a work-related musculoskeletal disorder (WRMSD), which affects 63-91% of sonographers [11-16]. Additionally, applying high forces for extended periods leads to muscle fatigue and hand tremor. When a sonographer is imaging, this tremor propagates through the ultrasound probe, and can affect the quality of the resulting images. Augmenting the force of the sonographer therefore has the added benefit of reducing the magnitude of operator hand tremor, leading to an improved image quality. The overall expected result of this system is improved image stability and a reduction in the strain to its users.

3.2 Relevant Control Law

In order to scale the clinician-applied force into the desired robot motion, a method to measure the contact force at the probe head is required. Using this measurement, an

updated control law is applied, presented as a modification to (2.1) and similar to that used for the Johns Hopkins University (JHU) Eye Robot [6,7,46]:

$$\dot{x}_{des} = K\left(\begin{bmatrix} F_e \\ T_e \end{bmatrix} - \gamma \begin{bmatrix} F_{et} \\ T_{et} \end{bmatrix}\right) \quad (3.1)$$

where as before, F_e and T_e are the force and torque, respectively, which define the force applied onto the probe handle by the clinician during its manipulation, measured at the robot end effector. γ is the scaling factor that will augment the contact force the clinician applies onto the surface of the patient and lead to force assistance. F_{et} and $T_{et}$are the force and torque, respectively, measured by the load cell inside the probe holder resolved at the robot end effector with the following transformation:

$$\begin{bmatrix} F_{et} \\ T_{et} \end{bmatrix} = Ad^T{}_{g_{et}} \begin{bmatrix} F_{tt} \\ T_{tt} \end{bmatrix} \quad (3.2)$$

where $\begin{bmatrix} F_{tt} \\ T_{tt} \end{bmatrix}$ represents the measured contact force values in the frame of the load cell.

Given the coordinate frame transformation $g_{et} = \begin{bmatrix} R_{et} & p_{et} \\ 0 & 1 \end{bmatrix}$, as described in (2.3), then

$$Ad^T{}_{g_{et}} = \begin{bmatrix} R_{et} & \hat{p}_{et}R_{et} \\ 0 & R_{et} \end{bmatrix}^T = \begin{bmatrix} {R_{et}}^T & 0 \\ -{R_{et}}^T\hat{p}_{et} & {R_{et}}^T \end{bmatrix} \quad (3.3)$$

As mentioned, two sensors are required for this purpose in order to decouple the force applied voluntarily by the sonographer when manipulating the ultrasound probe and the contact force applied against a patient's anatomy. The forces at the robot wrist were measured by by the Robotiq FT 150 while axial forces perpendicular to the US probe head are measured by the Honeywell Model 31 Mid load cell. This load cell is only capable of measuring forces in a single direction, installed to be in the Z-axis of the probe and robot end effector, referred to as F_{et_z}. Since the majority of forces during ultrasound procedures are applied in this axis, this is sufficient for our purposes. Due to this, (3.1) reduces to:

$$\dot{x}_{des} = K \left(\begin{bmatrix} F_e \\ T_e \end{bmatrix} - \gamma \begin{bmatrix} 0 \\ 0 \\ F_{et_z} \\ 0 \\ 0 \\ 0 \end{bmatrix} \right) \quad (3.4)$$

In order to decouple the forces measured by each sensor and ensure that the Honeywell load cell does not detect any manipulation forces, a custom US probe holder, described in detail in the next section, was designed.

3.3 Design of Custom Ultrasound Probe

The custom probe holder was created in Solidworks (Dassault Systèmes, Vélizy-Villacoublay, France) to fit the 60 mm 128 linear array ultrasound probe used in these studies, but a similar design can be created for other ultrasound probes. As previously mentioned, the purpose of this custom probe holder is to decouple the force applied by the clinician's manipulation of the probe from any contact force applied by the probe onto the patient. While the six-axis Robotiq FT150 rigidly attached to the robot end effector picks up information from both force sources, a one-axis load cell, placed inside the probe holder, is expected to only pick up forces from objects in contact with the probe.

Various iterations of this custom holder, all made using additive manufacturing with Acylonitrile-Buadiene-Styrene (ABS), have been designed and tested; the first design can be seen in Figure 3.1 below.

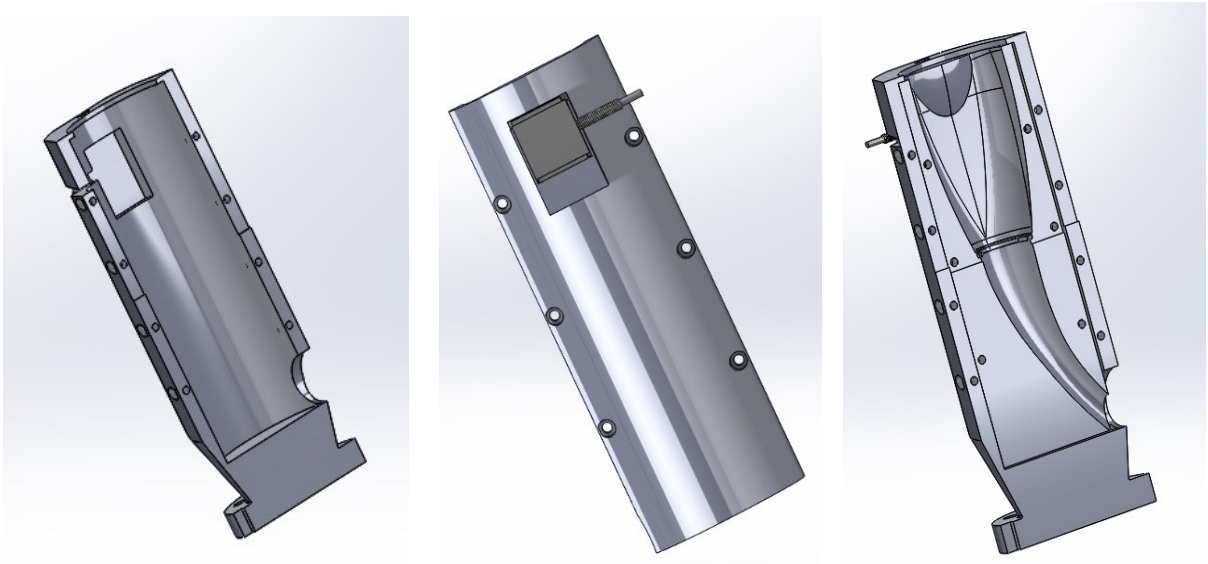

Figure 3.1 CAD drawing of first probe holder design

The design consists of two half clam-shell components, one which fits inside the other. The inner component clamps itself around the ultrasound probe. In this first design, the LSB200 10 lb JR S-Beam Load Cell (Futek, Irvine, California, USA) is placed inside

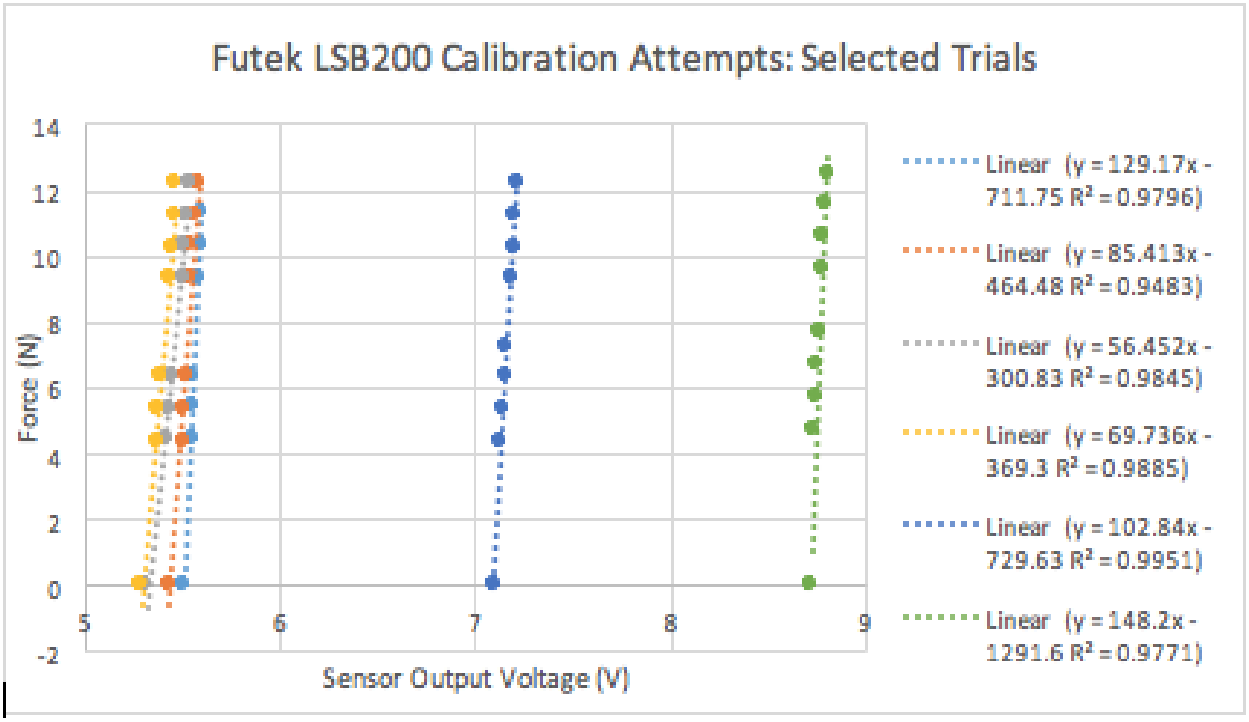

Figure 3.2 Selected trials in Futek LSB200 calibration for first design iteration

a groove found parallel to the probe. The load measures forces normal to its axial direction and has a force capacity of 10 lbs (approximately 44.4822 N), sufficient for ultrasound applications. The outer component clamps itself around the inner component, itself having a groove into which the Futek load cell fits. The other end of the holder is attached rigidly to the end effector of the UR5 robot. In theory, any force against the load cell would make the inner component shift linearly along the path guided by the outer component.

However, after preliminary testing it was found that the system did not behave reliably. Various attempts at relating the force applied at the robot head with the load cell output showed inconsistencies, as seen in Figure 3.2. Across trials, the zero value of the measured output was inconsistent. A possible technique used to circumvent this problem would have been to allow the user voluntarily to zero the Futek load cell by activating a microswitch or pressing a button on a user interface. However, more critical in the calibration procedure is the slope of the force vs. output voltage relationship. As seen in the equations of the best-fit line for each trial in the figure, this value also varied significantly across calibration attempts, making it virtually impossible to rely on the measured data. The next iteration of the holder design aimed at reducing the difference in slopes across trials. To do this, a number of changes were implemented.

First, the placement of the load cell was changed. In the original design, the load cell was found in parallel with the force applied at the probe head, in an arrangement that made the whole system unsymmetrical. This likely led to inconsistent and unrepeatable deformation of the load cell. Additionally, the rectangular geometry of the Futek LSB200 and its relatively high deflection of 100μm affected the symmetry of the design and reduced the sensor's propensity to return to its original zero position, making the output vary

significantly across trials. Additionally, the large contact surface areas between the inner and outer components of the holder added significant and non-predictable static friction that made it difficult to ensure that the sliding inner component returned to its original position.

A way to mitigate the problems associated with the load cell's placement and geometry was to relocate the load cell and to switch to the Honeywell Model 31 Mid load cell, shown in Figure 3.3., which has a maximal load of 25 lbf (, and a deflection of only 30 µm. This sensor requires an instrumental amplifier for signal detection. In this case, the INA125P (Texas Instruments, Dallas, TX, USA) is used.

In the second iteration of the US probe holder, seen in Figure 4.4, this load cell is placed at the bottom of the outer holder and in series with any force applied at the probe head. Additionally, the circular shape of the load-bearing surface ensures that the load is

Figure 3.3 Honeywell Model 31 Mid 25 lbf load cell

measured symmetrically. As shown in the top middle panel in Figure 3.4, a large portion of material was also removed from the inner component in order to reduce the friction caused by the surfaces in contact with each other. However, some remaining extruding material is necessary to ensure that the inner component is guided by the inner walls of the outer shell. This allows the inner component to move in a linear fashion in relation to the outer shell, reduce any torsional displacement, and thereby reduce the occurrence of uneven deformation of the load cell. Lastly, as seen in the bottom panel of Figure 3.4, two

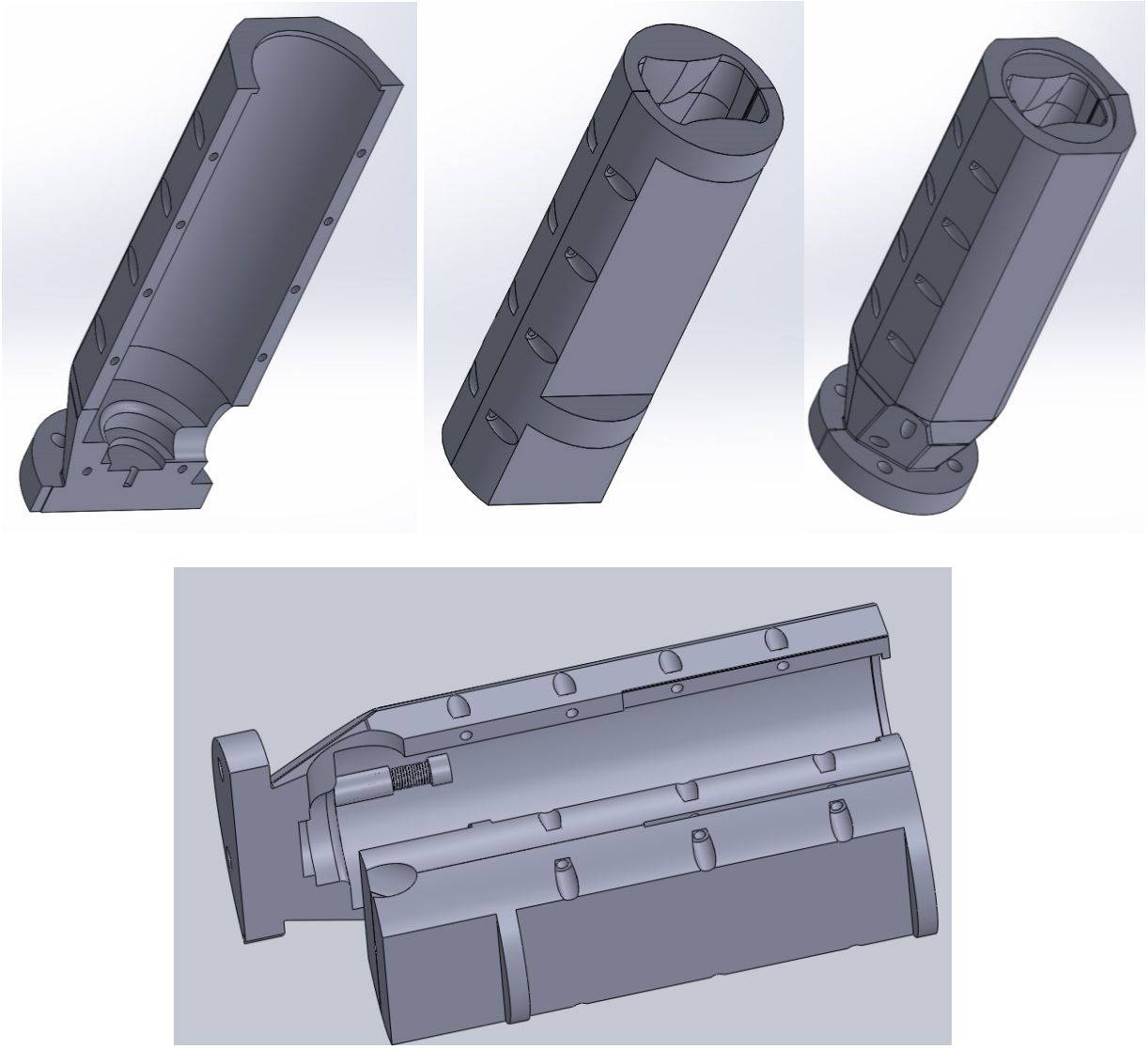

Figure 3.4 Second Design Iteration. The load cell is relocated to be at the bottom of the outer component, a large amount of material is removed from inner component, and a spring loaded mechanism is added to ensure the probe returns to its resting posit

spring loaded mechanisms were added between the inner and outer components to provide a constant force pushing the inner shell away from the load cell and back to its starting position when no force is applied at the head of the probe.

This design helped to increase the consistency and repeatability of the force measurement system, as seen in Figure 3.5.

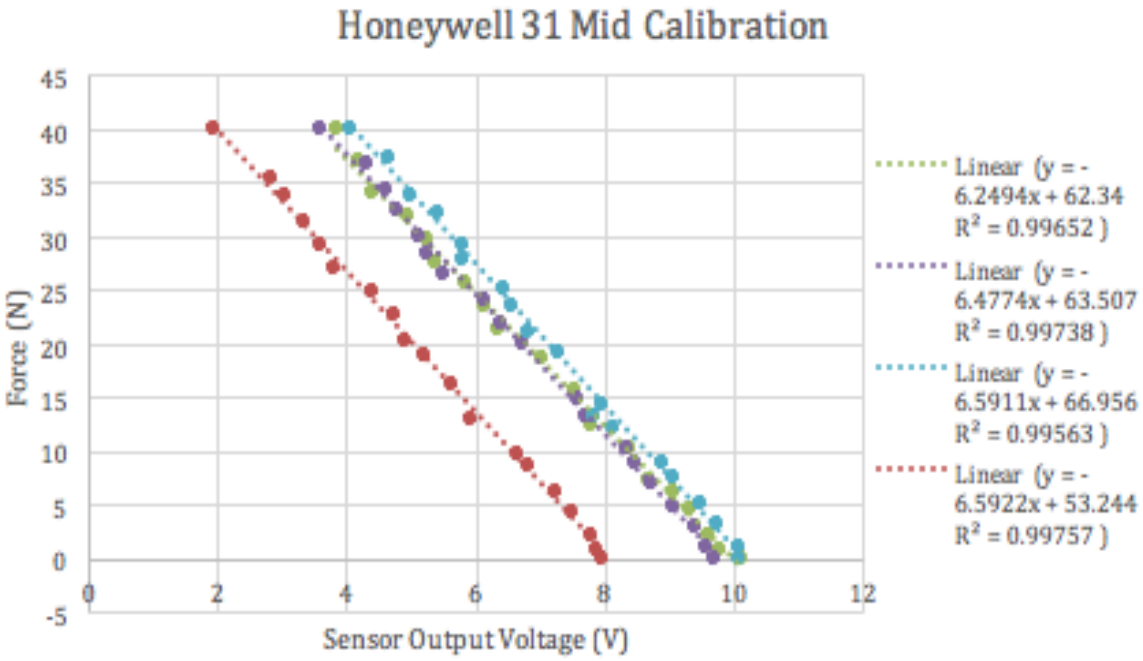

Figure 3.5 Calibration of Honeywell 31 Mid load cell. The changes in the probe holder design make the relationship between the applied force and the sensor output voltage significantly more repeatable than with the Futek LSB200

While the relationship between force and voltage, shown as the slope in the graph is now nearly constant, the readings at each force value are still not, as also seen by the varying y-intercepts of the lines of best-fit in the figure. A simple, short-term solution to this problem is to provide a method for the user to zero the load cell whenever desired, such as through the use of a button on a user interface.

In order to ensure that the load cell inside the probe holder was unable to measure any forces coming from a user's hand, an additional component was placed in between the robot end effector and the probe holder. This handle is shown in Figure 3.6 and allows for

the comfortable manipulation of the US probe, similar to that customary in freehand ultrasound, while allowing for the accurate integration of the aforementioned dual sensing paradigm. Again, while this is a convenient and effective short-term solution, it does have the problem of making the probe holder very long and somewhat awkward to manipulate. Ideas of how to improve this will also be touched upon in the *Future Design Changes* section that follow

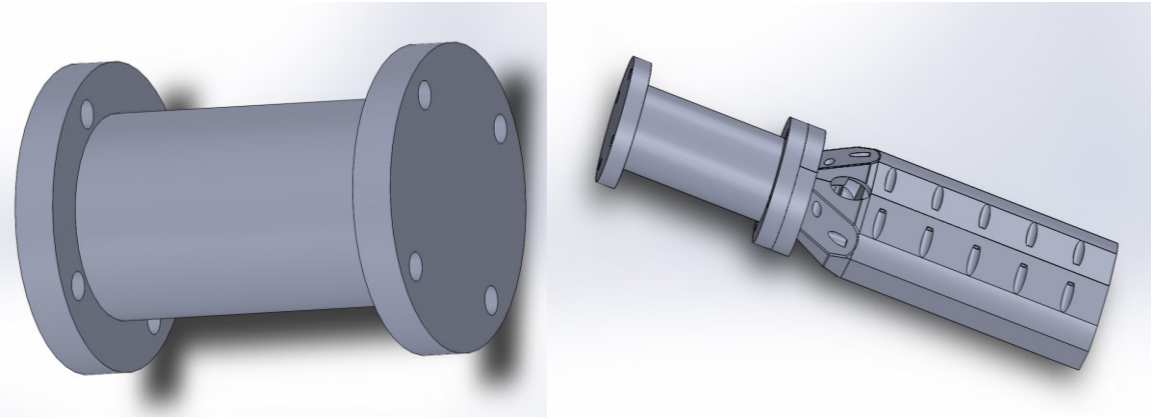

Figure 3.6 Handle added to design to reduce effect of manipulation forces on load cell

3.4 Future Design Changes

In order to improve the performance of the probe holder and end its dependency on the additional handle, several potential changes have been considered. One such change is the use of aluminum instead of ABS to create the inner sliding component of the holder. Aluminum, compared to ABS, has a much lower coefficient of friction, is non-porous and can therefore be greased if necessary, deforms little, and has smooth, even surfaces, unlike the results of 3D-printed plastics. This could help reduce the friction between the two components, allowing for improved consistency in the device's behavior. Another potential design change is to add spring plungers in between the inner and outer components to assist in reducing the friction between the two pieces and to better guide the inner component. Future changes will aim at fully decoupling the contact force from the force sensed at the

robot end effector and at making the co-robotic imaging procedure as comfortable as possible.

3.5 Variable Admittance Control

The admittance gains shown in (3.1) are isotropic. In this case, as the measured contact force increases, it has a higher effect on the control law, making it increasingly more difficult for the user to move the probe in the desired direction. Therefore, in order to make the force assistance smoother for the user, we introduce anisotropic gains, similar to that presented in [6]:

$$\dot{x}_{des} = K\left(A_e \begin{bmatrix} F_e \\ T_e \end{bmatrix} - \gamma A_{et} \begin{bmatrix} F_{et} \\ T_{et} \end{bmatrix}\right) \quad (3.5)$$

where the new components, A_e and A_{et}, are diagonal admittance matrices associated with the force measured by the force sensor at the robot end effector and the contact force measured by the load cell inside the custom probe holder, respectively. When $A_e = A_{et} = I$, (3.5) reduces to (3.1). The values of these diagonal admittance gain matrices are dependent on the contact force measured by the load cell. When the ultrasonographer first begins to apply a force against a patient's body, the contact force should have a significant impact on the robot control such that it augments the clinician's motion and assists in the force application. As the sonographer continues to apply a gradually increasing force, the effect of the contact force should steadily decrease such that the probe can be held steady at any desired tissue displacement depth with little effort, and lifted off comfortably when desired. To this end, we define:

$$A_e = diag([1, 1, 1 + \beta, 1, 1, 1]^T) \quad (3.6)$$

$$A_{et} = diag([1, 1, 1 - \beta, 1, 1, 1]^T) \quad (3.7)$$

where $\beta \in [0,1]$ varies with the contact force. As shown in Figure 3.7, the value of β increases linearly with the measured contact force, once it has surpassed a given threshold f_{lb}. It plateaus at its highest possible value, 1, once the contact force reaches the given upper bound f_{ub}.

When the contact force is below f_{lb}, the admittance control law reverts to (3.1). When it is higher than f_{ub}, the gain for the wrist force sensor is double that of (3.1) and that for the load cell is cut in half, ensuring the sonographer continues to have full control of the probe at all times.

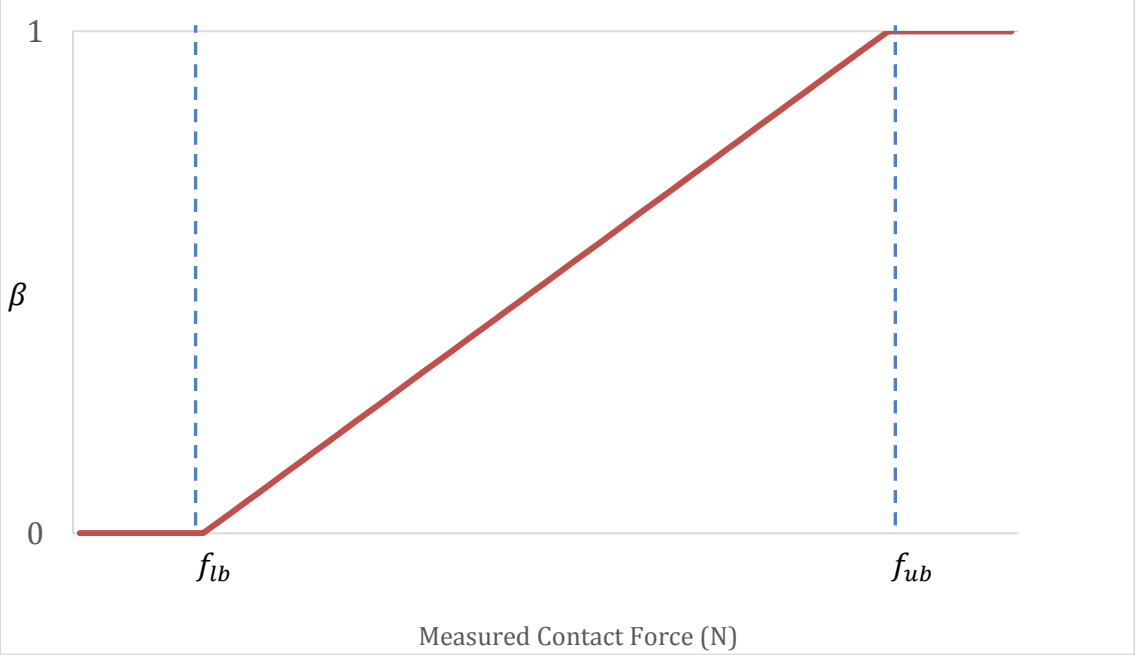

Figure 3.7 Effect of measured contact force on value of β.

3.6 Contact Force Locking

In certain situations, the sonographer might choose to lock the probe in place, allowing him or her to fully let go of the probe while maintaining a desired probe location, and contact force and, thereby, the desired ultrasound image. To do this, the sonographer

can simply apply a "twist" motion on the probe around its Z-axis. The Robotiq 6-axis F/T sensor will measure the torque applied and send a command to lock the current position – by setting all joint velocities to 0 rad/s – whenever there is a sudden torque measurement of 1 Nm or greater around its axial direction. The position can be unlocked by repeating the same motion, giving the user the same collaborative compliant force control he or she originally had. This force locking in action is shown in figure 3.8 below. In the image, the orange curve depicts the Honeywell Mid 31 load cell reading of the contact force and the blue shows the torque measurement around the axial direction of the probe, sensed by the FT150. As shown, when there is a sudden change in the torque measured, the contact force remains steady at the current contact force, in this case, approximately 25 N

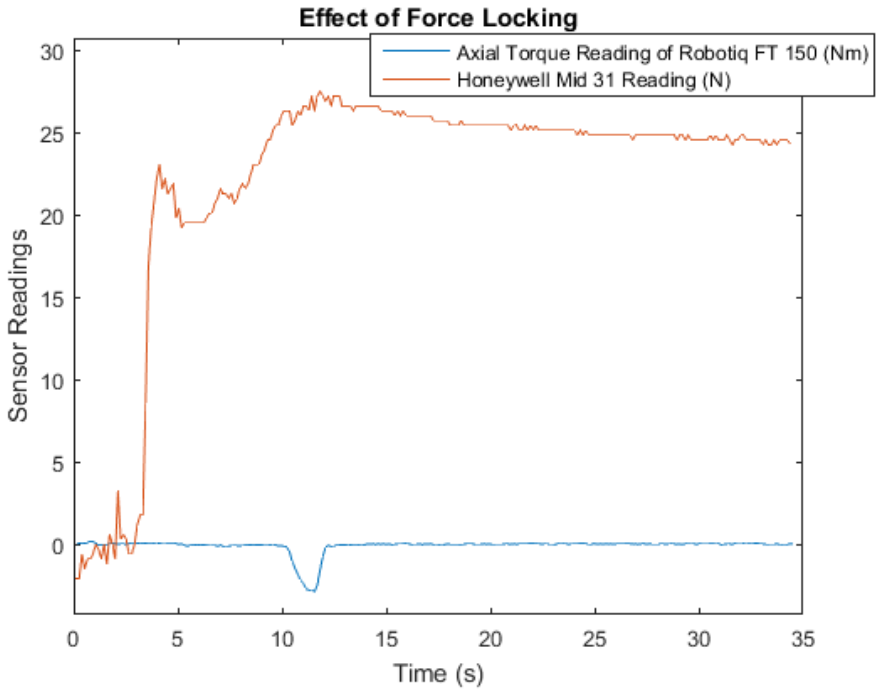

Figure 3.8 Effect of rapidly twisting the probe on contact force: robot does not move and contact force remains constant even if the probe is let go.

3.7 Contact Force Limiting

The effort augmenting capabilities of this system allow the user to apply any desired force onto the patient surface, while receiving robot assistance in the process. In practice, this can be dangerous to the patient since too high of a force applied on a patient's anatomy can cause significant damage to the surrounding tissue. Therefore, we seek to limit the contact force applied in the axial direction of the US probe as measured by the load cell inside the probe encasing. In short, the current force, f_{curr} plus any change in force, Δf must be less than or equal to the maximum force f_{lim}: $f_{curr} + \Delta f \leq f_{lim}$. From (2.1), the definition of the time derivative, $\dot{x} = \frac{\Delta x}{\Delta t}$, and the definition of material compliance, $K = \frac{\Delta x}{\Delta f}$, $\Delta f = \frac{\dot{x}\Delta t}{K}$, and therefore,

$$f_{curr} + \frac{\dot{x}\Delta t}{K} \leq f_{lim} \quad (3.8)$$

Solving for $\dot{x}$ leads to

$$\dot{x} \leq \frac{K(f_{lim} - f_{curr})}{\Delta t} \quad (3.9)$$

This is applied to the control law of the robot by adding an additional constraint to the optimization framework explained in Section 2.3 above. The constraint coefficient matrix H_{lim} and the corresponding constraint vector h_{lim} are calculated as follows:

$$H_{lim} = Ad_{g_{bt}} I_{6x6} \quad (3.10)$$

$$h_{lim} = \frac{K(f_{lim} - f_{curr})}{\Delta t} \quad (3.11)$$

where $Ad_{g_{bt}}$ is the adjoint transformation that resolves the velocities associated with the force measured by load cell in its own coordinate frame to the frame of the robot base:

$$Ad_{g_{bt}} = Ad_{g_{be}} \cdot Ad_{g_{et}} \quad (3.12)$$

where $Ad_{g_{be}}$ is defined in (2.5) and $Ad_{g_{et}}$ is defined in (3.3). Combining this constraint with the joint velocity limits, defined in (2.13) and (2.14), the optimization problem becomes:

$$\dot{q} = \underset{\dot{q}}{\operatorname{argmin}} \|J\dot{q} - \dot{x}\| \quad (3.13)$$

$$s.t \begin{bmatrix} H_{lim} & 0 \\ 0 & H_{joint} \end{bmatrix} \begin{bmatrix} J(\theta) \\ I_{6x6} \end{bmatrix} \dot{q} \leq \begin{bmatrix} h_{lim} \\ h_{joint} \end{bmatrix} \quad (3.14)$$

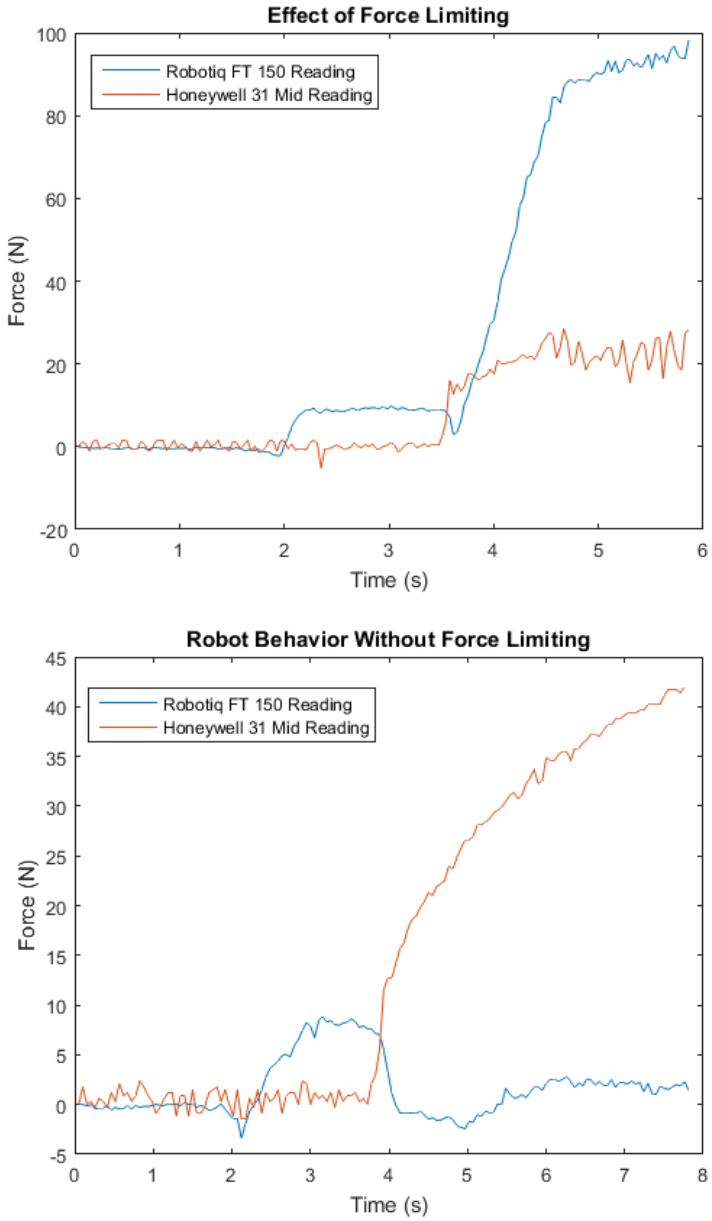

Figure 3.9 Effect of force limiting on permitted forces and robot behavior. (a) Contact force is limited to 20 N. (b) No force limit is set.

where $J(\theta)$ is the robot's Jacobian matrix and works to convert the Cartesian spatial constraints defined by H_{lim} and h_{lim} into their corresponding configuration space (joint angle) constraints. This is not required for H_{joint} and h_{joint}, defined in 2.13 and 2.14, respectively, because these joint velocity limits are already defined with regards to the joint angle velocities. Additional constraints can be added to the optimization problem by appending the associated constraint coefficient matrices and constraint vectors to H and h, respectively. The effect of activating force limiting with an f_{lim} value of 20 N is shown in Figure 3.9 (a). The blue curve depicts the measurement from the Honeywell 31 Mid load cell while the orange presents that of the Robotiq FT150 force sensor. As seen, when activated, force limiting stops the robot from applying any force above 20 N, despite the input from the user being significantly higher than that. For comparison, the force behavior without limiting is shown in Figure 3.10 (b), where the value of the contact force can increase with no bounds. In practice, a limit of around 25-40 N would be set for safety purposes.

3.8 Automatic Contact Force Application

An alternative method of force assistance is one in which the sonographer sets a desired contact force and allows the robot to approach this force autonomously. Once the sonographer has used collaborative control to move the US probe to the desired imaging location, this autonomous assistive imaging can begin. As opposed to the force scaling assistance described in previous sections of this chapter, the robot can approach this force setting without any interaction from the sonographer. The robot will apply the selected force in order to reach the desired imaging region of interest. This force will vary across

various types of ultrasound exams performed but will typically stay within the range of 5N-20N [47]. However, this value can be much higher in certain cases, such as with obese patients [13]. In one implementation, the sonographer is asked to input the desired application force at the point when the system is first started or to actively change it by inputting a desired value in a User Interface. Given that the forces at the robot end effector and the contact force at the probe head are decoupled, the sonographer still has the ability to move the probe in any direction to adjust the probe if necessary. However, the robot will always push to reach the set force and might work against the sonographer in this case. Originally, a PID controller was used to accurately approach the desired set force. This PID controller is explained in Appendix 4.

An alternate method, which was ultimately selected for its robustness, smooth integration into the existing framework, and fewer number of parameters, makes use of the optimization framework originally defined in (2.11). In this case, we allow the current force f_{curr} plus any change $\Delta f = \frac{\dot{x}\Delta t}{K}$, to stray away from the preset desired force f_{des} by a tolerance value of $\pm\epsilon_{force}$. This leads to the following formulation, similar to (3.8):

$$f_{des} - \epsilon_{force} \leq f_{curr} + \frac{\dot{x}\Delta t}{K} \leq f_{des} + \epsilon_{force} \quad (3.15)$$

Rearranging leads to:

$$\frac{K(f_{des} - \epsilon_{force} - f_{curr})}{\Delta t} \leq \dot{x} \leq \frac{K(f_{des} + \epsilon_{force} - f_{curr})}{\Delta t} \quad (3.16)$$

The constraint coefficient matrix $H_{desired}$ and the corresponding constraint vector $h_{desired}$ are calculated as follows:

$$H_{desired} = \begin{bmatrix} -Ad_{g_{bt}} \cdot I_{6x6} \\ Ad_{g_{bt}} \cdot I_{6x6} \end{bmatrix} \quad (3.17)$$

$$h_{desired} = \begin{bmatrix} \frac{K(\epsilon_{force} + f_{curr} - f_{des})}{\Delta t} \\ \frac{K(\epsilon_{force} - f_{curr} + f_{des})}{\Delta t} \end{bmatrix} \quad (3.18)$$

where, as in (3.10), $Ad_{g_{bt}}$ resolves the velocity values that correspond to the force measured by the load cell into the robot base frame. The result is shown in Figure 3.10. Here, f_{des} is set to 25N. Initially, there is no contact between the probe and the phantom but in less than one second, the robot is able to reach and settle at the desired force.

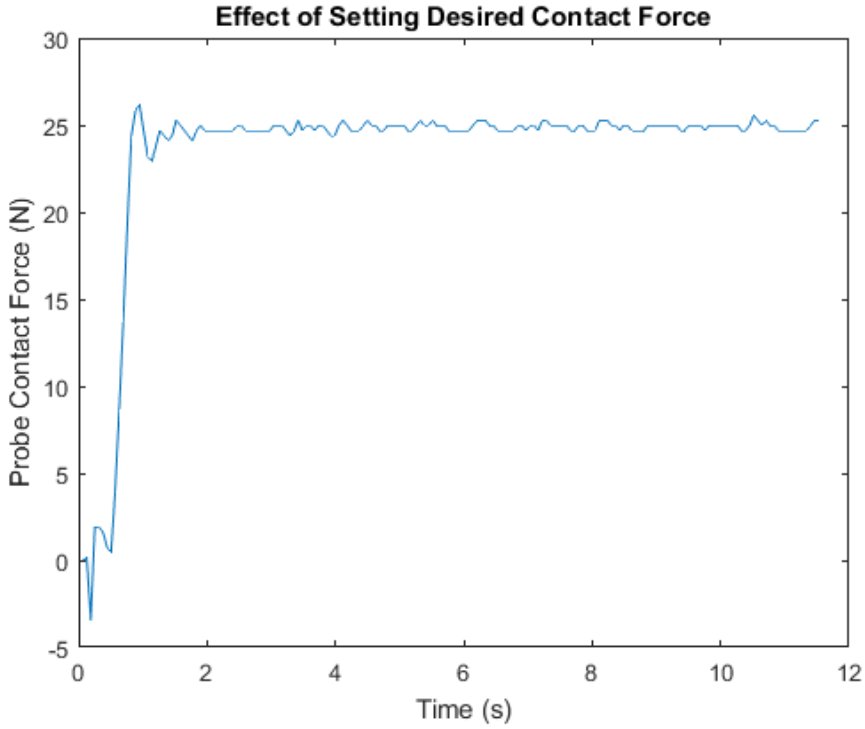

Figure 3.10 Automatic force assistance with 25 N desired contact force set. Robot moves to approach and settle at desired force rapidly and accurately

3.9 Summary

Ultimately, the use of the custom-made dual-sensor probe-holding device described in this chapter provides the capability to isolate the contact forces applied at the probe tip to those applied by the sonographer and used for regular admittance control. This holder thereby permits the sonographer to have full control of the probe with the added benefit of

augmented effort assistance, through the scaled, variable admittance control law of (3.5). In other words, the UR5 is able to perform most of the work, leaving the sonographer to guide the probe into place and to hold it lightly at the desired imaging position. With the activation of contact force locking by quickly applying a twisting motion to the probe holder the strain is even further reduced, since the sonographer can then fully release the probe if desired. Equivalently, activating automatic contact force application will allow the sonographer to exert no force or effort if desired, with the option to readjust or guide the probe to the desired final location. Finally, for safety purposes, contact force limits are always in place and keep the robot from pushing against the patient with potentially harmful or dangerous forces. These capabilities make up the force-assistive components of the presented system. While the effects on force control behavior that result from the contact force limiting, contact force locking, and automatic contact force application features were shown in this chapter, force augmentation using the scaled variable admittance control scheme is explored in further detail in the next chapter.

CHAPTER 4: CO-ROBOTIC ULTRASOUND DEPLOYMENT AND USER STUDIES

In order to validate our dual-sensor force assistance robot ultrasound system, we conducted a set of user studies designed to compare its performance with that of typical, unassisted freehand ultrasound. Our protocol was approved by the Johns Hopkins University Institutional Review Board (IRB) and filed under application ID HIRB00003738 and its amendment AM00004083. Participants of various experience levels using ultrasound systems were recruited and asked to perform certain tasks using our custom probe holder first un-attached and then attached to the UR5's end effector.

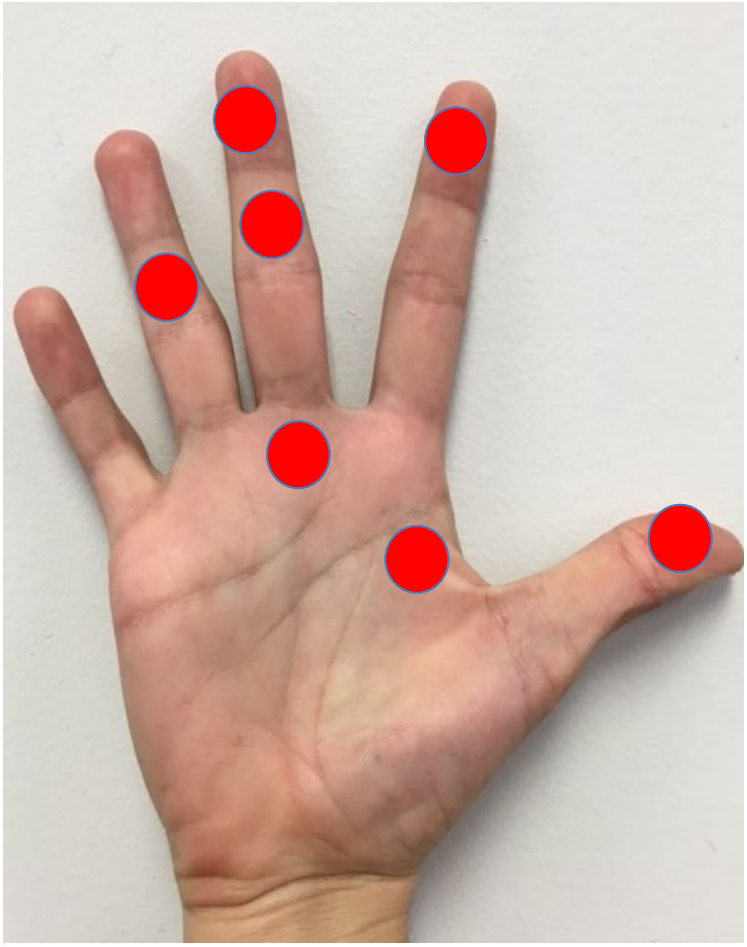

Figure 4.1 Ideal grip force measurement locations, as determined in [48] and resulting placement of Flexiforce film sensors.

4.1 Setup and Methods

Throughout the duration of the study, the participants held the probe holder at an instructed position on the handle extension such that the grip forces applied at the areas of their palms depicted in red in Figure 4.1 could be measured and collected. Seven different 190.5 mm long A201 film sensors (FlexiForce, Boston, MA, USA) with a force capacity of 0-445 N were adhered in this particular pattern on the probe handle in order to measure the grip forces exerted at these seven positions on the users' palms throughout the experiment. This was done to determine the effect of robotic force assistance on the strain sonographers exert during lengthy ultrasound procedures. As explained in chapter 1, studies have shown that sonographers apply an average of 3.96 kg (≈39.6 N) of force in gripping the transducer over an entire scanning period and that this force can reach up to 27.6 kg (≈276 N) if the patient is obese [3]. They have also shown that prolonged durations of high grip-force applications cause injury in sonographers [11-16]. The placement of

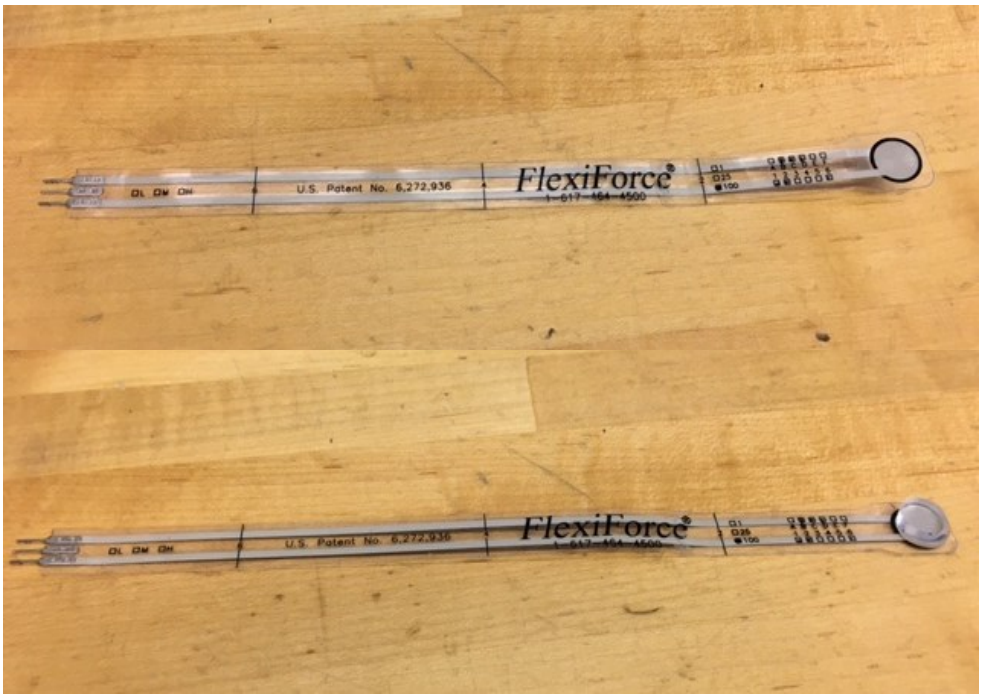

Figure 4.2 Modification of FlexiForce A201 (Top) Sensor without modification. (Bottom) Sensor with force-distributing "puck" adhered to sensing area

these film sensors on the users' hands, seen in Figure 4.1, was determined from the results of Tornifoglio, who performed an analysis on the ideal placement of identical film sensors for the measurement of human grip force [48].

As recommended by the manufacturer, each film sensor was modified with a small laser-cut acrylic "puck" adhered to its sensing area to ensure that it captures 100% of the applied load. One of these film sensors, before and after modification, is shown in Figure 4.2.

Figure 4.3 shows the results of adhering seven of these film sensors onto the probe holder handle according to the desired palmar placement depicted by Figure 4.1. The possible variations in users' hand sizes were taken into account during the placement of

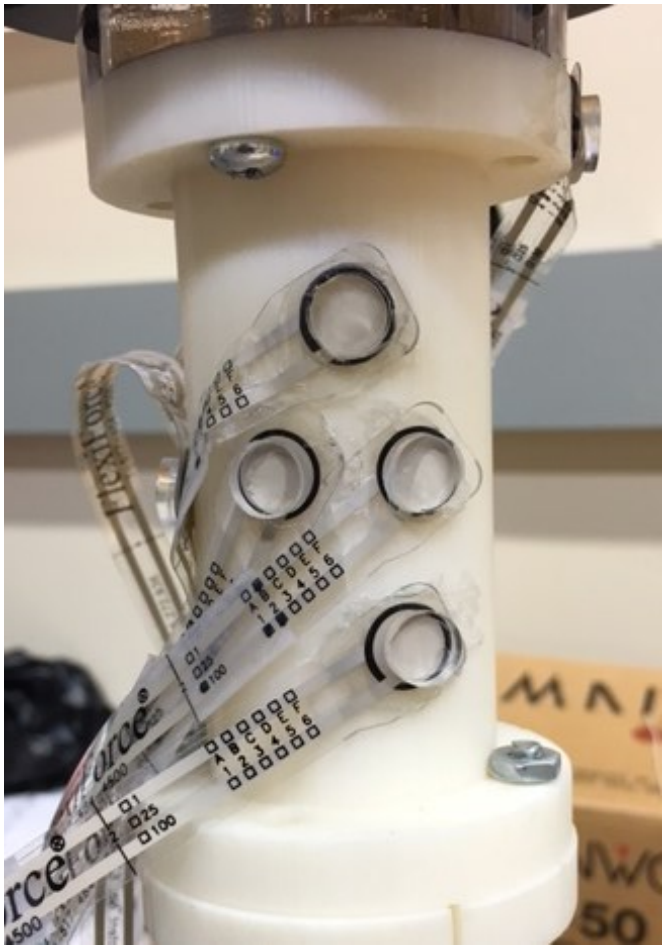

Figure 4.3 FlexiForce sensors attached to the probe holder for grip force measurements throughout experiment.

these sensors. They were adhered in a manner that will satisfy the average adult human hand, allowing for some variance in the data collection. Throughout the duration of the user studies, participants are asked to hold the probe in such a way that their hands are in constant contact with the pucks on each FlexiForce sensor.

In order to collect data from the FlexiForce sensors, voltage readings must be converted into corresponding force values. The signal collection circuit for each of the seven film sensors is shown in Figure 4.4, provided by the sensor manufacturer [49].

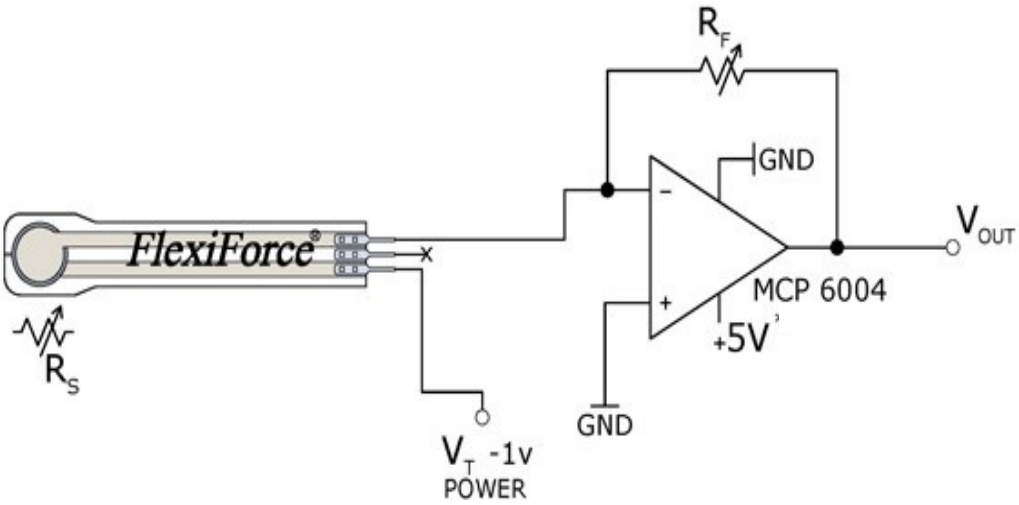

Figure 4.4 FlexiForce recommended circuit from [49].

The circuit is that of an inverting operational amplifier with the following equation:

$$V_{out} = -V_T \left(\frac{R_F}{R_s}\right) \quad (4.1)$$

where V_T is the input voltage, R_F is the reference resistance, set to 100 kΩ, R_S is the variable resistance of the FlexiForce sensor, which decreases as the force applied increases, V_T is the input voltage, set to a constant 1V and V_{out} is the resulting output.

The output of this circuit is passed into a second order Butterworth low pass filter with a cutoff frequency of approximately 20 Hz and a unary gain, designed as described in [50] and shown in Figure 4.5. In the image, V_{in} is the output of the circuit for each film

sensor shown in Figure 4.4 and V_{out} is the resulting filtered voltage reading input into Matlab's (MathWorks, Natick, MA, USA) Data Acquisition (DAQ) Toolbox using a NI USB-6008 DAQ Device (National Instruments, Austin, TX, USA).

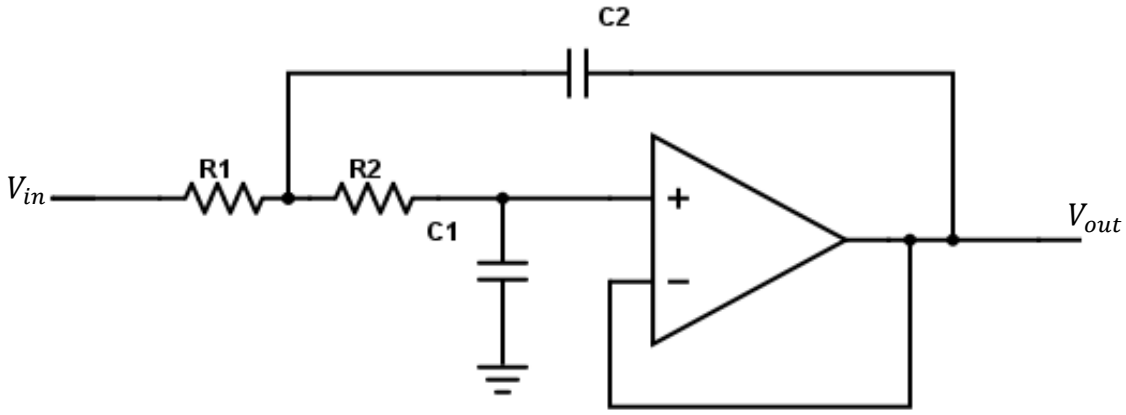

Figure 4.5 Second-order unit-gain low-pass filter designed as in [50]. Schematic made using the Digi-Key Scheme-it tool.

The values of C_1 and C_2 are calculated based on the desired filter type:

$$C_2 \geq C_1 \cdot \frac{4b_1}{{a_1}^2} \quad (4.2)$$

where for a Butterworth filter, $a_1$and b_1 are 1.4142 and 1, respectively [49]. The selected values of C_1 and C_2 were 2.2 µF and 4.7 µF, respectively. The values of R_1 and R_2 are calculated based on the values of a_1, b_1, C_1, C_2, and f_c, the cutoff frequency in Hz (selected to be 20 Hz):

$$R_{1,2} = \frac{a_1 \cdot C_2 \mp \sqrt{a_1^2 \cdot C_2^2 - 4 \cdot b_1 \cdot C_1 \cdot C_2}}{4 \cdot \pi \cdot f_c \cdot C_1 \cdot C_2} \quad (4.3)$$

The resulting values of R_1 and R_2 are 1.9116 kΩ and 3.2038 kΩ, respectively. The transfer function $A(s)$ of the filter in the frequency domain is:

$$A(s) = \frac{V_{out}(s)}{V_{in}(s)} = \frac{A_0}{1+\omega_c(C_1(R_1+R_2)+(1-A_0)R_1C_2)s+\omega_c^2 R_1 R_2 C_1 C_2 s^2} \quad (4.4)$$

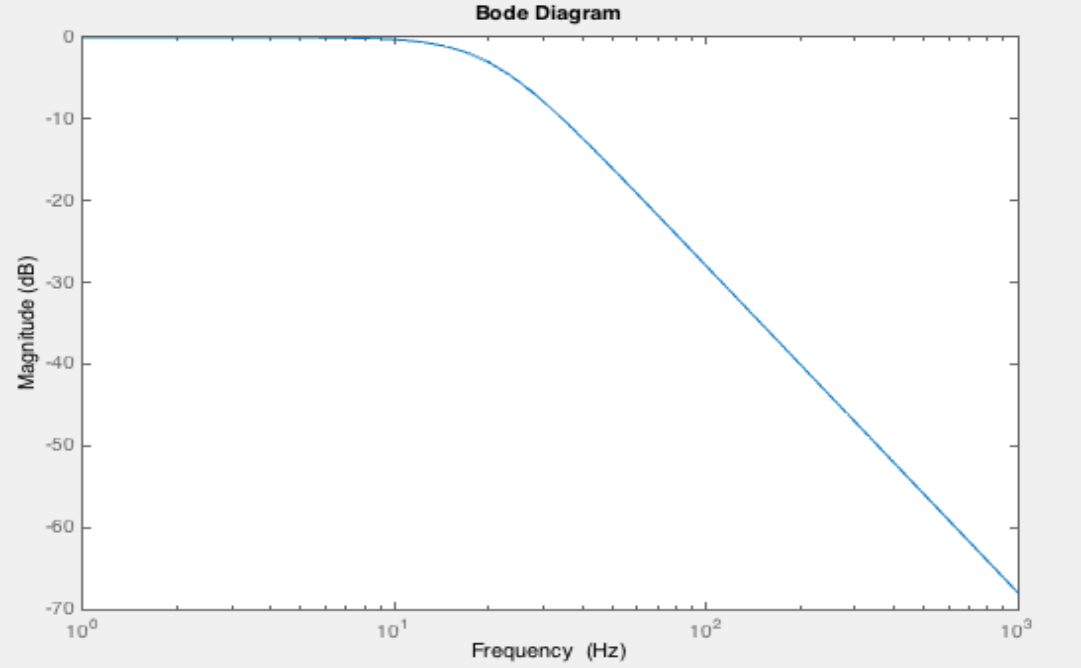

Figure 4.6 Frequency Response of Butterworth Low-Pass Filter with Cutoff Frequency of 20 Hz

where A_0 is the gain, 1, ω_c is the angular cutoff frequency, defined as $\omega_c = 2 \cdot \pi \cdot f_c$ and $s = j\omega$. The filter's expected frequency response is shown in Figure 4.6.

Throughout the procedure, study participants used the ultrasound phantom shown in Figure 4.7. This phantom was created using Plastisol (PVC) (M-F Manufacturing

Figure 4.7 Plastisol Phantom Created for User Studies Experiment

Company, Fort Worth, TX, USA), hardened to withstand high compression forces. High contrast ultrasound imaging features were created by adding Sigmacell Cellulose Type 50 (3% w/v), (Sigma-Aldrich Corporation, St. Louis, MO, USA) to the mixture.

Participants were presented with the graphical user interface (GUI) shown in Figure 4.8. This GUI allows a user to establish or end a connection with the ultrasound machine; select the type of images to be collected; begin and end image collection; establish or end a connection with the UR5; zero the load cell measurement; toggle between "Force Assist" (dual-sensor scaled admittance control) or "Explore" (single-sensor, unconstrained admittance control) modes; visualize the US images and the probe contact force in real time; and save relevant data. There is also a timer used in our experiments to inform each participant for how long to hold the probe steady, as described below. It is important to

Figure 4.8 Graphical User Interface (GUI) used for data collection in user study

note that the back-end program for image acquisition in a Matlab GUI used was originally written by Lei Chen of the MUSiiC group and modified for our needs.

Throughout the experiment, we record the contact force applied by the probe against the US phantom as well as the grip force of each participant, while collecting ultrasound images. We do this for all trials, those where the ultrasound probe is manipulated through freehand and those where the UR5 provides force assistance. The contact forces are used to compare the need of readjustment as well as the presence of hand tremor and other destabilizing factors present when imaging using the two methods. The target forces used are 5, 15, 25, 35, and 45 N. While most ultrasound procedures are unlikely to require more than 25 N, these higher forces in the short time-span of each study allow us to model the effect of time on sonographer fatigue and the effect of the resulting hand tremor. We analyze grip forces to determine the effect of robotic assistance in reducing user strain. Lastly, we provide the study participants with a questionnaire to collect their opinions on the ease of use, intuitiveness, and physical strain involved with both freehand and robotic ultrasound. The questionnaire presented to the users of this study is shown in Appendix 5.

The experimental protocol is summarized below:

1. With the probe holder unattached to the robot end effector, the participant grasps the probe holder at the handle such that the film force sensors match up with the positions on their palms shown in Figure 4.1. Any required assistance on how to do so accurately is provided.
2. Participant places probe on phantom and applies a force of 5 N, watching the gauge visible on the GUI to maintain force as stable and consistent as possible

3. Participant notifies investigator that he or she is holding the probe as steadily as possible. Investigator activates 10-second timer on GUI.
4. Participant continues to maintain this position as constant as possible until the ten seconds have passed. Grip force, contact force, and image information is collected throughout these ten seconds.
5. Participant is given some time to rest, if necessary.
6. Steps 2-5 are repeated for probe contact forces of 15, 25, 35, and 45 N.
7. Steps 1-6 are repeated two additional times, for a total of 3 trials of five force measurements each.
8. Steps 1-7 are repeated with the probe holder attached to the robot end effector and with robotic force assistance provided.
9. Participant completes questionnaire, sharing opinions about system.

4.2 Results and Discussion

So far, six participants with varying degrees of ultrasound experience have been recruited to complete the experiment described in detail above. As mentioned, throughout the experiments, the participants were asked to hold an ultrasound probe against a custom-made phantom while images, grip force and probe-to-phantom contact forces were recorded. From these preliminary results, we compared the values of the force metrics collected in non-robotic trials, in which the participant manipulated the probe freehand, with those collected with assistance from our robotic control framework. Due to variations in each individual's physical strength, experience with robot manipulation and other pertinent factors, each study participant's results were analyzed independently.

4.2.1 Grip Force Measurements

When analyzing each user's grip force throughout the imaging procedure, the output of all seven FlexiForce film sensors were summed in order to create one single grip force indicator. This was done for each trial and each contact force goal (5, 15, 25, 35, or 45 N). For each person, the resulting grip force indicator for each contact force target value was averaged separately across the three freehand trials and the three robotically assisted trials. Figure 4.9 shows the results for each individual with the solid blue lines displaying the grip force as measured without robotic assistance and the dotted red line displaying that measured with robotic assistance. As seen, the results show an overall trend of a significant reduction in grip force between non-assisted and assisted trials. The greatest drop in grip force, 9.29 N (72.8% decrease), was seen for participant 5 when imaging in the 45 N force goal. Participant 3's results followed the expected trend for target contact forces of 5-35 N but showed a deterioration for the 45 N data point, with an increase of 1.16 N (24.17%) between non-assisted and assisted trials. While any number of factors might have caused this discrepancy, it is also important to note the standard deviation of the average grip-force indicator for the robot-assisted trials. At a value of 3.99 N, it is the highest standard deviation in the FlexiForce measurements across all robot-assisted trials, implying that the participant did not appropriately grip the probe during the full span of the data collection.

The nearly consistent results across all trials shows the feasibility of robot force assistance in reducing the grip force required by ultrasonographers, and therefore their chance of developing musculoskeletal disorders. Future work will focus on ensuring grip measurements are appropriately collected for participants of various hand sizes and of either hand dominance (left or right handed).

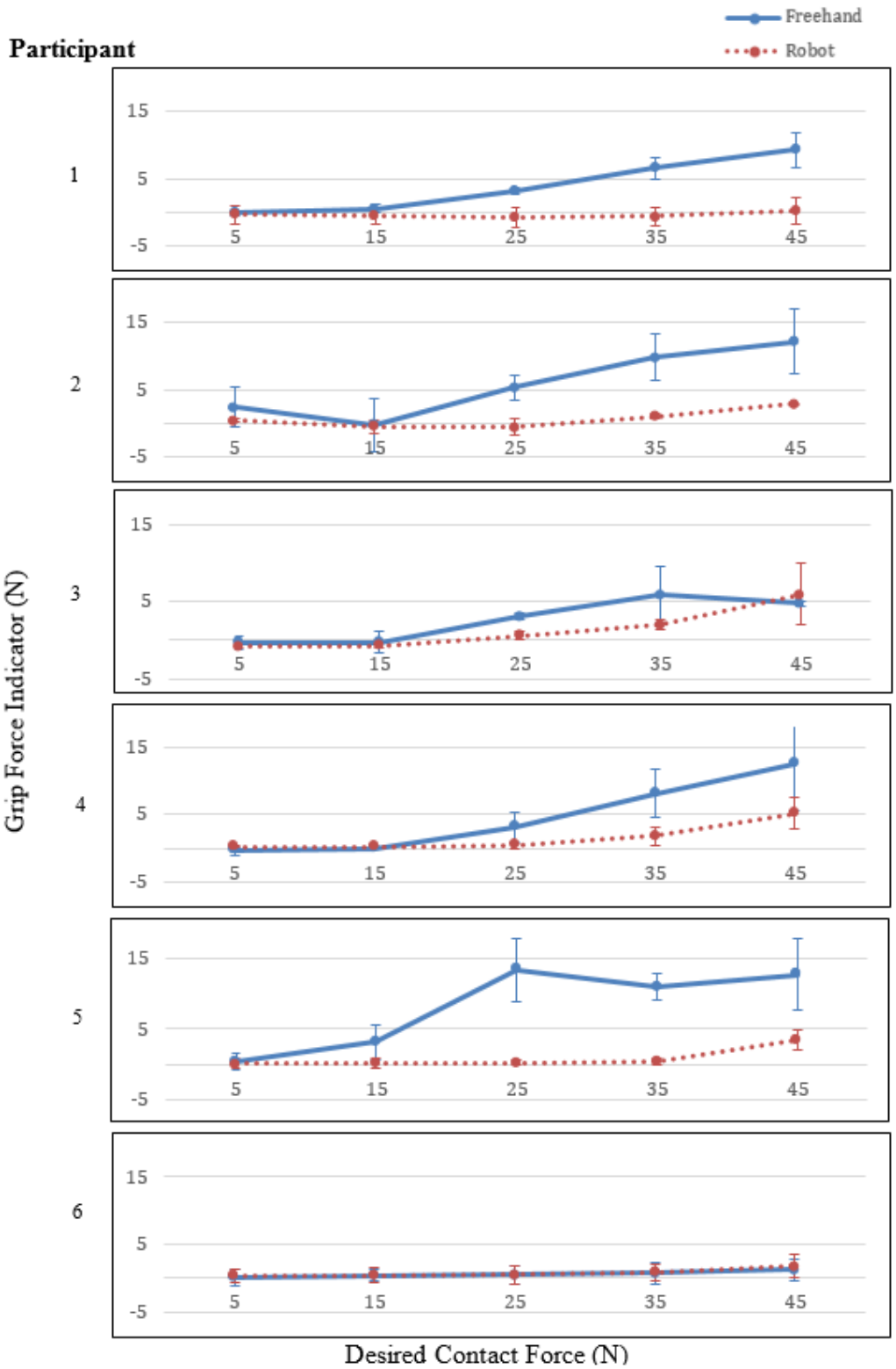

Figure 4.9 Grip Force Indicator (sum of all FlexiForce sensor readings) for each participant

4.2.2 Contact Force Measurements

The contact forces measured by the Honeywell Model 31 Mid load cell were also analyzed to determine the amount of variation in the measurement when attempting to maintain a constant force against the custom-made phantom. An example of the data collected for one participant (5) is presented in Figure 4.10. The data shown by the blue curve is the contact force over time the participant applied against the phantom without assistance for a single trial while the orange curve shows the effect of assistance, also for a single trial. The regions of interest are constrained to 10 second intervals during which the study participant holds the probe at 5, 15, 25, 35, or 45 N.

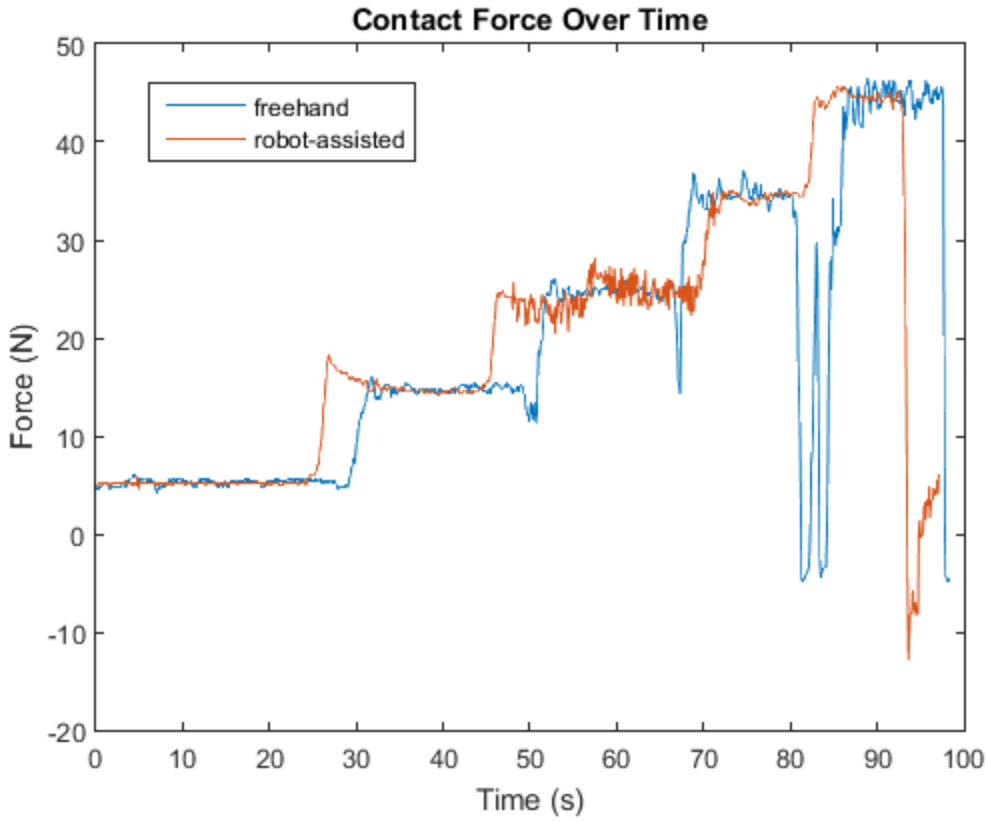

Figure 4.10 Contact force vs time with and without robot force assistance

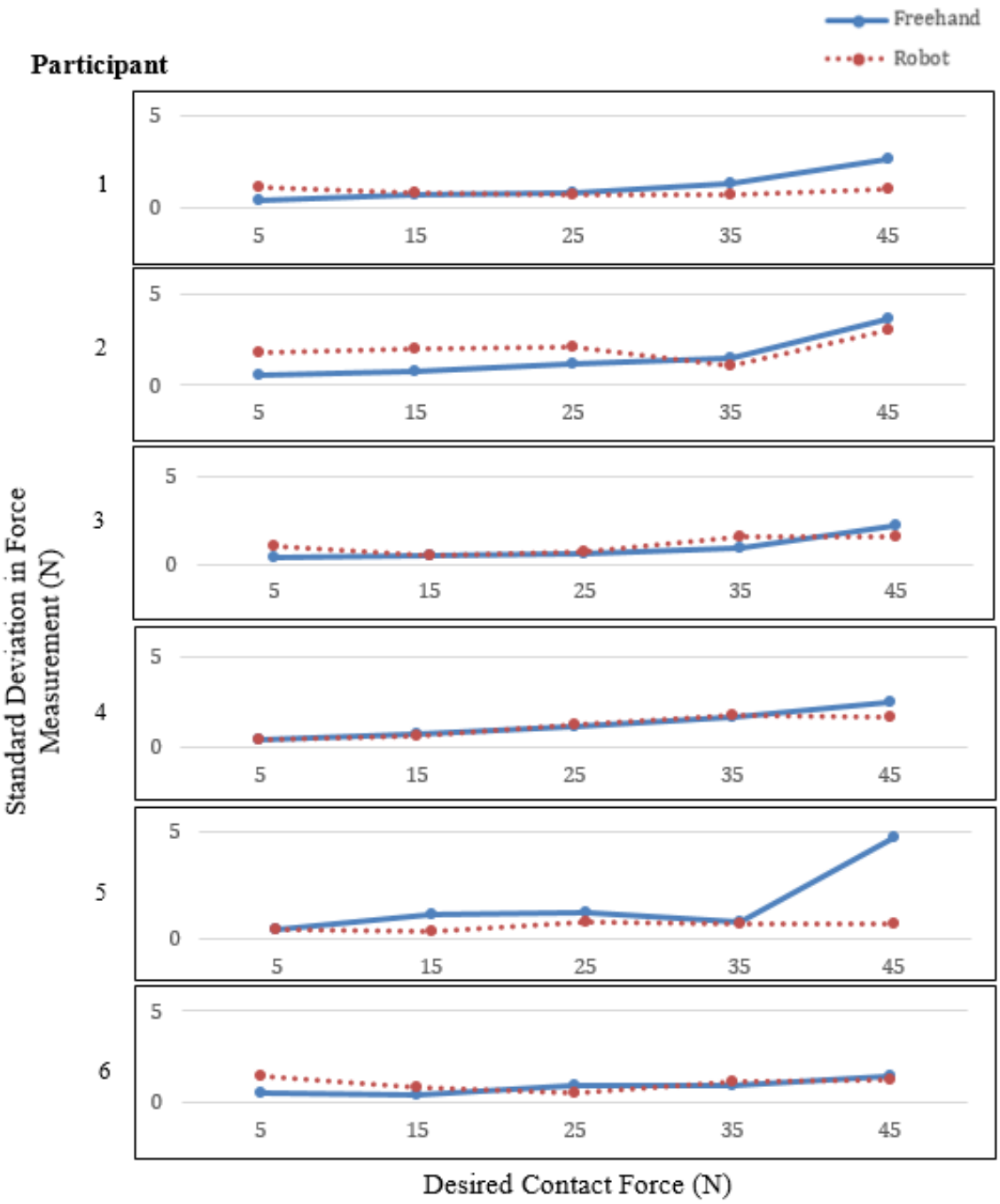

Figure 4.11 Error between expected and measured contact force readings over ten second measurements

Figure 4.11 shows the standard deviation in the contact force measured throughout the procedures; the solid blue line represents the data collected during freehand ultrasound and the dotted red line represents that collected with robotic assistance. While results vary among participants, all six showed a reduction in the standard deviation for the 45 N goal

force using robotic assistance, with reductions in standard deviations ranging from 0.128 N (9.13% decrease; participant 4) to 4.08294 N (86.09% decrease; participant 5). The average reduction at this data point was 1.318 N (average percent reduction of 39.37%). For lower goal force values, the results were mixed. In the majority of cases, the data collected with robotic assistance had a standard deviation below or very nearly equal to that collected with freehand. However, a surprising trend was the slight but clear increase in variation at the 5 N and 10 N data points, shown in the results of four of the six participants (participants 1, 2, 3, and 6).

The reduction in error in the 45 N data point across participants shows the feasibility of using force assistance in ultrasound. While it is not common for ultrasound procedures to require forces as high as 45 N, the effect of fatigue over prolonged procedures can have a similar outcome in the hand tremor of an ultrasonographer. Therefore, it is likely that the reduction in force deviation over time in this short, high-force case points at a similar reduction in deviation in prolonged, mid-force cases typical in clinical practice. The unexpected behavior in the lower force goals, which results in more error with robotic assistance than without is likely due to the improper tuning of the anisotropic admittance gains defined in (3.6) and (3.7), which might be allowing for involuntary user motions or even noise to affect the robot commands. Currently, these gains are most sensitive at low contact forces, explaining the apparent improvement in behavior as force increases. Before future trials are run, more testing will be conducted in order to find the ideal values for these gain matrices. It is also important to note the presence of noise added by vibrations in the robot. At certain unpredictable points, the UR5 begins to shake in place, even when no new velocity commands are provided. An example of this behavior is seen in Figure

4.10 above, where the significant variation shown in the 25 N measurement using the robot was caused by this phenomenon. Future work will aim at filtering out these high frequency vibrations.

4.2.3 Questionnaire Results

At the end of the study, each participant was asked to fill out a questionnaire, the contents of which are shown in Appendix 5. The goal of this questionnaire was to collect user opinions on the usability of, the intuitiveness of and extent to which our robotic force assistance system helped to reduce user strain. Study participants were asked to answer

Response	Difficulty of Using Freehand in Imaging Task	Difficulty of Using Robotic System in Imaging Task	Strenuousness of Imaging Task with Freehand	Strenuousness of Imaging Task with Robotic System	Intuitiveness of Robotic System Compared to Freehand
1	0	0	0	0	1
2	0	2	0	0	0
3	1	4	1	6	5
4	5	0	3	0	0
5	0	0	2	0	0

Table 4.1 Participant Responses to User Study Questionnaire

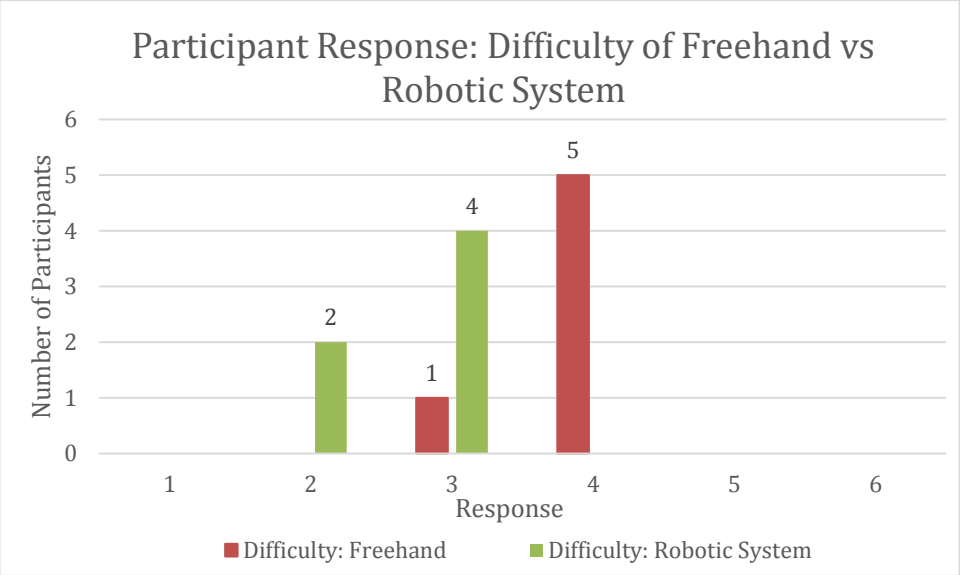

Figure 4.12 Participant response regarding difficulty of freehand and robot-assisted US. The change was significant ($p = 0.0127$; $p < 0.05$).

each question on a scale of 1-5. The results of the survey for the six participants are shown in Table 4.1. Figure 4.12 depicts the responses for the questions regarding difficulty, Figure 4.13 does the same for strenuousness, and Figure 4.14 shows the responses to the question involving the intuitiveness of the robotic system compared to freehand.

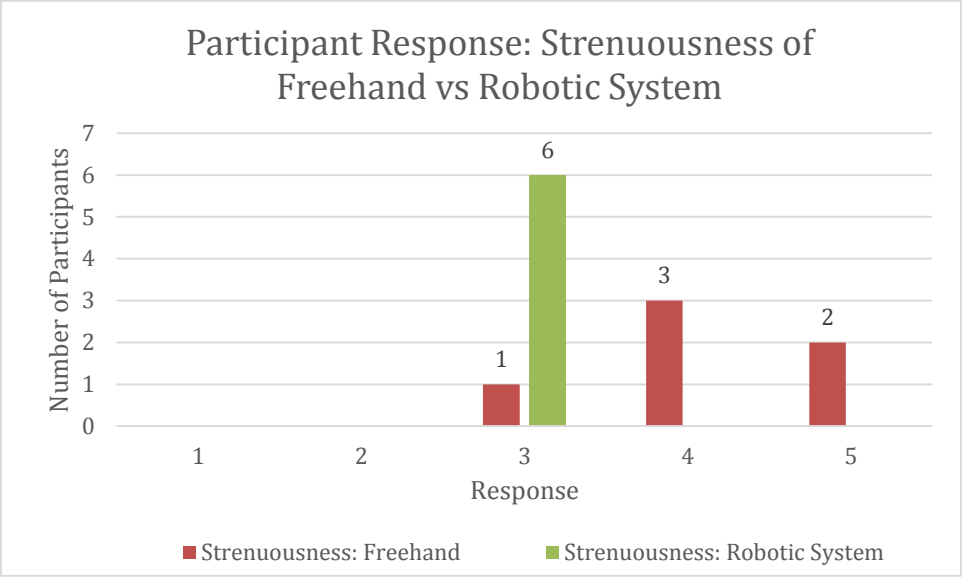

Figure 4.13 Participant response regarding strenuousness of freehand and robot-assisted US. The change was significant ($p = 0.0117$; $p < 0.05$).

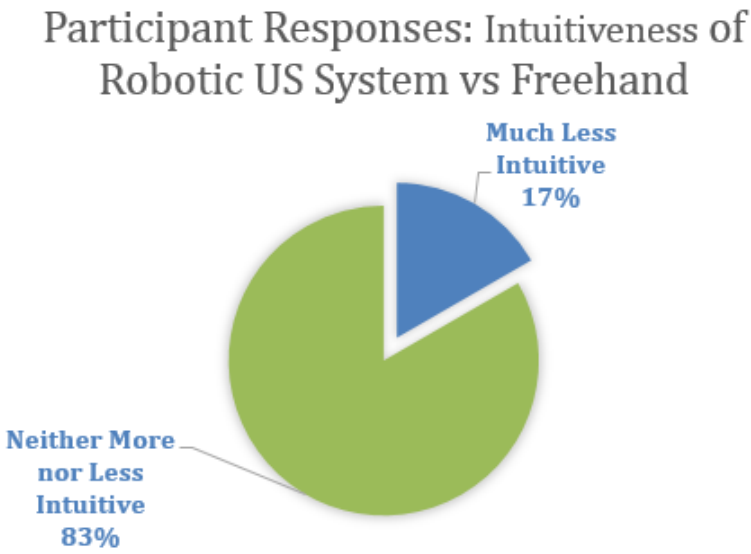

Figure 4.14 Participant response regarding intuitiveness of the robotic US system, as compared to freehand US

The results showed a relatively positive response to our robotic ultrasound imaging system, showing that for the most part easier to use and less strenuous than freehand ultrasound. 83.33% of respondents (5) said that the imaging task without any robotic assistance was “somewhat difficult”, while 16.66% of respondents (1) deemed it “neither easy nor difficult.” 66.66% (4) believed that completing the imaging task with the robotic system was “neither easy nor difficult” while 33.33% (2) ranked it as “somewhat easy.” This difference in responses was found to be statistically significant ($p = 0.0127$; $p < 0.05$). From this preliminary data it can be concluded that in general, the robotic system can be considered to be at least equally as easy to use, if not easier than freehand. In terms of strenuousness, 33.33% of respondents (2) believed using freehand to complete the experiment tasks was “extremely strenuous”, 50% (3) believed it to be “very strenuous” and 16.66% (1) considered it “moderately strenuous.” 100% of participants (6) said that the robotic ultrasound system was “moderately strenuous”, proving it can match, if not decrease the amount of strain placed on the sonographer. This was also found to be a significant change ($p = 0.0117$; $p < 0.05$). Lastly, 83.33% of participants (5) deemed the robotic ultrasound system “neither more nor less intuitive” than freehand while 16.66% (1) considered it to be “much less intuitive.” In this case, this result shows some of the limitations of robotic ultrasound. Given the bulkiness of industrial robots and the constrained workspace, the probe cannot be maneuvered as easily as in freehand. It was also throughout the trials that the simultaneous collection of images for analysis added notable time latency (lag) to the robot’s movements, making it considerably more difficult to control. Future work will focus on balancing the number of US images saved and the lag of the robot.

4.2.4 User Study Conclusions

Overall, these preliminary results show the potential of our dual-sensor force-assistance robotic ultrasound system in reducing sonographer strain and hand tremor during image collection. The scaled admittance control scheme has not previously been investigated in robotic ultrasound procedures and has the potential of changing the paradigm of traditional ultrasonography. In the future, work will be done to improve the usability of our system. Following that, participants will be recruited to test these improvements. Additionally, analysis of all ultrasound images collected during the trials will be performed to determine the effect of the robot's hand tremor reducing capabilities in improving the stability of consecutively collected ultrasound images.

CHAPTER 5: VIRTUAL FIXTURES AND SYNTHETIC TRACKED APERTURE ULTRASOUND

The work included in this section was completed to fulfill the requirements of the Advanced Computer Integrated Surgery Course at the Johns Hopkins University, taught by Dr. Russell Taylor. It was done in collaboration with Kalyna Apkarian under the mentorship of Haichong 'Kai' Zhang, Dr. Emad Boctor, and Dr. Russell Taylor. Due to the similarities with the work described in previous chapters and the overlap in the requirements, some components were used in this work as well. For example, the admittance control law and signal filtering techniques described in Chapter 2, as well as the force limiting and manual constant desired force setting functionalities from Chapter 3 were incorporated into the virtual fixtures work described in the remainder of this chapter. All were developed by the author. Much of the imaging algorithms used were developed by one of our mentors, Haichong Kai Zhang. The remaining work, namely the virtual fixtures formulation and implementation, and analysis of images acquired applying these algorithms was done collaboratively with Kalyna Apkarian.

5.1 Introduction to Synthetic Tracked Aperture Ultrasound Imaging

As explained by Zhang et al. [51], ultrasound image resolution is affected by several factors, including the center frequency of the transmission wave and the F-number, which represents the ratio of the focusing depth to the aperture size. Typically, high center frequency is desired for high-resolution. However, only low-frequency acoustic waves are available if the region of interest is located in deep tissue, since high-frequency waves are absorbed in the near field. Similarly, the F-number increases with increasing focusing

depth, but leads to degradation in image quality in deep tissue. Therefore, a large probe aperture size is desired to decrease the F-number. Synthetic aperture (SA) is a technique presented in the literature [52-54] that increases image resolution by synthesizing the information from multiple sub-apertures and extending the effective aperture size.

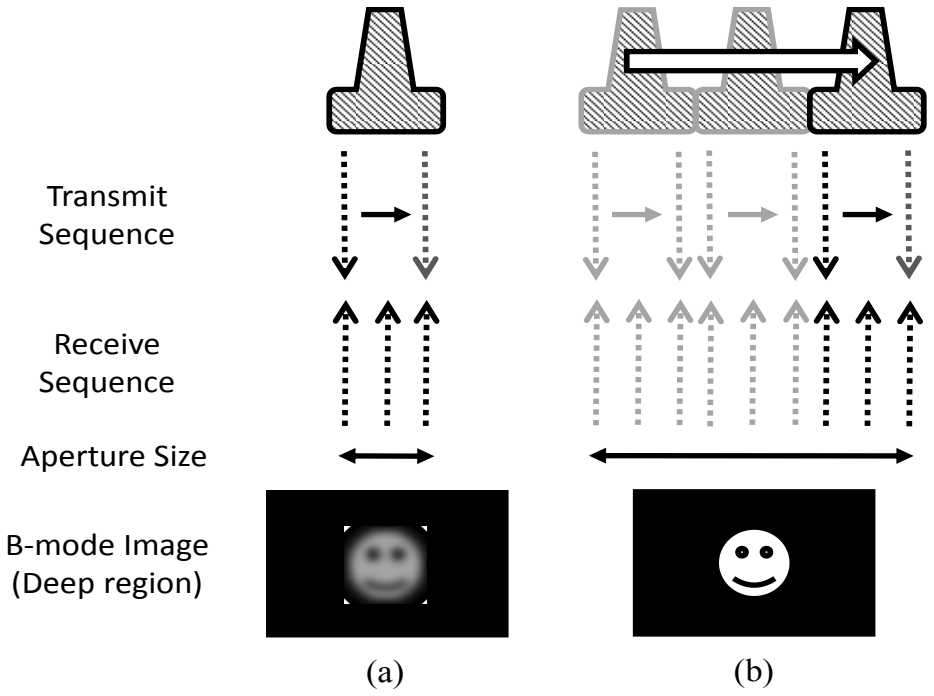

Figure 5.1 How synthetic tracked aperture ultrasound (STrAtUS) imaging is different from conventional synthetic aperture imaging. (a) Synthetic aperture imaging with a single pose, and (b) STrAtUS imaging with multiple poses and resulting resolution impr

Zhang et al. [51] propose the use of a 6-DOF robotic arm to further expand the synthetic aperture size beyond that of conventional SA. The algorithm, Sysnthetic Tracked Aperture Ultrasound (STRATUS), utilizes the tracking capabilities of the UR5 robot to identify the orientation and position of the ultrasound image and merges multiple sub-apertures from these different poses to beamform one final compound image. A depiction of the process is shown in Figure 5.1. In their work, the UR5 is given a predetermined trajectory in 3D space through which to move the US probe. Regular B-mode ultrasound images are simultaneously collected. Recording the robot's forward kinematics throughout

the process allows the probe's position and orientation to be matched with its corresponding ultrasound image. In the final step, data collected at each pose is projected back into the original ultrasound image frame and summed up, resulting in a reconstructed image. In order for this projection to take place, all data collected must be transformed to a uniform coordinate system. The coordinate systems involved in STRATUS imaging are shown in Figure 5.2. The transformation from the robot base frame to the robot end effector

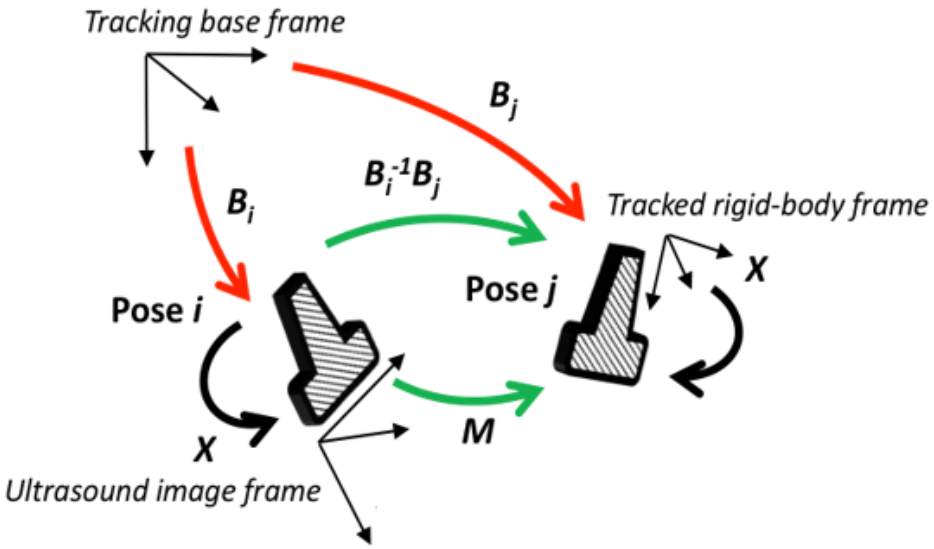

Figure 5.2 The coordinate systems involved in synthetic tracked ultrasound (STRATUS) imaging [51]. Reprinted with permission from SPIE ©2016 SPIE

frame is defined as B, and the transformation from robot end effector frame to the ultrasound image frame is defined as X. As in [51], the motion applied to the ultrasound probe by the robot as it is autonomously guided along the predetermined trajectory can be expressed as:

$$M = X^{-1}B_i^{-1}B_jX \quad (5.1)$$

where B_i and B_j correspond to two subsequent poses of the robot end effector and M is the resulting transformation between the two. The transformation of the data from each pose to a uniform coordinate system can be expressed as in [55] as

$$p_u = X^{-1}B_u^{-1}B_ip_i \quad (5.2)$$

where p_i is the location vector of the pose i and p_u is the projected location vector in the uniform coordinate system, B_u is the transformation for the uniform coordinate system, and B_i is the i-th pose, as in (5.1). From [55], the received pre-envelope detected radio frequency (RF; raw ultrasound data generated from ultrasound probes and from which B-mode images are reconstructed) signals from each pose are then summed up as

$$RF_u(p_u) = \sum_{i=1}^{N} RF_i(p_u) \quad (5.3)$$

where RF_i is the received RF signals from the i-th pose, and RF_u is the RF signal of the final reconstructed image. Zhang et al. [55] demonstrated that this technique reduces speckle patter as the aperture size extends, as seen in Figure 6.3. As shown, increasing numbers of pose data help to increase the the resolution of the image.

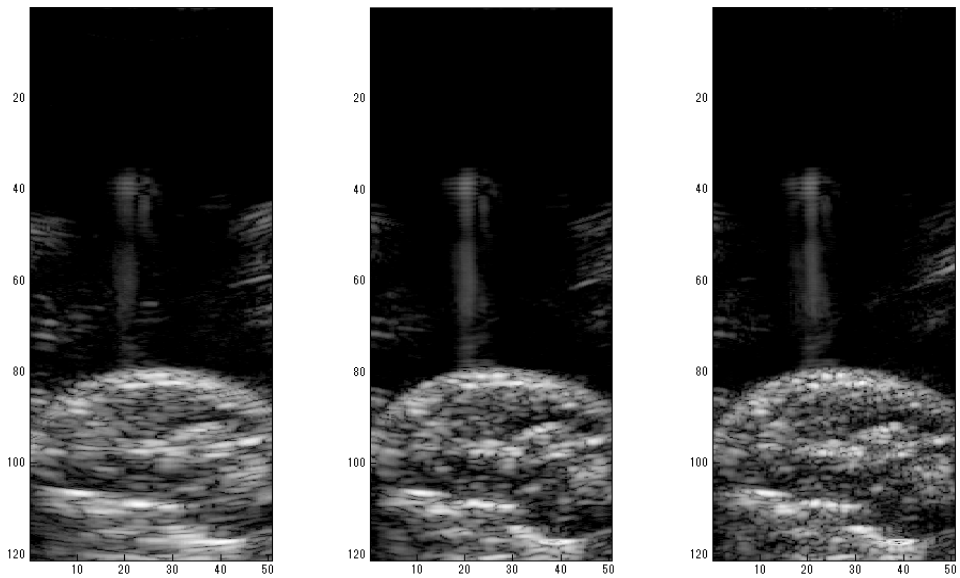

Figure 5.3 The reconstructed image of the human wrist. (a) Single pose result represents conventional ultrasound image, (b) the STrAtUS imaging result using 10 poses data corresponding to 19.5 mm motion, and (c) the STrAtUS imaging result using 20 poses

While the results previously collected demonstrate the feasibility of using STRATUS imaging in clinical applications, the fact that the UR5 robot acted autonomously

causes safety to become a concern. Additionally, automatic robot motion makes it difficult to change the speed or direction of imaging dynamically throughout the procedure, since the predetermined path cannot be changed. Therefore, an improved method is a cooperative control scheme that allows the sonographer to have decision-making abilities in the imaging procedure.

5.2 Introduction to Virtual Fixtures

As previously described, virtual fixtures (VF) are a class of robot control algorithms that consist of geometric constraints that either limit the motion of the end effector or that require certain behaviors. VFs can be used to augment clinicians' abilities to provide safety and precision [56]. Various versions of virtual fixtures have been presented in the literature [57-61], with the work introduced by Funda et al. [42] and extended by Li et al. [43-45] providing a flexible framework for their implementation. It uses the optimal motion control method described in (2.11) to define geometric constraints such as restricted geometric workspace. In the case of robotic ultrasound assistance, the use of this approach helps lead the sonographer along a desired trajectory while providing haptic feedback to discourage deviation from this path. For the purpose of synthetic tracked aperture ultrasonography, the use of VFs can comfortably lead the sonographer along an in-plane trajectory, guiding him or her to scan the correct area and nowhere else, so that a final, higher-resolution image can be reconstructed. This method gives the sonographer control of the probe as it only moves when force is applied on it, using the admittance control law defined in (2.1), and allows for the drawing of patient-specific trajectories in real time. Additionally, force control can be used to maintain a constant contact force with the patient during the imaging

process, as defined in (3.17) and (3.18) and to limit this value for patient safety, as formulated in (3.10) and (3.11).

The geometric virtual fixtures used in this work, namely stay on line and stay on plane, are described in greater detail in sections 5.3 and 5.4 below.

5.3 Stay on Line Constraint

The first geometrical constraint implemented for STRATUS was a stay on line virtual fixture, used to assist the ultrasonographer on staying on the same imaging plane, required for the accurate image reconstruction in synthetic aperture imaging. The formulation of this constraint is explained in detail in [43]. In short, we aim to define a line in 3-dimensional space along which the probe is to stay for the duration of the imaging procedure. The error between the probe position and the pre-defined line is minimized

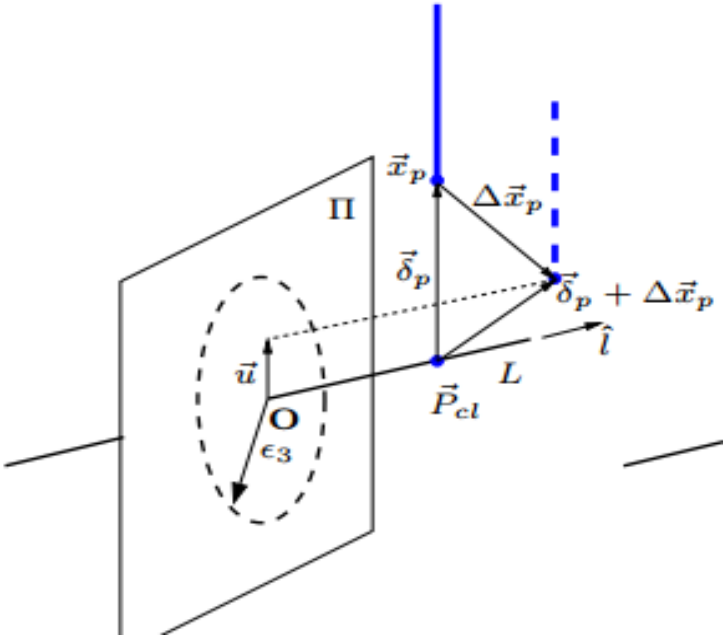

Figure 5.4 Geometry of Stay on Line Constraint [43]. Reprinted with permission from IEEE, ©2005 IEEE.

throughout the process. This general idea is shown in Figure 5.4 below, where L defines the selected line ($L = L_0 + \hat{l}$), L_0 is a point on the line, $\hat{l}$ is the vector which defines its

direction, $\vec{x}_p$is the position of the probe head at a moment in time, $\vec{P}_{cl}$is the point on the line closest to the probe at that moment, $\vec{\delta}_p$is the distance between $\vec{x}_p$ and $\vec{P}_{cl}$, and $\Delta\vec{x}_p$ is the incremental change in the position of the probe head for each step, either approaching or moving down L. $\vec{u}$ is the projection of $\vec{\delta}_p + \Delta\vec{x}_p$ onto the plane Π, perpendicular to L. The magnitude of $\vec{u}$ must be less than an error tolerance value ϵ_{line} (ϵ_3 in Fig 5.4).

In the image, the error-tolerance range is defined by a circle around the line with radius ϵ. However, due to the linear nature of the optimization solver used, the constraint must be linearized, done by representing the circle as a polygon of n vertices. The optimization constraints can now be constructed as:

$$H_{line} = \begin{bmatrix} \left[R\left[\cos\frac{2\pi}{n}, \sin\frac{2\pi}{n}, 0\right]^T\right]^T & 0 & 0 & 0 \\ \left[R\left[\cos\frac{4\pi}{n}, \sin\frac{4\pi}{n}, 0\right]^T\right]^T & 0 & 0 & 0 \\ \cdots & & & \\ \left[R\left[\cos\frac{2n\pi}{n}, \sin\frac{2n\pi}{n}, 0\right]^T\right]^T & 0 & 0 & 0 \end{bmatrix} \quad (5.4)$$

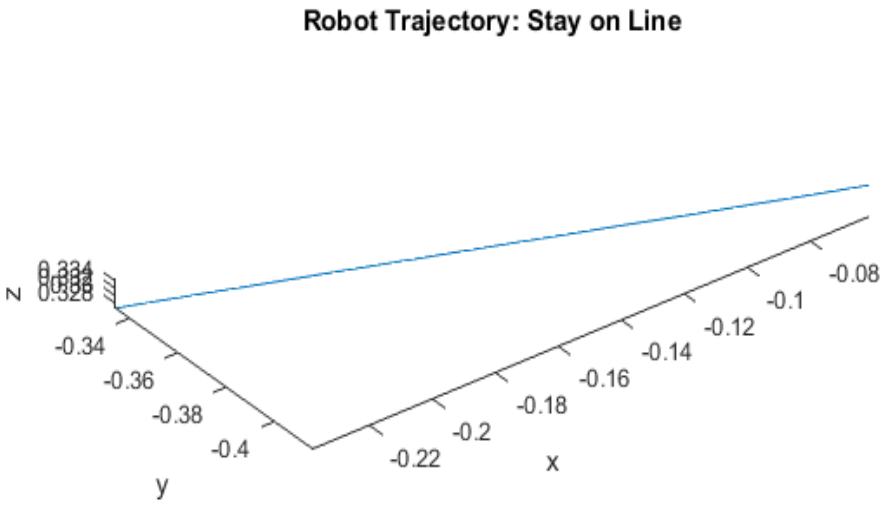

Figure 5.5 Robot tracking data of the US probe with stay on line virtual fixture activated

$$h_{line} = \begin{bmatrix} \epsilon_{line} \\ \cdots \\ \epsilon_{line} \end{bmatrix} - H_{line} \begin{bmatrix} [\vec{x}_p - \vec{P}_{cl}] \\ \vec{0} \end{bmatrix} \quad (5.5)$$

where $R \in SO(3)$ defines the rotation between the plane Π and the robot coordinates. In our implementation, $\epsilon = 0.5\text{mm}$ and $n = 8$. Tracking data of the probe head over the duration of an US imaging procedure is shown in Figure 5.5 and displays how the probe head does indeed stay within 0.5 mm from the line.

5.4 Stay on Plane Constraint

Similar to the Stay on Line algorithm, the stay on plane virtual fixture limits the movement of the robot and therefore the position of the probe in such a way that the images acquired are all in plane with the region of interest. This constraint however gives the sonographer more control over the regions that can be visited by the probe and should prove more useful in clinical practice since it will allow for moving down paths that are

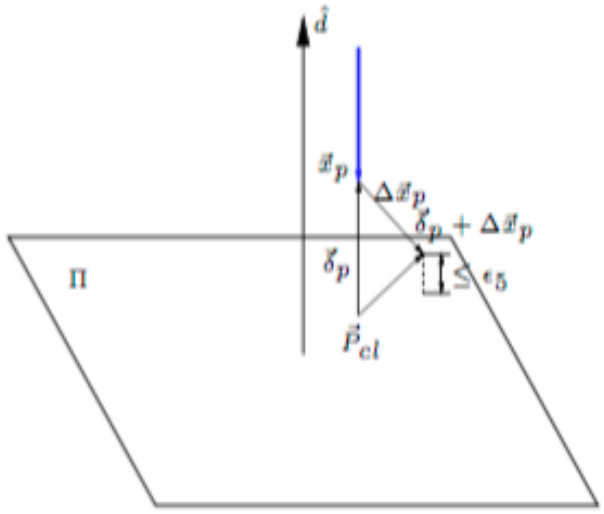

Figure 5.6 Geometry of Stay on Plane Constraint [43]. Reprinted with permission from IEEE, ©2005 IEEE.

not planar, as patients' anatomies are typically not. The geometric setup of this constraint comes from [43] and is shown in Figure 5.6.

Analogous to the linear constraint case, $\vec{P}_{cl}$ is the point on the plane Π closest to the current location of the probe $\vec{x}_p$ and $\vec{\delta}_p$ is the associated error. $\hat{d}$ is the unit normal direction of Π. Here, we define a separate ϵ_{plane} (ϵ_5 in the image), which is the allowable margin of error. The constraint becomes:

$$H_{plane} = \begin{bmatrix} -\hat{d}^T & 0 & 0 & 0 \\ \hat{d}^T & 0 & 0 & 0 \end{bmatrix} \quad (5.6)$$

$$h_{plane} = \begin{bmatrix} 0 \\ \epsilon_{plane} \end{bmatrix} - H_{plane} \begin{bmatrix} [\vec{x}_p - \vec{P}_{cl}] \\ \vec{0} \end{bmatrix} \quad (5.7)$$

Tracking data of the probe head over the duration of an US imaging procedure is shown in Figure 5.7 and shows how this constraint helps maintain the probe on the plane, adding one degree of freedom to the Stay on Line VF.

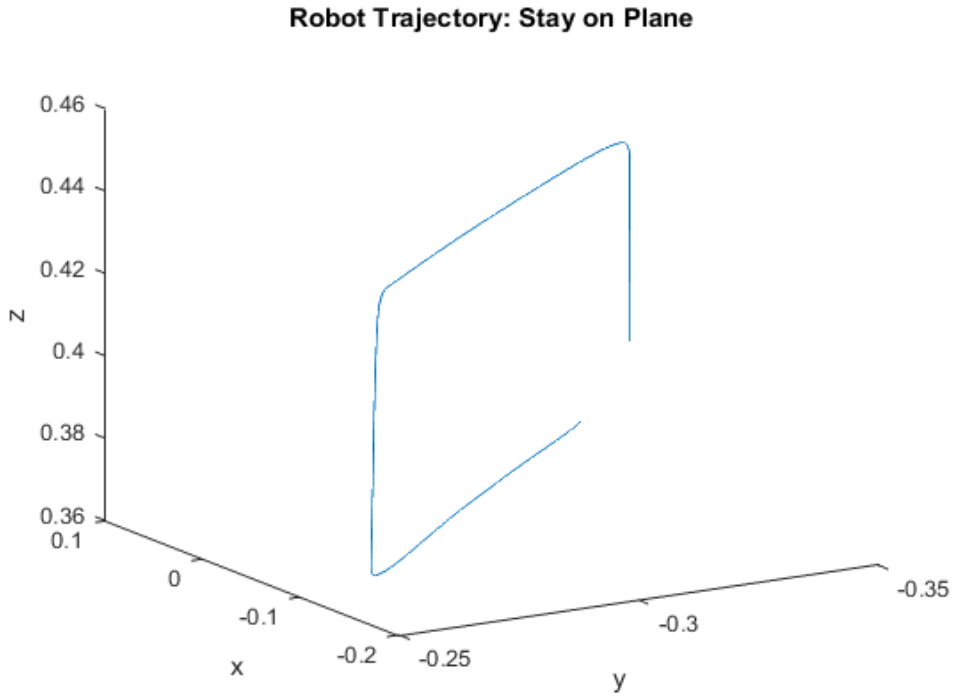

Figure 5.7 Robot tracking data of US probe with the stay on plane virtual fixture activated

It is sometimes desirable to maintain a constant contact force during an in-plane imaging procedure. In this case, it is possible for contact force control to be combined with the stay-on-plane constraint. The optimization problem becomes:

$$\dot{q} = \underset{\dot{q}}{\operatorname{argmin}} \|J\dot{q} - \dot{x}\| \quad (5.8)$$

$$\text{subject to: } \begin{bmatrix} H_{desired} & 0 & 0 \\ 0 & H_{plane} & 0 \\ 0 & 0 & H_{joint} \end{bmatrix} \begin{bmatrix} J(\theta) \\ J(\theta) \\ I_{6x6} \end{bmatrix} \dot{q} \leq \begin{bmatrix} h_{desired} \\ h_{plane} \\ h_{joint} \end{bmatrix} \quad (5.9)$$

where $H_{desired}$ and $h_{desired}$ are as defined in (3.17) and (3.18), respectively, and H_{joint} and h_{joint} are defined in (2.13) and (2.14), respectively.

5.5 User Interface and STRATUS Process Flow

A custom graphical user interface (GUI) was designed to allow the user to activate the desired virtual fixtures. It is shown in Figure 5.8. It gives the sonographer the options to activate the stay on line constraint (by pushing the "Line" button), the stay on

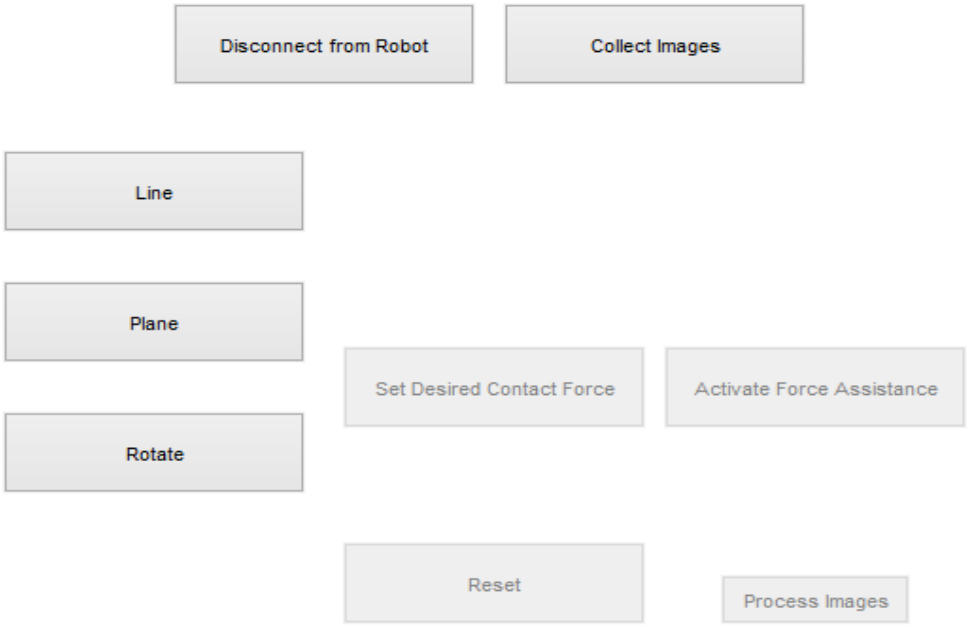

Figure 5.8 GUI Used for STRATUS-VF imaging applications to connect with robot and US machine and activate desired VF or force control constraints.

plane constraint with the orientation of the probe kept constant (no rotation is allowed; by pressing the “Plane” button), or the stay on plane constraint with rotation allowed around the direction normal to the plane, useful in the case where the desired imaging trajectory is not planar (by pressing the “Rotate” button). When the user chooses one of the stay on plane options, either with or without rotation allowed, he or she is also given the option of using force assistance. In this case, the sonographer brings the probe head to a desired imaging location and pushes the probe against the patient until a viable image can be collected. At this point, the user can press the “Set Desired Contact Force” to assign the current contact force to the desired value. Then, by pressing the “Activate Force Assistance” button the constraints presented in (5.9) are added to the optimization problem, and the robot maintains the probe at the set contact force while the sonographer has the option of moving in the plane. This is useful in the case where the sonographer needs to lift the probe off the patient for readjustment but wants it to apply the same force as before.

Figure 5.8 shows the overall process flow for the co-robotic STRATUS imaging system described. At first, the user moves the probe to the desired initial position. At this point, a virtual fixture constraint can be activated, restricting the trajectory of the probe in the corresponding fashion. The sonographer then moves the US probe accordingly, collecting images throughout. The robot constantly tracks its joints and end effector state, as well as the current contact force, to determine if the velocity commands are feasible given the set constraints. If so, the robot moves accordingly. Otherwise, the robot restricts or the very least limits the motion in that direction. Once a sufficient number of poses and images have been acquired, the STRATUS reconstruction algorithm summarized in section 5.1 can be run, leading to one final extended synthesized B-mode image.

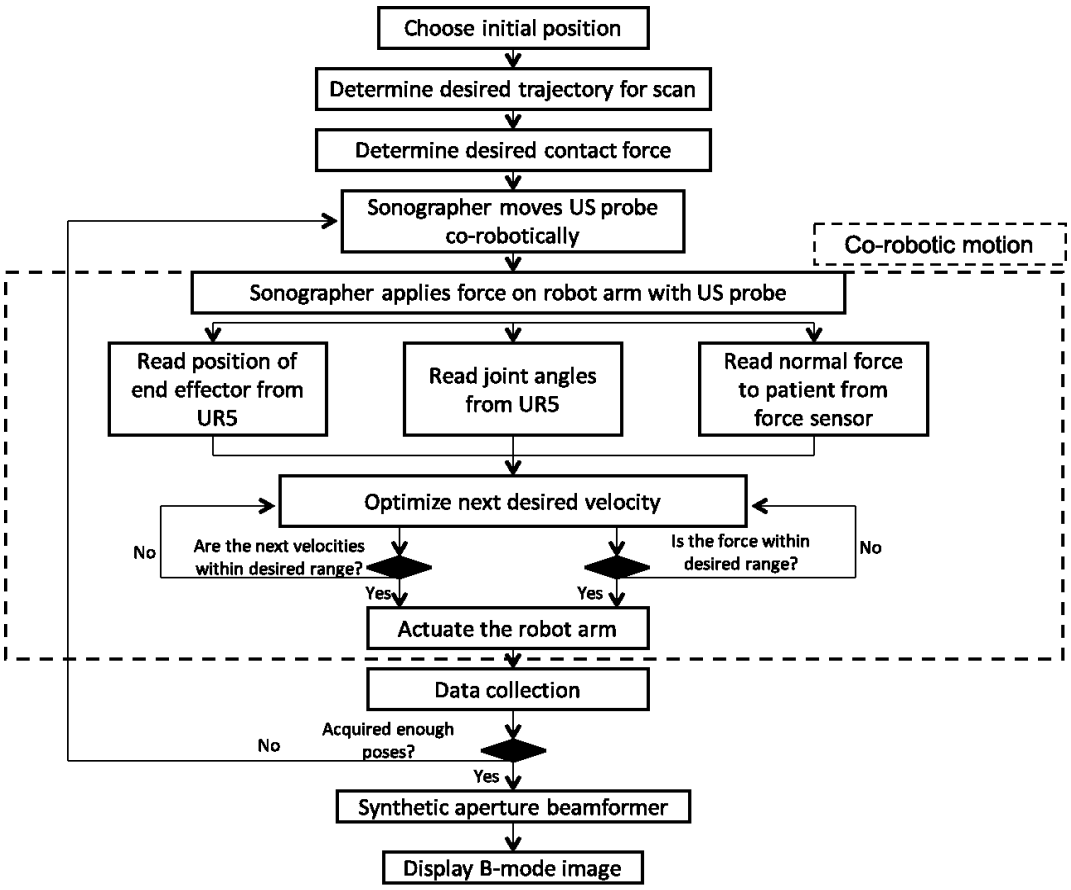

Figure 5.9 Cooperative robot control for STRATUS imaging: process flow.

5.6 Results and Discussion

Figure 5.10 shows the effect of the STRATUS image formation after scanning a planar multi-purpose tissue equivalent ultrasound phantom (Victoreen Instruments Co., Cleveland, OH, USA; shown in Figure 5.11) using virtual fixtures. In this case, a lateral in-plane motion was applied, and 105 poses were collected. Figure 5.10 (a) shows a single pose ultrasound B-mode image, while (b) and (c) show the results of using extended synthetic aperture ranges of 10 and 60 mm, respectively. In other words, as the probe is moved down the constrained trajectory, each slice in images (b) and (c) is a result of compounding B-mode images consecutively collected across either 10 or 60 mm. By integrating the information from all poses, the field-of view of the image expanded by 65.5

mm, and makes it possible to visualize many features not visible in the single pose image. The resolution of the point targets, shown by a yellow arrow in (a), improved as the aperture

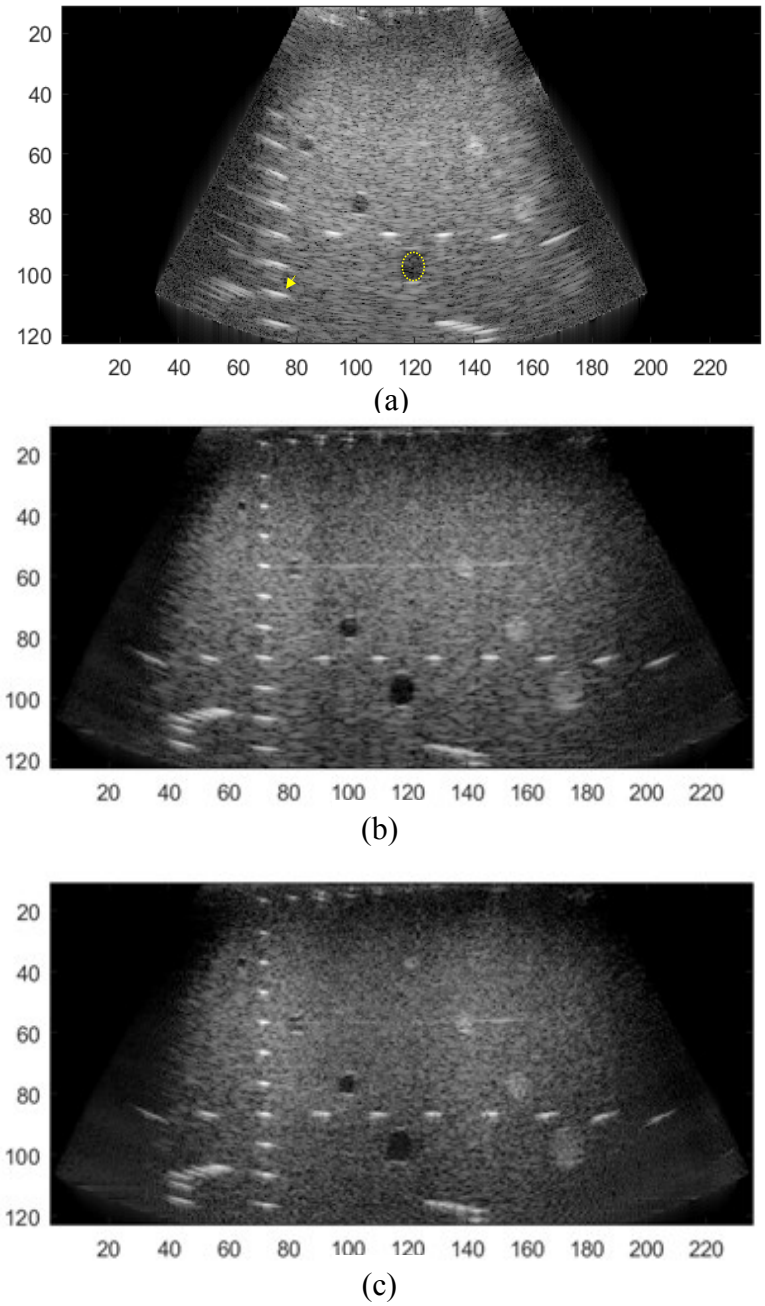

Figure 5.10 Effect of STRATUS. (a) Single pose B-mode ultrasound image on general US phantom. (b) STRATUS images synthesized with a motion range of 10 mm. (c) STRATUS images synthesized with a motion range 60 mm; field-of-view expanded by 65.5 mm.

size increased, and the contrast of the anechoic regions, shown with a yellow circle in (a), became more obvious. Similar results were observed with contact force regulation.

Table 5.1 shows a quantitative analysis of the imaging results from the same trials. The full width at half maximum (FWHM), an inverse measure of resolution, was measured at the point located at around 110 mm axially and 75 mm laterally. The contrast was calculated as a ratio between the mean intensity of the anechoic region and the mean intensity of the surrounding high intensity region. Signal-to-noise ratio (SNR) was

	Single	STRATUS: 10 mm	STRATUS: 60 mm
FWHM (mm)	**3.87**	**3.96**	**2.37**
Contrast (dB)	**-7.14**	**-13.24**	**-10.67**
SNR (dB)	**25.01**	**27.20**	**29.35**

Table 5.1 Quantitative Analysis of Ultrasound Image Improvement with STRATUS

computed as the ratio between the point target intensity and the standard deviation of the background region.

Figure 6.11 Planar general ultrasound phantom used in virtual fixtures experiments. Next steps will aim at imaging more anatomically accurate phantoms.

In these initial results, STRATUS showed an image quality improvement over conventional ultrasound with the 60 mm motion range across all three metrics. In the future, data will be collected using additional virtual fixtures. For example, while the results presented above come from images collected using the planar phantom shown in Figure 6.11, future work will focus on using the "rotate on plane" virtual fixture to collect imaging data from more anatomically-accurate phantoms such as a rounded abdominal phantom. Overall, the results in the planar phantom show the feasibility of the STRATUS-VF framework in improving image quality using low frequency ultrasound, which could change the paradigm of ultrasound imaging.

CHAPTER 6: FUTURE WORK AND CONCLUSIONS

As discussed in detail throughout this document, the various components of our robot-assisted ultrasound framework, including the dual-sensor force augmenting and virtual fixture capabilities, show promise in helping improve image quality and reduce the magnitude of the force and effort sonographers need to exert to acquire such images. Future work by existing and new members of our group will aim at improving the existing system. This chapter lists all proposed changes and improvements, as well as new applications of the existing framework.

6.1 Changes to Current System

One required change deals with the custom-designed probe holder described in Section 3.3. Some potential changes are described in Section 3.4. In short, one limitation of the current probe holder is the method with which and the material out of which it is manufactured. 3-D printed ABS is porous, highly deformable and uneven. While the current solution of adding the additional handle to the probe holder, as shown in Figure 3.6, behaved appropriately, it greatly increases the size of the design and makes it awkward to manipulate the probe. A new design made of a different material, such as aluminum and the addition of guiding mechanisms, such as spring plungers, would help make the probe holder easier to use.

Other potential next steps relate to the user studies performed and described in Chapter 4. As discussed, the results of our preliminary studies showed room for improvement in robot responsiveness. The two components that need to be addressed are the proper tuning of the variable admittance gains described in Section 3.5 and the lag

caused by the drop in sampling rate when collecting ultrasound images. Once these problems have been addressed, more participants will be recruited to test the changes.

Lastly, there is potential for improvement in the virtual fixtures and synthetic tracked aperture aspect of our robot assisted ultrasound system. Namely, the next step is to collect imaging data from a non-planar ultrasound phantom, such as one that models the human abdomen. This will allow us to test our "rotate on plane" virtual fixture and to validate its functionality.

6.2 Other Potential Applications

Beyond force-augmentation for imaging obese patients or virtual fixtures for synthetic tracked aperture, our system also has the potential to be used in a number of other applications including US tomography and US mirror imaging.

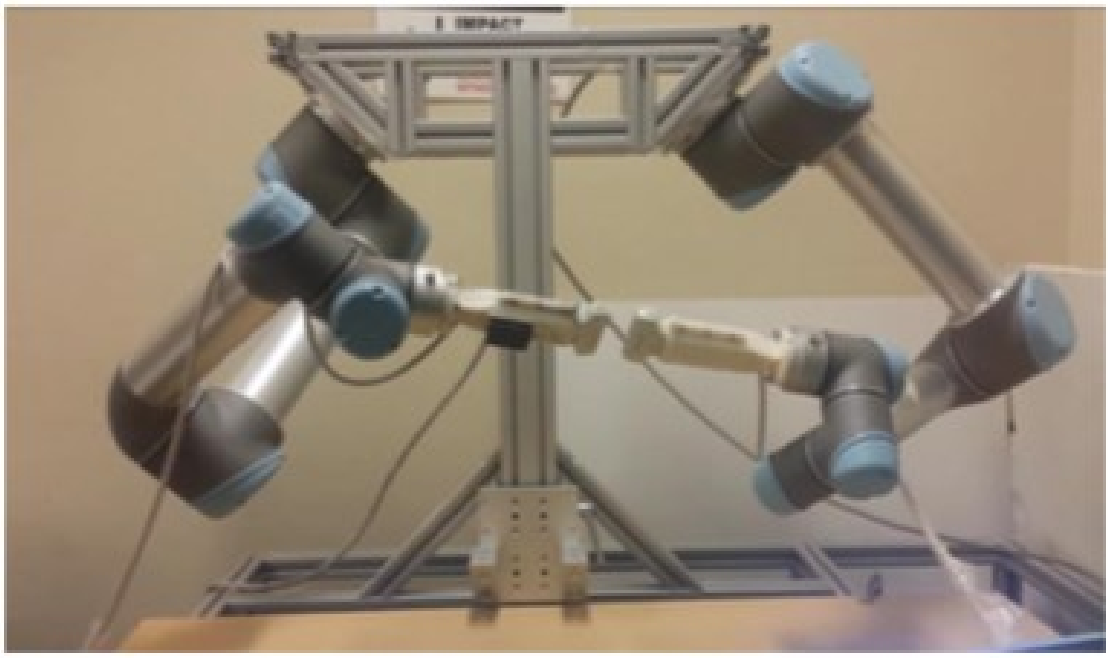

Figure 6.1 Dual arm robotic ultrasound system for ultrasound tomography [32]. Reprinted with permission from SPIE ©2015 SPIE.

In US tomography, a dual arm system previously developed by our group [31, 32] and seen in Figure 6.1 can be used to reconstruct an object's acoustic properties as two US probes, each being held by a separate robot, maintain alignment with each other. Using our system, one arm can be controlled collaboratively by the sonographer with our admittance control laws while the other matches its movements. As the human-controlled robot is placed on a patient or other volume to be imaged, the second approaches from the opposite side and applies a force of equivalent magnitude. Since it would be necessary to accurately measure the contact force against the patient without receiving crosstalk from the sonographer's manipulation forces, the dual-sensor setup and custom designed probe holder described in Chapter 3 would be useful. In addition, because the second probe is being controlled by a second robot without human interaction, it is necessary that only safe forces are being applied by the robot to the surface of the patient. The force limiting and "approached desired force" capabilities described in Sections 3.7 and 3.8, respectively, can help assure this.

Another application being investigated by our group is the use of the dual arm setup for safe mirrored ultrasound scanning of a patient's anatomy. As a sonographer performs a typical imaging procedure on one component of the patient's anatomy, a second robot mimics the clinician's movements in a mirrored fashion. In a procedure such as the imaging of both legs to check for deep vein thrombosis, a sonographer would be able to image both legs simultaneously, cutting the procedural time in half. As a result, valuable clinical resources would be saved. As in the ultrasound tomography application, our system has the capabilities for force control of the autonomous robot based on the admittance control of the human-controlled arm.

6.3 Conclusions

In conclusion, prior to this work, the use of admittance control and force augmentation in robot-assisted ultrasound had not been extensively studied. Similarly, the same can be said about the use of admittance control and virtual fixtures in synthetic aperture imaging. Overall, the work and results presented in this thesis show that robotic ultrasound can be used to facilitate, expedite, and improve the results of ultrasound procedures while reducing the strain placed on the human sonographer. We have described a system architecture that can be used to provide assistance to an US clinician through admittance control and force augmentation. The results from preliminary user studies show that this method is capable of facilitating high-contact-force imaging, and of reducing grip force, a factor highly correlated with the development of work-related musculoskeletal disorders in ultrasonographers. In addition, we have shown that virtual fixtures can be used to constrain the motion of a robot to stay on in-plane trajectories. This has the proven capability to reconstruct synthetic tracked aperture images with expanded fields of view, and with improved resolution, contrast and signal-to-noise ratio. In the future, we plan to improve our current system further based on the results collected thus far. We will continue to validate it by recruiting more participants for the user study and by collecting additional imaging data with newly implemented virtual fixtures.

APPENDICES

Appendix 1: Robot Kinematics Calculation

The transformation $g_{be}(\theta) \in SE(3)$ defined in (3.3) can be calculated by a number of methods. One such method is to use the get_forward_kin() method of the URScript language used to command the UR5 [38]. The resulting vector, $k \in \mathbb{R}^6$ represents the tool pose given as $k = \begin{bmatrix} x \\ y \\ z \\ T_x \\ T_y \\ T_z \end{bmatrix}$ where $p = \begin{bmatrix} x \\ y \\ z \end{bmatrix}$ represents the location in 3D space of the end effector in robot base coordinates and T_x, T_y and T_z are the axis-angle parameterization of the end effector orientation. The rotation matrix R is calculated using the Rodrigues formula shown in [40] as:

$$R = e^{\theta\hat{\omega}} = I + \sin(\theta)\hat{\omega} + (1 - \cos(\theta))\hat{\omega}^2 \qquad \text{(A1.1)}$$

where $\omega \in \mathbb{R}^3$ is a unit vector which specifies a direction of rotation and $\theta \in \mathbb{R}$ is the angle of rotation in radians. Since the UR5 represents all rotations using the axis-angle parameterization, θ and ω can be calculated from the values of T_x, T_y and T_z of the robot tool tip at the time of measurement as follows:

$$\theta = \left\| \begin{bmatrix} T_x & T_y & T_z \end{bmatrix} \right\|; \quad \omega = \frac{\begin{bmatrix} T_x & T_y & T_z \end{bmatrix}}{\theta} \qquad \text{(A1.2)}$$

where $\|\cdot\|$ is the vector norm.

An alternate method of calculating the forward kinematics of the UR5 is to use the produce of exponential (POE) formula, also presented by [40]. For a 6-DOF robot like the UR5, the POE formula is:

$$g_{be}(\theta) = e^{\hat{\xi}_1\theta_1}e^{\hat{\xi}_2\theta_2}e^{\hat{\xi}_3\theta_3}e^{\hat{\xi}_4\theta_4}e^{\hat{\xi}_5\theta_5}e^{\hat{\xi}_6\theta_6}g_{be}(0) \text{ (A1.3)}$$

Here, $\xi_i \in \mathbb{R}^6 = \begin{bmatrix} -\omega_i \times q_i \\ \omega_i \end{bmatrix} = \begin{bmatrix} v_i \\ \omega_i \end{bmatrix}$ is the unit twist that corresponds to the screw motion for the ith joint, $\omega_i \in \mathbb{R}^3$ is a unit vector in the direction of the twist axis, and $q_i \in \mathbb{R}^3$ is any point on the axis. $\hat{\xi}_i$ is the wedge of ξ_i and is defined as $\begin{bmatrix} \hat{\omega}_i & v_i \\ 0 & 0 \end{bmatrix}$, $\theta = [\theta_1 \quad \theta_2 \quad \theta_3 \quad \theta_4 \quad \theta_5 \quad \theta_6]^T$ are the positions in radians of each of the robot's joint at any given time, which can be collected from the robot using get_joint_positions(), and $g_{be}(0)$ is the rigid transformation between the robot end-effector e and the robot base b when the manipulator is in its reference configuration, selected as $\theta = \left[0 \quad -\frac{\pi}{2} \quad 0 \quad 0 \quad -\frac{\pi}{2} \quad 0\right]^T$. The robot in this configuration is shown in Figure A1.1, acquired from the "Virtual Experimentation Platform" (V-REP; Coppelia Robotics, Zurich, Switzerland). The value of each ξ_i is dependent on the distance between the 1st and i^{th} joint, as well as the axis of rotation of that i^{th} joint.

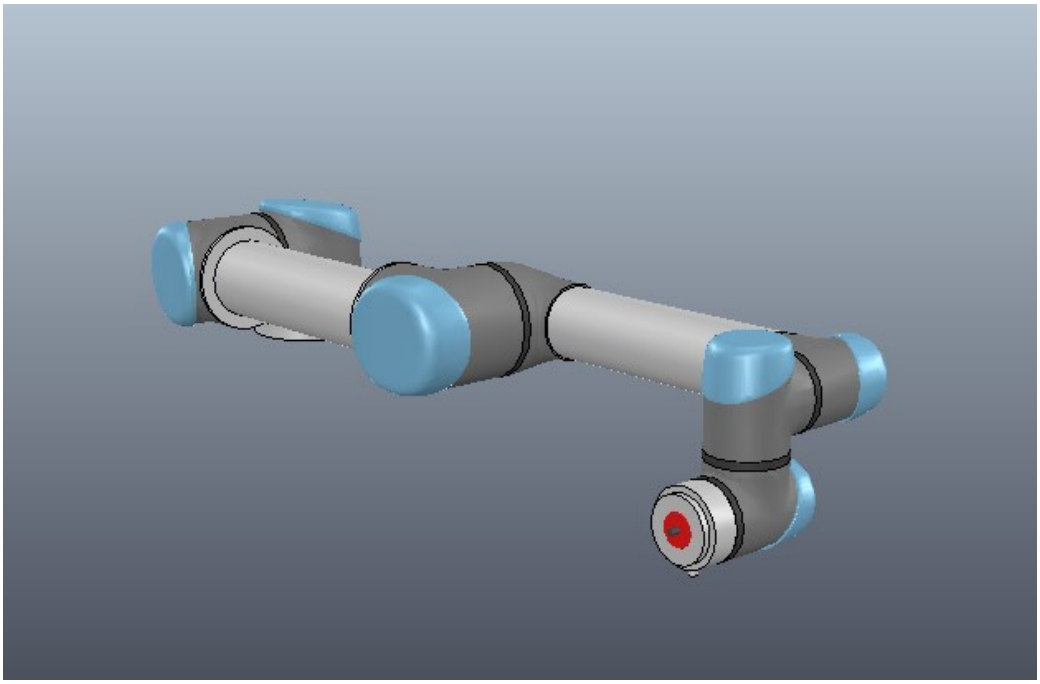

Figure A1.1 Base Configuration of UR5, used to calculated the forward kinematics of robot

Appendix 2: Weighted Moving Average Smoothing Filter

As described in section 3.3, in order to remove the significant jitter present in the control of the UR5, a low-pass filter algorithm must be implemented. As an original attempt, a weighted moving average filter was applied. Using this method, each Cartesian end-effector velocity command sent to the robot at time t is a linear combination of the velocity calculation based on the current force readings and the average of a certain number of previous velocity commands:

$$\boldsymbol{v_{desired}} = w * \boldsymbol{v_{curr}} + (1 - w) * \boldsymbol{v_{prev}} \text{ (A2.1)}$$

where w defines the impact of the current and averaged past velocity commands in the calculation of the filtered value. The value of w and the quantity n of previous velocities to include in this calculation to ensure both smooth transitions between commands and rapid responses to sudden changes were determined experimentally to be in the ranges of 0.18-0.20 and 11-15, respectively, depending on the desired level of compliance. Figure A2.1 shows the effect of this moving average filter. While the jitter is significantly reduced,

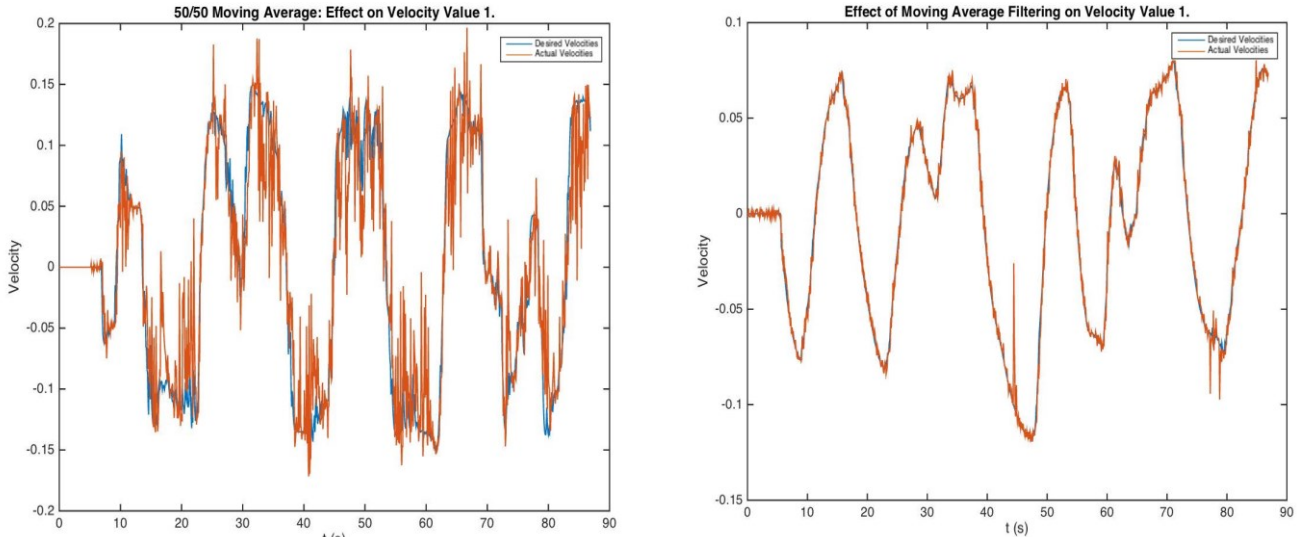

Figure A2.1 Effect of Moving Average Filter for Linear X Velocity. Left: Current and average of 10 previous velocity commands are weighted evenly. Right: Current command is weighted by 18% while the average of 15 past commands is weighted by 82%

the method was not because of its dependence on the sampling rate; such filters lead to time latency, or lag, equivalent to n (the number of previous samples) times the sampling period. Therefore, as the sampling rate decreases, for example when ultrasound images are collected concurrently during robot control, lag increases. The ultimately implemented "1€" filter, described in detail in section 3.3, is able to balance jitter and lag better and was therefore a better fit for our needs.

Appendix 3: Robot Jacobian Calculation

The Jacobian matrix $J(\theta) \in \mathbb{R}^{6x6}$ is used to related desired robot joint velocities to the corresponding Cartesian end effector velocities, as described in section 3.3. Deriving the robot kinematics equation with respect to time leads to the Jacobian. For the UR5 it can be calculated using the product of exponentials (POE) formula as in [40]:

$$J(\theta) = [\xi_1 \quad \xi'_2 \quad \cdots \quad \xi'_6]$$
$$\xi'_i = Ad_{e^{\hat{\xi}_1\theta_1 \ldots e^{\hat{\xi}_{i-1}\theta_{i-1}}}}\xi_i;\ 2 < i < 6 \tag{A3.1}$$

Here, ξ_i is the unit twist vector explained in the definition of (A1.3), and $Ad \in \mathbb{R}^{6x6}$ is the adjoint transformation, as defined in (3.5), which transforms twist coordinates from the frame of the first joint to the frame of the i^{th} joint, using the product of exponentials formula $e^{\hat{\xi}_1\theta_1} \ldots e^{\hat{\xi}_{i-1}\theta_{i-1}}; 2 < i < 6$, similar to that defined in (A1.3). Therefore, the i^{th} column of the Jacobian corresponds to the i^{th} joint twist transformed by the transformation from the robot base to the coordinate frame of the $(i-1)^{th}$ joint. This means that the contribution of the i^{th} joint velocity to the end-effector velocity is independent of the configuration of later joints in the chain.

Appendix 4: Contact Force Control: PID Controller

As discussed in section 4.6, it is possible to set a desired contact force that the probe must apply to the patient. Originally, instead of the force constraint method defined in (4.15) and (4.16), a PID controller was used to account for the error between desired the application force value and the actual value in the z direction measured by the FT-150. This control scheme allowed that the force pressed against the patient is reached, stabilizes quickly and overshoot is minimized to assure safety. In short, a PID controller rectifies the error in the error in the following manner:

$$u(t) = K_p * e(t) + K_i \int_0^t e(\bar{t})d\bar{t} + K_d * \frac{de}{dt} \quad \text{(A4.1)}$$

where e(t) is the error at the current time point and is defined by:

$$e(t) = f_{z,desired}(t) - f_{z,measured}(t) \quad \text{(A4.2)}$$

The e(t) component makes up the proportional (P) term. The accumulation of past values of error calculated throughout the duration of the program are depicted as the integral (I) term. Finally, the possible future values of error are accounted for in the derivative term (D), in which the current rate of change in the error is measured. These three components are scaled by separate gain coefficients, depicted above as K_p, K_i, and K_d, respectively. The resulting u(t) is added to the measured force to better approach the goal. These coefficients were determined through experimentation to be around 0.58, 0.00116, and 0.1714, respectively. The effects of adding P, PI, and finally PID control are shown in Figure A4.1.

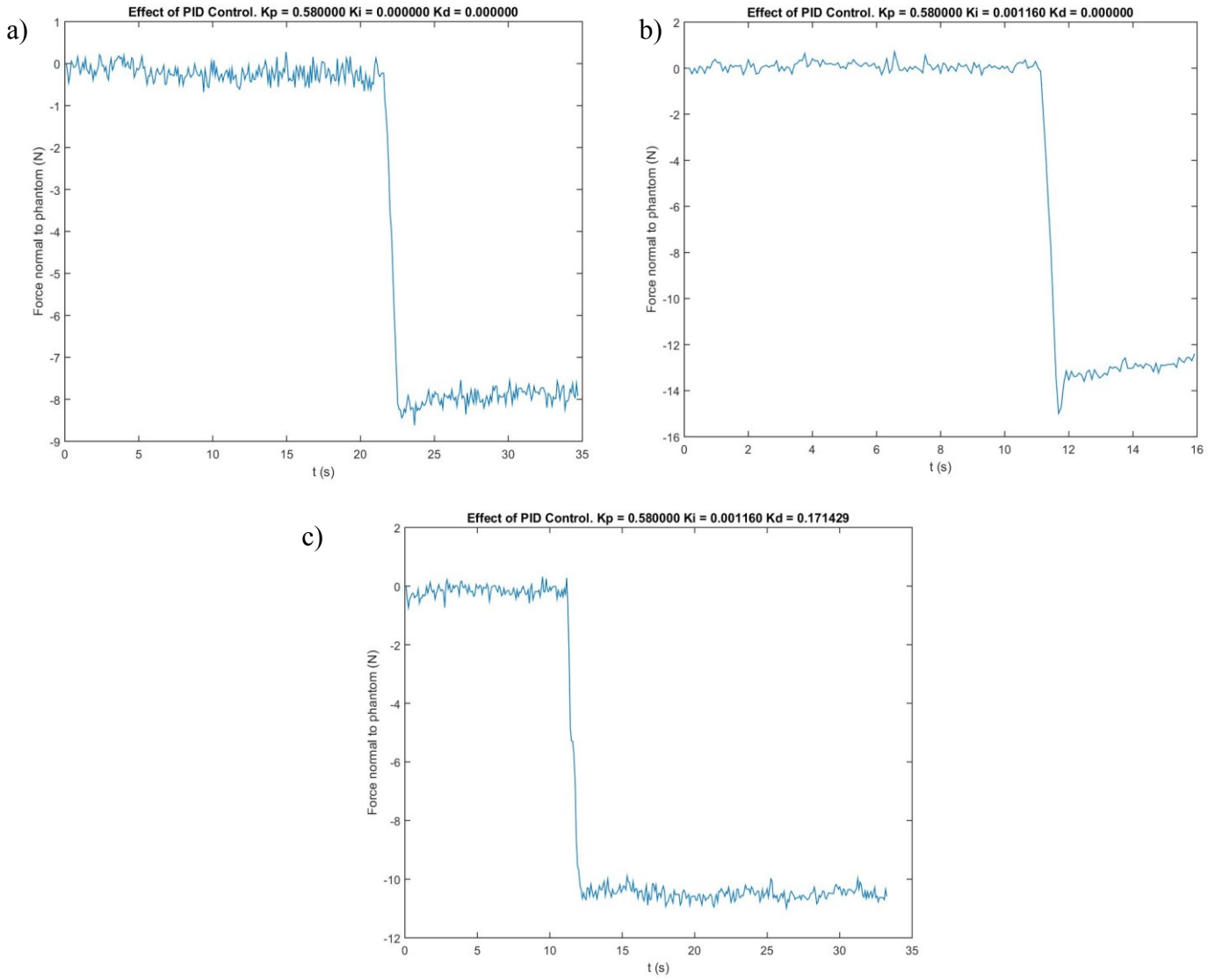

Figure A4.1 Comparison of P, PI, and PID control a) Effect of Implementing Proportional Control Scheme. Desired force is not reached. b) Effect of Implementing Proportional-Integral Control Scheme. Overshoot Occurs. c) Effect of Implementing Proportional

In these test cases, the US probe begins approximately 120 mm above the surface of an US phantom pointed perpendicular to the surface of the phantom, as seen in Figure A4.2. The desired application force was preset to 10 N in each case. It is clear from Figure A4.1 that adding P control does not ensure that the actual desired force is reached. Also implementing I comes close to rectifying this but causes an overshoot and stabilizes at a

higher-magnitude force. Adding a D term into the calculation removes this overshoot and allows the system to stabilize at approximately the correct desired force.

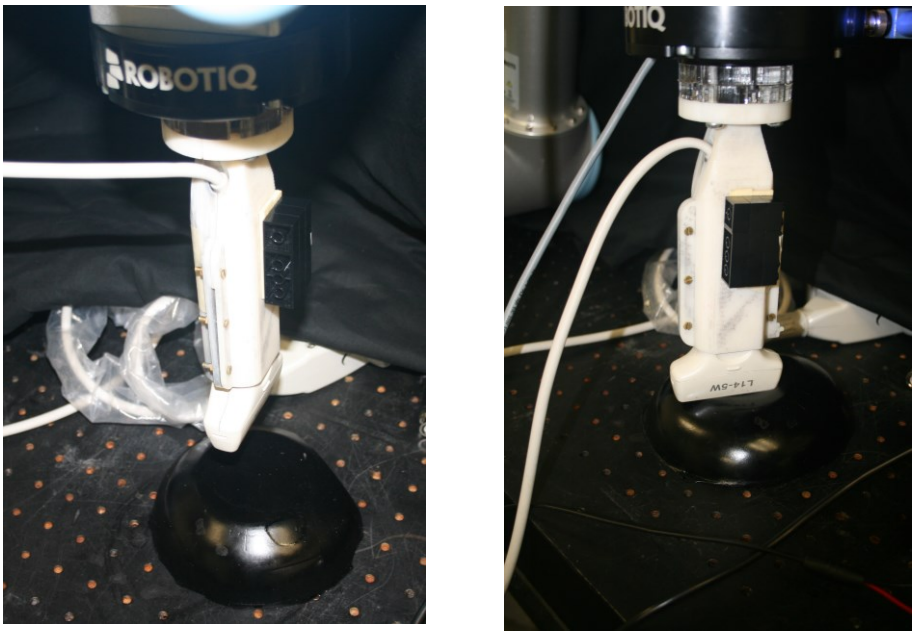

Figure A4.2 Setup for Application Force Testing. Left: Probe is approximately 120 mm above an US phantom. Right: Probe is contact with phantom maintaining constant force of 10 N

In practice, the force measured by the FT-150 in the z linear direction is replaced by the controller output.

$$F_{z,set} = u(t) \quad \text{(A4.3)}$$

The updated force vector is what was used to calculate the end-effector velocity as described in Chapter 3 above. As a result, if the ultrasound probe is ever lifted off of the patient or if it is shifted to a part of the patient's anatomy with a different distance to the surface of the probe, the robot will automatically return the probe to the pre-set force once let go.

Appendix 5: User Study Questionnaire

Ease of Use Survey: UR5 Robotic Assisted Ultrasound

1. How much experience do you have with handling ultrasound-imaging systems (select all that apply)?
    - ❑ Clinical Experience
    - ❑ Research Experience
    - ❑ Other Experience
    - ❑ No Experience

2. How easy/difficult was it to perform the imaging tasks using freehand ultrasound (without robotic assistance)?
    - ❑ Extremely easy (1)
    - ❑ Somewhat easy (2)
    - ❑ Neither easy nor difficult (3)
    - ❑ Somewhat difficult (4)
    - ❑ Extremely difficult (5)

3. How easy/difficult was it to perform the imaging tasks with UR5 robotic assistance?
    - ❑ Extremely easy (1)
    - ❑ Somewhat easy (2)
    - ❑ Neither easy nor difficult (3)
    - ❑ Somewhat difficult (4)
    - ❑ Extremely difficult (5)

4. How physically strenuous was the imaging task using freehand?
    - ❑ Not at all strenuous (1)
    - ❑ Minimally strenuous (2)
    - ❑ Moderately strenuous (3)
    - ❑ Very strenuous (4)
    - ❑ Extremely strenuous (5)

5. How physically strenuous was the imaging task using robotic assistance?
    - ❑ Not at all strenuous (1)
    - ❑ Minimally strenuous (2)
    - ❑ Moderately strenuous (3)
    - ❑ Very strenuous (4)
    - ❑ Extremely strenuous (5)

6. How intuitive was the manipulability of the UR5 robotic system compared to freehand (only using ultrasound probe)?
    - ❑ Much less intuitive (1)
    - ❑ Somewhat less intuitive (2)
    - ❑ Neither more nor less intuitive (3)
    - ❑ Somewhat more intuitive (4)
    - ❑ Much more intuitive (5)

Appendix 6: Error Analysis

In this section, we continue the error analysis performed by Aalamifar et al. for the dual robot system previously developed by the authors [32]. As mentioned in Section 7.2, this dual arm setup can be combined with force assistance for US tomography and other applications. Therefore, how error propagates through this system is relevant for our purposes as well. The transformation between relevant coordinate frames is shown in Figure A6.1 and the overall method used here and in [32] is summarized below.

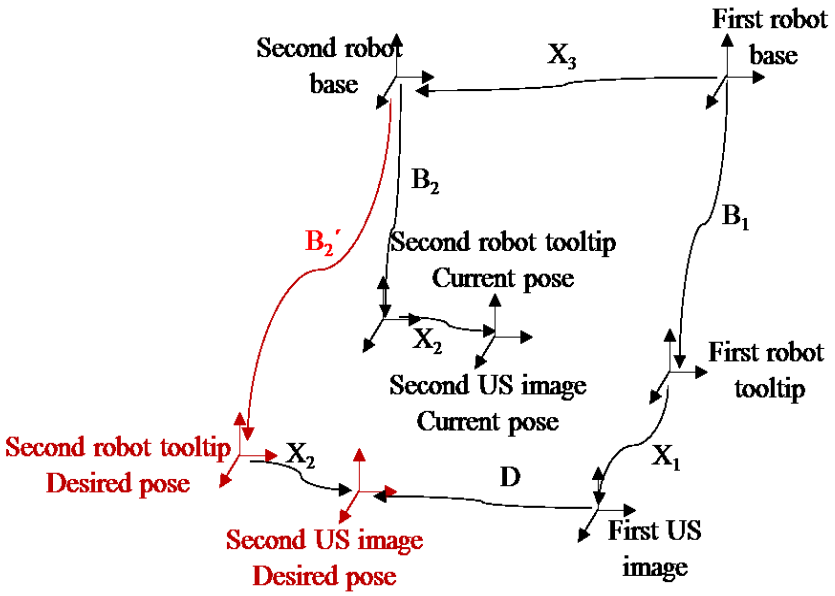

Figure A6.1 Transformations involved in US tomography setup for calculating the desired second arm pose such that the two US probes are aligned (from [32]). Reprinted with permission from SPIE ©2015 SPIE.

The transformation D from the coordinate frame of the first US image to that of the second image can be calculated using the following equation:

$$D = X_1^{-1} B_1^{-1} X_3 B_2 X_2 \quad \text{(A5.1)}$$

Accounting for inaccuracies of the system, the value of ΔD, the measurement error in D can be calculated using the values of the transformation matrices and their respective errors:

$$\Delta D = D^{-1}\Delta X_1^{-1}X_1^{-1}\Delta B_1^{-1}B_1^{-1}X_3\Delta X_3 B_2\Delta B_2 X_2\Delta X_2 \quad \text{(A5.2)}$$

Since the two probes should be aligned in front of each other, the desired D matrix is a rotation of 180 degrees about the x-axis and a translation along the z-axis. This translation was selected randomly to be [0,150] mm. We defined a random transformation matrix from the first robot base to its tooltip B_1 and calculated B_2 using equation (A5.1). All of the matrices in (A5.2) are elements of SE(3), as defined in equation (3.3). In terms of the error matrices, the rotation, as defined by the Rodrigue's formula shown in (A1.1), can be simplified to:

$$R \approx I + \theta\hat{\omega} \quad \text{(A5.3)}$$

when θ is small. In our case, we selected a maximum rotation angle error of 1 degree (0.0175 radian) and a maximum translation error of 0.1 mm. The axes of rotational and translational error were picked randomly. At each time point, we picked the current rotation and translational errors from zero to maximum error randomly for the robot transformations. However, the calibration matrices have a constant error and were therefore held constant throughout the process after having been generated randomly.

Based on the results presented by Aalamifar et. al., attempts were made to reduce the error propagation by changing the values of the non-error matrices. To this end, it was hypothesized that altering the design of the US probe holder described in Section 2: System Overview above such that the displacement in the z direction could be significantly reduced would help to reduce the overall error. To test this theory, a change of the translational components of both matrices X_1 and X_2 to [0.06; 0; 0.005] mm (with a vector norm of 0.0602) from the original [-0.0026; -0.0010; 0.1706] mm (with a vector norm of 0.1706) was attempted and the results in the form of the values of ΔD are shown in Figure A6.2. It

is clear from these results and those presented in the previous analysis that there is no significant improvement in the error, leading to the conclusion that the effect of the distance between the probe and robot's end effector is negligible. Only the individual transform's errors seem to have a significant effect on the overall value of ΔD so every effort must be made to ensure these values are as small as possible.

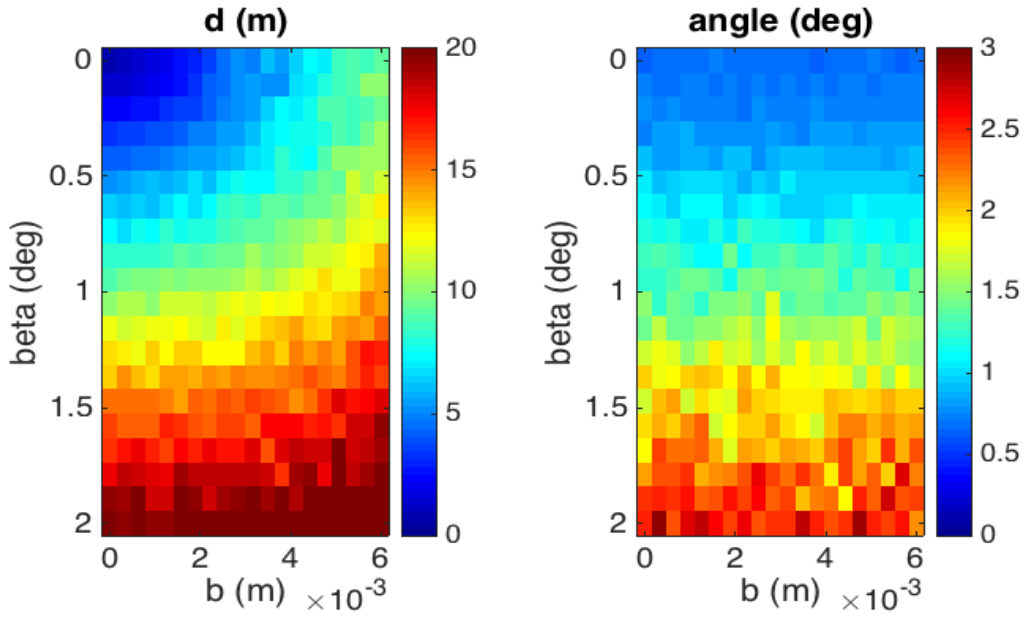

Figure A6.2 Result of shortening distance between robot end effector and US probe tip on value of ΔD. The effect is negligible

We now consider the case in which D is defined to be the transform from the coordinate frame of the second US image to that of the first image, instead of the opposite relationship explored above. Therefore,

$$D = X_2^{-1} B_2^{-1} {X_3}^{-1} B_1 X_1 \text{ (A5.4)}$$

In this situation, the error in D, ΔD becomes:

$$\Delta D = D^{-1} \Delta X_2^{-1} X_2^{-1} \Delta B_2^{-1} B_2^{-1} \Delta X_3^{-1} X_3^{-1} B_1 \Delta B_1 X_1 \Delta X_1 \text{ (A5.5)}$$

The values of all the matrices are calculated or randomly generated as above. The results of the error propagation can be seen in Figure A6.3.

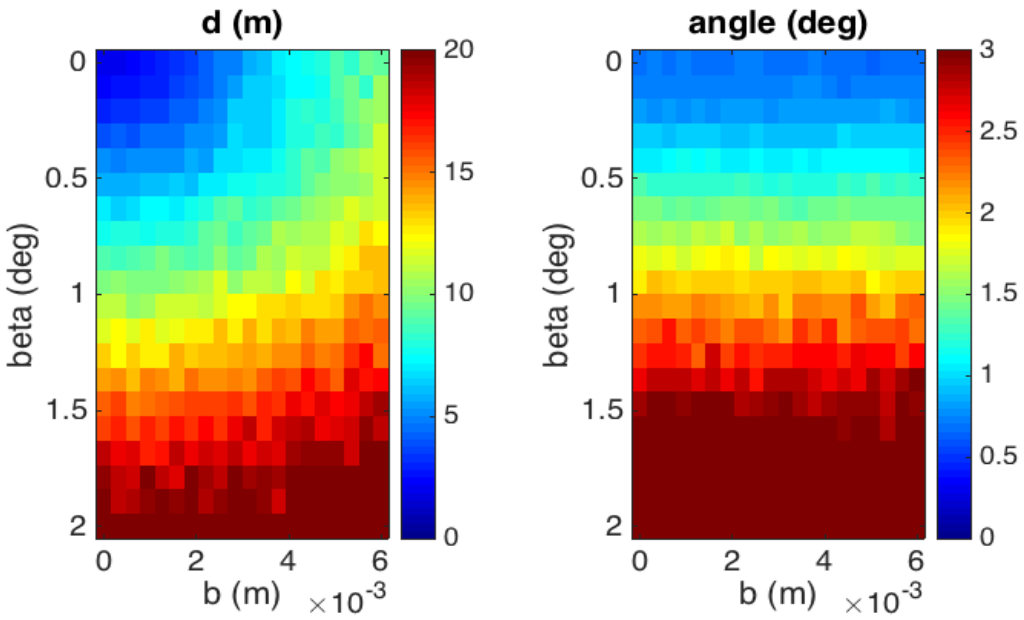

Figure A6.3 Result of redefining D as transform from second US image to first

The results of Figure A6.3 show a significant increase in the rotational error of the overall system. This can be explained by the exchange of positions of $X_3\Delta X_3$ in (11) to $\Delta X_3^{-1}X_3^{-1}$ in (A5.5) caused by taking the inverse of two multiplied SE(3) matrices ($(AB)^{-1} = B^{-1}A^{-1}$). As previously mentioned, the values of the Δ or error matrices have the greatest impact on the value of the overall error. Additionally, by the properties of rotation matrices and matrix multiplication, the farther left a value appears in a matrix chain, the greater effect it has. Therefore, because of the extra inversion that occurs in this formulation, the value of ΔX_3, or more specifically, $\Delta X_3{}^{-1}$ has a greater impact on the final value of ΔD. All else being equal, it is therefore preferable to define D as the transformation from US image 1 to US image 2 in order to minimize the propagation of error throughout the system.

CITATIONS

[1] Priester, Alan M., Sriraam Natarajan, and Martin O. Culjat. "Robotic ultrasound systems in medicine." *Ultrasonics, Ferroelectrics, and Frequency Control, IEEE Transactions on* 60, no. 3 (2013): 507-523.

[2] Wells, Peter NT, and Hai-Dong Liang. "Medical ultrasound: imaging of soft tissue strain and elasticity." Journal of the Royal Society Interface 8.64 (2011): 1521-1549.

[3] Rousseau, Thierry, Nicolas Mottet, Guillaume Mace, Carole Franceschini, and Paul Sagot. "Practice guidelines for prevention of musculoskeletal disorders in obstetric sonography." Journal of Ultrasound in Medicine 32, no. 1 (2013): 157-164.

[4] Haidegger, Tamas, et al. "Force sensing and force control for surgical robots." 7th IFAC Symposium on Modeling and Control in Biomedical Systems. Vol. 7. No. 1. 2009.

[5] Nathoo, N, Cavusoglu, MC, Vogelbaum, MA, Barnett, GH 2005, In Touch with Robotics: Neurosurgery for the Future, Journal of Neurosurgery; Vol.56/3, pp.421-433.

[6] Taylor, RH, Menciassi, A, Fichtinger, G, Dario, P, 2008, Medical Robotics and Computer-Integrated Surgery, Chapter 52. in Springer Handbook of Robotics; eds. Siciliano, B, Kathib, O, Springer, Berlin.

[7] Xia, Tian, et al. "An integrated system for planning, navigation and robotic assistance for skull base surgery." The International Journal of Medical Robotics and Computer Assisted Surgery 4.4 (2008): 321-330.

[8] Haidegger, Tamas, Tian Xia, and Peter Kazanzides. "Accuracy improvement of a neurosurgical robot system." Biomedical Robotics and Biomechatronics, 2008. BioRob 2008. 2nd IEEE RAS & EMBS International Conference on. IEEE, 2008.

[9] He, Xingchi, et al. "A multi-function force sensing instrument for variable admittance robot control in retinal microsurgery." Robotics and Automation (ICRA), 2014 IEEE International Conference on. IEEE, 2014.

[10] Kumar, Rajesh, et al. "Preliminary experiments in cooperative human/robot force control for robot assisted microsurgical manipulation." Robotics and Automation, 2000. Proceedings. ICRA'00. IEEE International Conference on. Vol. 1. IEEE, 2000.

[11] Balicki, Marcin, et al. "Micro-force sensing in robot assisted membrane peeling for vitreoretinal surgery." Medical Image Computing and Computer-Assisted Intervention–MICCAI 2010 (2010): 303-310.

[12] Schoenfeld, Alex. "Ultrasonographer's wrist–an occupational hazard. "Ultrasound in Obstetrics & Gynecology 11.5 (1998): 313-316.

[13] Village, Judy, and Catherine Trask. "Ergonomic analysis of postural and muscular loads to diagnostic sonographers." International Journal of Industrial Ergonomics 37.9 (2007): 781-789.

[14] Silverstein, Barbara A. THE PREVALENCE OF UPPER EXTREMITY CUMULATIVE TRAUMA DISORDERS IN INDUSTRY (ERGONOMIES, OCCUPATIONAL EPIDEMIOLOGY). University of MICHIGAN, 1985.

[15] Maxwell, Cynthia, and Phyllis Glanc. "Imaging and obesity: a perspective during pregnancy." American Journal of Roentgenology 196.2 (2011): 311-319.

[16] Evans, Kevin, Shawn Roll, and Joan Baker. "Work-related musculoskeletal disorders (WRMSD) among registered diagnostic medical sonographers and vascular technologists: a representative sample." Journal of Diagnostic Medical Sonography (2009).

[17] "Occupational Outlook Handbook: Diagnostic Medical Sonographers and Cardiovascular Technologists and Technicians, Including Vascular Technologists." U.S. Bureau of Labor Statistics. U.S. Bureau of Labor Statistics. Web. 11 Apr. 2016.

[18] Monfaredi, Reza, et al. "Robot-assisted ultrasound imaging: Overview and development of a parallel telerobotic system." Minimally Invasive Therapy & Allied Technologies 24.1 (2015): 54-62.

[19] Boctor, Emad M., et al. "A dual-armed robotic system for intraoperative ultrasound guided hepatic ablative therapy: a prospective study." Robotics and Automation, 2004. Proceedings. ICRA'04. 2004 IEEE International Conference on. Vol. 3. IEEE, 2004.

[20] Ding, Jienan, et al. "Robotically assisted ultrasound interventions." Medical Imaging. International Society for Optics and Photonics, 2008.

[21] Krupa, Alexandre. "Automatic calibration of a robotized 3D ultrasound imaging system by visual servoing." Robotics and Automation, 2006. ICRA 2006. Proceedings 2006 IEEE International Conference on. IEEE, 2006.

[22] Janvier, Marie-Ange, et al. "Performance evaluation of a medical robotic 3D-ultrasound imaging system." Medical image analysis 12.3 (2008): 275-290.

[23] Hong, J., et al. "An ultrasound-driven needle-insertion robot for percutaneous cholecystostomy." Physics in Medicine and Biology 49.3 (2004): 441.

[24] Salcudean SE, Zhu WH, Abolmaesumi P, Bachmann S, Lawrence PD. A robot system for medical ultrasound. 9th International Symposium of Robotics Research (ISRR); Snowbird; 1999. p 152–9.

[25] Koizumi, Norihiro, Shin'ichi Warisawa, Mitsuru Nagoshi, Hiroyuki Hashizume, and Mamoru Mitsuishi. "Construction methodology for a remote ultrasound diagnostic system." Robotics, IEEE Transactions on 25, no. 3 (2009): 522-538.

[26] Vieyres, Pierre, et al. "The TERESA project: from space research to ground tele-echography." Industrial robot: an international journal 30.1 (2003): 77-82.

[27] A. Vilchis-Gonzalez, J.C. Avila-Vilchis, A. Garcia-Torres, "TERMI Robot", CERMA, 2007, Electronics, Robotics and Automotive Mechanics Conference, Electronics, Robotics and Automotive Mechanics Conference 2007, pp. 464-469, doi:10.1109/CERMA.2007.130

[28] Solazzi, M., et al. "Kinematic design of a gravity compensated robot for device for ultrasound examination and assessment of endothelial dysfunction." 12th IFToMM World Congress. 2007.

[29] Nakadate, Ryu, Jorge Solis, Atsuo Takanishi, Motoaki Sugawara, Kiyomi Niki, and Eiichi Minagawa. Development of the Ultrasound Probe Holding Robot WTA-1RII and an Automated Scanning Algorithm based on Ultrasound Image Feedback. Springer Vienna, 2010.

[30] Mathiassen, Kim, et al. "An Ultrasound Robotic System Using the Commercial Robot UR5." Frontiers in Robotics and AI 3 (2016): 1.

[31] Aalamifar, Fereshteh, et al. "Enabling technologies for robot assisted ultrasound tomography: system setup and calibration." SPIE Medical Imaging. International Society for Optics and Photonics, 2014.

[32] Aalamifar, Fereshteh, Dengrong Jiang, Haichong K. Zhang, Alexis Cheng, Xiaoyu Guo, Rishabh Khurana, Iulian Iordachita, and Emad M. Boctor. "Co-robotic ultrasound tomography: dual arm setup and error analysis." In SPIE Medical Imaging, pp. 94190N-94190N. International Society for Optics and Photonics, 2015.

[33] Sen, H. Tutkun, et al. "A cooperatively controlled robot for ultrasound monitoring of radiation therapy." Intelligent Robots and Systems (IROS), 2013 IEEE/RSJ International Conference on. IEEE, 2013.

[34] Nakadate, Ryu, Yasuaki Tokunaga, Jorge Solis, Atsuo Takanishi, Eiichi Minagawa, Motoaki Sugawara, Kiyomi Niki, and Akiko Saito. "Development of robot assisted measurement system for abdominal ultrasound diagnosis." In Biomedical Robotics and Biomechatronics (BioRob), 2010 3rd IEEE RAS and EMBS International Conference on, pp. 367-372. IEEE, 2010.

[35] Masuda, Kohji, Yuuki Takachi, Yasuhiro Urayama, and Takashi Yoshinaga. "Development of support system to handle ultrasound probe by coordinated motion with medical robot." In Engineering in Medicine and Biology Society, EMBC, 2011 Annual International Conference of the IEEE, pp. 4519-4522. IEEE, 2011.

[36] Pierrot, François, Etienne Dombre, Eric Dégoulange, Loïc Urbain, Pierre Caron, Sylvie Boudet, Jérome Gariépy, and Jean-Louis Mégnien. "Hippocrate: a safe robot arm for medical applications with force feedback." Medical Image Analysis 3, no. 3 (1999): 285-300.

[37] Casiez, Géry, Nicolas Roussel, and Daniel Vogel. "1€ filter: a simple speed-based low-pass filter for noisy input in interactive systems." Proceedings of the SIGCHI Conference on Human Factors in Computing Systems. ACM, 2012.

[38] Universal Robots. User Manual: UR5, February 2013.

[39] Universal Robots. The URScript Programming Language: For version 1.5

[40] Kazanzides, Peter, Joel Zuhars, Brent Mittelstadt, and Russell H. Taylor. "Force sensing and control for a surgical robot." In Robotics and Automation, 1992. Proceedings., 1992 IEEE International Conference on, pp. 612-617. IEEE, 1992.

[41] Murray, Richard M., et al. A mathematical introduction to robotic manipulation. CRC press, 1994.

[42] Funda, Janez, et al. "Constrained Cartesian motion control for teleoperated surgical robots." Robotics and Automation, IEEE Transactions on 12.3 (1996): 453-465.

[43] Li, Ming, Ankur Kapoor, and Russell H. Taylor. "A constrained optimization approach to virtual fixtures." Intelligent Robots and Systems, 2005. (IROS 2005). 2005 IEEE/RSJ International Conference on. IEEE, 2005.

[44] Li, Ming, and Russell H. Taylor. "Spatial motion constraints in medical robot using virtual fixtures generated by anatomy." Robotics and Automation, 2004. Proceedings. ICRA'04. 2004 IEEE International Conference on. Vol. 2. IEEE, 2004.

[45] Li, Ming, and Russell H. Taylor. "Optimum robot control for 3d virtual fixture in constrained ent surgery." Medical Image Computing and Computer-Assisted Intervention-MICCAI 2003. Springer Berlin Heidelberg, 2003. 165-172.

[46] Üneri, Ali, et al. "New steady-hand eye robot with micro-force sensing for vitreoretinal surgery." Biomedical Robotics and Biomechatronics (BioRob), 2010 3rd IEEE RAS and EMBS International Conference on. IEEE, 2010.

[47] Smith-Guerin, N., et al. "Clinical validation of a mobile patient-expert tele-echography system using ISDN lines." Information Technology Applications in Biomedicine, 2003. 4th International IEEE EMBS Special Topic Conference on. IEEE, 2003.

[48] Tornifoglio, Shane Vincent. "Development and Application of a Portable System to Reliably Measure Grip Forces Using Thin-Film Force Sensors." (2012).

[49] "FlexiForce A201 Sensor." Tekscan. Tekscan, 13 Nov. 2014. Web. 23 Feb. 2016. <https://www.tekscan.com/products-solutions/force-sensors/a201?tab=description>.

[50] Carter, Bruce. Op Amps for Everyone. 4th ed. Waltham, MA: Newnes, 2013.

[51] Zhang, Haichong K., et al. "Synthetic tracked aperture ultrasound imaging: design, simulation, and experimental evaluation." Journal of Medical Imaging3.2 (2016): 027001-027001.

[52] J. A. Jensen, S. I. Nikolov, K. L. Gammelmark, and M. H. Pedersen, "Synthetic aperture ultrasound imaging," Ultrasonics, 44, e5-e15 (2006).

[53] L. F. Nock, and G. E. Trahey, "Synthetic receive aperture imaging with phase correction for motion and for tissue inhomogeneities. I. Basic principles," IEEE Trans. Ultrason., Ferroelect., Freq. Cont., 39, 489-495 (1992).

[54] G. E. Trahey, and L. F. Nock, "Synthetic receive aperture imaging with phase correction for motion and for tissue inhomogeneities. II. Effects of and correction for motion," IEEE Trans. Ultrason., Ferroelect., Freq. Cont., 39, 496-501 (1992).

[55] Zhang, Haichong K., et al. "In vivo visualization of robotically implemented Synthetic Tracked Aperture Ultrasound (STRATUS) imaging system using curvilinear array." SPIE Medical Imaging. International Society for Optics and Photonics, 2016.

[56] Balicki, Marcin Arkadiusz. "Augmentation Of Human Skill In Microsurgery." (2014).

[57] L. B. Rosenberg, "Virtual fixtures: Perceptual tools for telerobotic manipulation," in Virtual Reality Annual International Symposium, 1993, pp. 76–82.

[58] J. Abbott and A. Okamura, "Virtual fixture architectures for telemanipulation," in IEEE International Conference on Robotics and Automation. Ieee, 2003, pp. 2798–2805.

[59] J. J. Abbott and A. M. Okamura, "Pseudo-admittance Bilateral Telemanipulation with Guidance Virtual Fixtures," The International Journal of Robotics Research, vol. 26, no. 8, pp. 865–884, Aug. 2007.

[60] A. Bettini, P. Marayong, S. Lang, A. M. Okamura, and G. D. Hager, "Vision-Assisted Control for Manipulation Using Virtual Fixtures," IEEE Transactions on Robotics, vol. 20, no. 6, pp. 953–966, 2004.

[61] B. C. Becker, R. A. MacLachlan, L. A. Lobes, and C. N. Riviere, "Vision-based retinal membrane peeling with a handheld robot," in IEEE International Conference on Robotics and Automation. IEEE, May 2012, pp. 1075–1080.

VITA

Rodolfo Finocchi received his B.S. in Biomedical Engineering from the Johns Hopkins University, Baltimore, MD in 2015. He then entered the Masters in Robotics at Johns Hopkins University in the fall of 2016, focusing on Medical Robotics and Computer Integrated Surgical Systems. His research interests include medical robotics and devices, human-machine interfaces, computer-assisted surgery, and haptics.

Following the completion of his degree, Rodolfo will be working as a Research Engineer at Children's National Medical Center in Washington, DC. As part of an interdisciplinary team of experts in engineering and medicine, he will be helping to develop technologies that make pediatric surgery more precise, less invasive, and pain free.